Development of an Automatic Electromagnetic Resonance Rewarming System for the Cryopreservation of Large-Scale Biomaterials

Shen Ren

A dissertation

submitted in partial fulfillment of the

requirements for the degree of

Doctor of Philosophy

University of Washington

2020

Reading Committee:

Dayong Gao, Chair

Ming Chen

Zhiquan Shu

Junlan Wang

Program Authorized to Offer Degree:

Mechanical Engineering

University of Washington

Abstract

Development of an Automatic Electromagnetic Resonance Rewarming System for the Cryopreservation of Large-Scale Biomaterials

Shen Ren

Chair of the Supervisory Committee:
Professor Dayong Gao
Department of Mechanical Engineering

In the last few decades, applications of biopreservation, particularly cryopreservation, have played significant roles in scientific and clinical settings. The foundation of these approaches is the successful cryopreservation of biological samples, including deoxyribonucleic acid (DNA) / Ribonucleic acid (RNA), proteins, bio-fluids, cells, tissues, and organs. So far, we can only cryopreserve bio-samples of small volumes in the order of 1 mL, mostly due to the lack of an effective rewarming technique. For small volume systems, the convective rewarming method remains the gold standard. However, as the sample volume increased, the conventional way cannot avoid physical damage to the bio-specimen due to the cellular injuries induced by the remaining ice crystals. To prevent crystallization in the thawing process, rapid rewarming is the

key. Additionally, for larger biomaterials such as the bulk volume of cell suspension, tissues, or organs, a uniform temperature profile throughout the biomaterial is required to avert the larger thermal gradient that often causes fracture or cracks within the material. Thus, an ideal rewarming method should be both rapid and uniform to achieve the successful cryopreservation of large scale biomaterials. The conversion of electromagnetic energy into heat provides a possible solution to this problem. In this dissertation, an automatic electromagnetic resonance rewarming system is developed to (1) determine the critical thermal-electrical properties of the samples, (2) simulate and investigate the coupled electromagnetic and heat transfer problem, (3) adjust the frequency and power input in real-time to ensure the resonant state, (4) automatically load cryopreserved samples from liquid nitrogen to the rewarming chamber, and (5) achieve the rapid-uniform warming of large-scale biomaterials.

The cryoprotectant (CPA) is introduced to diminish the cryo-injuries during cryopreservation. The effectiveness of CPA, or vitrification solution, which is aiming to prevent ice crystals for larger samples in the lower temperature range completely, mainly depends on the composition and concentration of certain chemical agents. It is critical to understand and determine the electrical and thermal properties of CPA solutions to better utilize electromagnetic energy. The dielectric constant and dielectric loss were determined through a dynamic feedback system adopting the cavity perturbation theory. The thermal conductivities were determined with a designed micro thermal sensor, and specific heats were measured through differential scanning calorimetry (DSC). The selection of the optimal CPA/vitrification solution is based on the permeability of the cell membrane to the CPA, the toxicity of the CPA to the cells, absorptivity of the CPA to the electromagnetic power, and heat diffusion within the CPA solution. The higher concentration of CPA will reduce the ice formation in the sample during the cooling process, but

meanwhile, it also introduces higher osmotic pressure and toxicity that results in the damage or death of the cells. On the other side, the previously measured electrical and thermal properties of CPA solutions were analyzed to predict the rewarming rate and temperature profile. By balancing these fundamental parameters, the optimal CPA/vitrification solution for a specific type of biological materials was decided.

An exact analytic solution is hard to derive for the electromagnetic warming problem due to the complexity and nonlinearity of the electromagnetic and heat transfer theories. Therefore, a numerical simulation model built with COMSOL was used to predict the warming process, finalize the geometry of the sample holder, and optimize the power utilization efficiency.

Another challenge with electromagnetic heating is maintaining the resonant state during the entire rewarming process since an off-resonant state will dramatically reduce the sample's absorption of the electromagnetic energy. A real-time resonant frequency monitoring and controlling system was developed. As the temperature of the cryopreserved sample increased, the resonant frequency shifted and was captured by the control system. The system adjusted the signal source automatically based on the feedback from the tracking components to keep the power absorption at a high level. In the meantime, an aluminum-based supporting frame was designed, manufactured, and assembled to achieve the automated sample loading process. The results showed that this sample loading system could transfer the cryopreserved specimen from the liquid nitrogen environment to the heating chamber in a short time and protect the operator from the potential frostbite.

Several experimental tests of the automatic electromagnetic resonance rewarming system with cells and tissues were also performed in this dissertation. To further utilize the energy generated by the electromagnetic field, the magnetic nanoparticles (MNPs) were used to absorb

magnetic field energy and extend the improvements of rapid-uniform rewarming. In the cell test, Jurkat cells were chosen because of their importance in Leukemia and HIV research and poor preservation with current protocols for large volume. With the combined electromagnetic and MNPs warming, the recovery rate of 25 mL Jurkat cell suspension was obtained at 93.7±5.5%, almost doubled compared to the performance of the convective water bath method. The post-thaw assessment with alamarBlue assay proved the biological functionalities of Jurkat cell were well preserved with the electromagnetic resonance rewarming system. In the tissue test, rabbit jugular veins were chosen because of their similar vessel size to humans and the ease of handling. Vitrification solution was adopted to eliminate the ice crystals, post-thaw assessments including histology analysis, agonist and antagonist induced contractile and relaxation measurements, alamarBlue assay, and mitochondria membrane potential measurements were performed to qualitatively and quantitatively evaluate the performance of different rewarming methods.

Plans for future improvements are also presented in this dissertation, including the design of the next generation resonance cavity, further improvements of the resonant frequency monitoring and controlling system, and optimization of the organ rewarming test.

TABLE OF CONTENTS

LIST OF FIGURES

LIST OF TABLES

ACKNOWLEDGEMENTS

This dissertation is the output of the effort and support of several people to whom I am extremely grateful. I would like to express my sincere gratitude to everyone who supported me during this long journey.

First and foremost, I extend my gratefulness to my supervisor, life mentor, and guide, Professor Dayong Gao, for his incredible contribution in shaping the foundation of my research career. During the time at the University of Washington, his unflinching support, encouragement, scientific intuition, and wisdom inspired me and enriched my growth as a Ph.D. student. Apart from the academic work, his generosity, care, and love for me are unmatched. My involvement with him has triggered and nourished the intellectual maturity that I will benefit for the whole of my life.

I would like to thank Dr. Ming Chen for his numerous guidance on my experimental and theoretical study. As a mechanical engineering student, the electromagnetic theory is absurd and difficult to digest; Dr.Chen kept explaining the concepts and provided insightful ideas to the design and development of the control system.

I would like to thank Professor Zhiquan Shu for his continued support, guidance, and attention in the past six years that companioned me through this unpredicted Ph.D. expedition. Dr. Shu treated me like family; he cared about and helped me in every aspect of my personal development, including course study, teaching skills, and research.

I would like to thank Professor Jiaji Pan, who brought me into the electromagnetic area. He built a solid foundation and provided instructive comments and daily mentorship from the beginning of this work.

It is my highest honor to have Professor Junlang Wang and Professor Xiaohu Gao on my committee. Their insightful advice and suggestions on nanoparticles and ice crystals significantly improved the results and quality of this study.

I am also profoundly grateful for the support and hard work of my labmates and their substantial contribution to uplift the studies presented in this dissertation. Ji Peng and Praveen Sekar, for providing inspiring comments and continued support on the numerical simulation and heating experiments; Ye Jin and Ziyuan Wang, for the extensive contribution on automatic control and sample loading system; Shaohang Hao and Ruidong Ma, for the long-term help and support on cell and tissue tests; Dr. Cifeng Fang, Dr. Jinyuan Zhang, Nanye Du, Xiao Ma, Alexander Novokhodko, Leo Tao, and Yanyi Wang, for all their help, support, and valuable suggestions without which, this work would not have been possible.

Thanks to Professor Xiaoming Yang and Professor Buddy Ratner for kindly providing biomaterials; Dr. Jinhui Zhou and Dr. Xuefeng Kan for tissue harvesting; Hao Tang for measurements of mitochondrial membrane potential.

I appreciate the support from the ME department staff, especially Wanwisa Kisalang, for the great advising and relaxing work environment, and Nancy Moses, for all the rush ordering of the research supplies.

Fortunately, I also have the privilege of having a lovely family and friends who had a fundamental role in getting me through the Ph.D. process successfully.

My deepest and cordial gratitude, love, and appreciation go to my dear parents, Dr. Xiaohui Ren and Dr. Luo Chen, for their enduring love, trust, and encouragement. My love and thanks equally go to my parents-in-law, Luoyuan Zhou and Jun Hou, for their constant support made me strong during the hard days.

My dear wife, Yunjie Zhou, there is no way to thank her for being my side all the time. I have the luxury of being surrounded by her endless love and support that pushed me better and stronger every day. And our cat, Lizi, for all the companion days and nights.

Also, I feel lucky to meet so many smart and devoted friends, including but not limited to Dr. Yifan Chang, Dr. Yifan Cheng, Dr. Zheng Li, Dr. Guozheng Shao, Dr. Chaoyi Yang, Dr. Tianye Yang, Tristine Baccam, Wei Chen, Francis Estrada, Erik Hopf, Julie Mayer, Lucy Mayer, Michael Mayer, Zhongjie Qian, Yifei Ren, Yuzhou Shen, Kaisheng Song, Yunxiang Zhang, Yunshi Zhou, etc. Thanks for all the lovely and fun time spent together.

Chapter 1. INTRODUCTION

1.1 CRYOBIOLOGY AND CRYOPRESERVATION

Cryobiology studies the effects of low temperature and freezing on biomaterials and biological systems, including RNA, DNA, cells, tissues, and organs. In the past decades, cryobiology's rapid development leads to broad applications in agriculture, food science, reproductive medicine, and conservation of endangered life species. The beginning of systematic study and research of cryobiology trace back to 1949, when Polge et al. found rooster sperm with glycerol successfully survived in liquid nitrogen [2]. Since then, the investigation in cryobiology has continued to attract scientists and engineers with a variety of backgrounds in biomedicine, chemistry, material science engineering, electrical engineering, and mechanical engineering.

Cryopreservation is the technology to effectively suspend the 'time clock' of biological systems by cooling to low temperatures. The fundamental mechanism of preserving live materials is slowing down or even pausing enzymatic and chemical activities at such low temperatures. The biomaterials' structural integrity and biological functionalities are sustained via specifically designed cryopreservation protocols down to cryogenic temperature for long-term storage. Cryopreservation has been filled with needs in many fields, from fundamental research to clinical applications. Human sperm can be stored for years before the usage of fertilization. Stem cells (from bone marrow, cord blood, or peripheral blood) have been cryopreserved, transported, and then cultured and transplanted to cure various diseases since the 1950s. For instance, Hodgkin's and non-Hodgkin's lymphoma [3-5], myeloid or lymphoblastic leukemia [5-7], and solid tumors (testis, breast) [4, 5, 7-9]. Other successful cryopreserved biosamples including, red blood cells [10], oocytes [11, 12], liver cells [13], skin [14], cornea [8], etc. These practical experiences and

protocols led the foundation of establishing biobanks of biomaterials that bring the following advantages:

1. Biobanks provide opportunities to store both healthy and diseased cells and tissues for systematic studies and clinical treatments. Storage of large quantities of biosamples allows research and use of the samples at a time distant from their initial collection. Biorepository of diseased materials(e.g., cancers) is critical for physiology research, vaccine development, cellular therapy, and drug tests.
2. It extends the time window to screen transmissible diseases in the donated cells, tissues, and organs. Meanwhile, without large quantities and varieties of biosamples from different donors, it is impossible to find matching samples for the recipient.
3. It provides a solution to the schedule discord between donor and recipient. The patients in urgent conditions have the option to receive pre-matched biomaterials for transplant operations.
4. It creates a possibility for people to preserve the stem cells/tissues from themselves and use them in the future without concerns about transplant rejection.
5. It fits the needs of remote extracting the biological data of specific biosamples under the rapid development of the big data analysis.
6. It offers the potential to preserve the endangered animal and plant species.

However, upon so many benefits and achievements over the past years, there are still lots of challenges in the cryopreservation. Currently, many types of biomaterials cannot be well cryopreserved due to the so-called ‘cryo-injuries’ that happened during the freezing and thawing processes. Lovelock initially raised the concern that the increasing concentration of the solution

caused damage to the cell membrane and resulted in the death of the cell [15]. Meryman found the increasing extracellular osmolality led to the membrane injury, while the volume of intracellular water beyond the critical volume [16]. Later, it was realized by the scientists that the rate of the kinetic cooling and rewarming process were important to cryopreservation. In the 1970s, Mazur proposed a 'two-factor hypothesis' of cryoinjuries after the study of Chinese hamster tissue-culture cells [17].

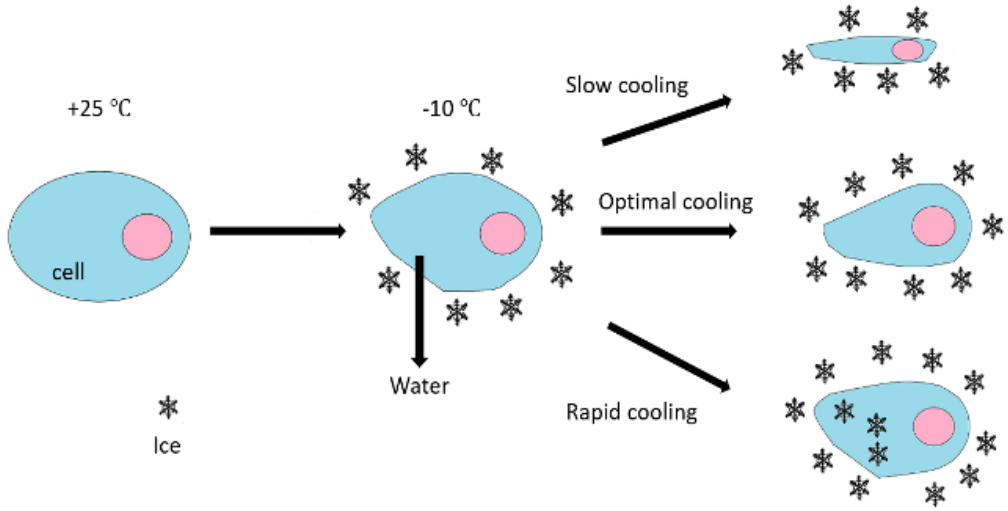

Figure 1-1. 'Two-Factor Hypothesis' of cryoinjury.

As shown in Figure 1-1, when a cell is cooled from room temperature to subzero temperatures (e.g., -10 ℃) under the atmosphere pressure, the extracellular osmolality was increased due to the formation of the extracellular ice. The inequality of the osmolality between intra- and extracellular environments leads to the efflux of water across cell membranes. Then, two distinctive cellular injuries may happen during the cooling process: 1) when the cooling rate is too high, there is not sufficient time for the water efflux before the intracellular ice formation (IIF). The lethal IIF can tear the cell membrane and is called 'ice injury'; 2) on the other side, when the cooling rate is too slow, water inside the cell has enough time to travel out until the

equilibrium of the osmolality and water chemical potential. As water is lost, the increased concentration of intracellular medium and electrolytes can be toxic to cells, which is called ‘solution injury’. Besides, the slow cooling may cause severe cell dehydration and volume shrinkage, exceeding the tolerance limit of the membrane. Thus, neither too fast nor too slow cooling process is favored for cryopreservation. An optimal cooling procedure should be slow

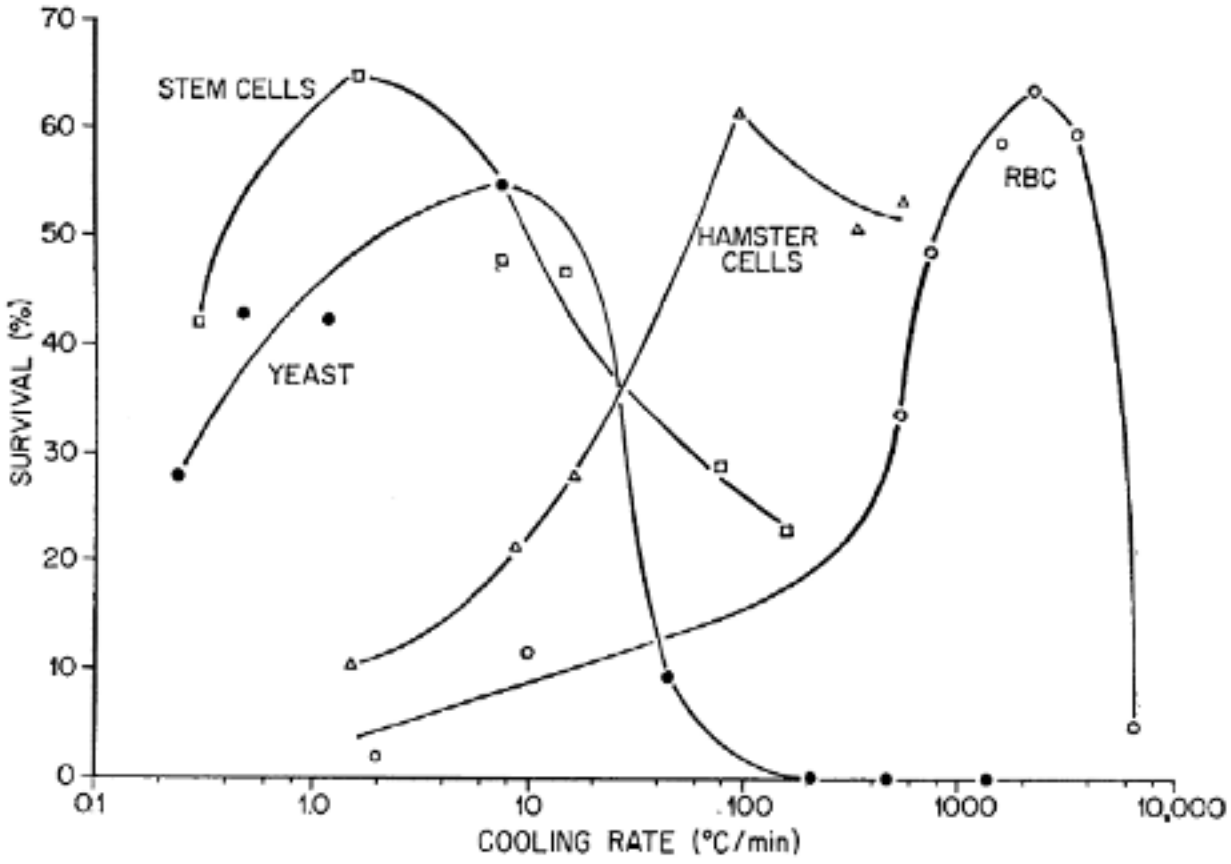

Figure 1-2. Comparative effects of cooling rate on the survival of various cells frozen and thawed rapidly

enough to avoid the ice injury but also rapid to prevent the solute injury. Based on the ‘two-factor hypothesis’, Mazur found an inverted ‘U’ shape between cell survival rate and the cooling rate [18], as shown in Figure 1-2. Each specific type of cell has an optimal cooling rate. Such an optimal rate is determined by the ability of water to cross the cell membrane, i.e., water permeability of the cell membrane [19].

1.2 CRYOPROTECTIVE AGENT(CPA)

To further alleviate the cryoinjuries, some chemical agents, named cryoprotectants or cryoprotective agents (CPA), were discovered. Since the unintended observation of glycerol's protective function in sperm cryopreservation in 1949, more than hundreds of CPAs have been used. In general, they can be classified into three categories.

1) Permeating CPAs, such as glycerol, dimethyl sulfoxide (DMSO), ethylene glycol (EG), and propylene glycol (PG). The mechanism of membrane-permeable CPAs is penetrating the cells, surpass the freezing temperature of the intracellular environment to inhibit IIF [20], and fill in the intracellular volume to compensate for the volume shrink due to water loss and prevent over-reduction of the membrane.
2) Non-permeating CPAs, such as sucrose, trehalose, dextran, Hydroxy-ethyl-starch (HES), and Polyvinyl Pyrrolidone (PVP). These CPAs cannot permeate into the membrane but do affect the extracellular matrix, drag water out of the cells, increase the extracellular viscosity, prevent intracellular freezing in the early stage of freezing, and increase the glass transition temperature (T_g).
3) Anti-freezing proteins (AFP). AFPs function with non-colligative property, which means the freezing temperature is not lowered proportionally to the AFP's concentration. Overdose of AFP may stimulate the ice formation. As the name implies, the appropriate addition of AFP can delay or prevent ice crystallization during the freezing by binding to small ice crystals to inhibit the growth and recrystallization of ice. Since the finding of AFP's existence in the blood of an arctic fish by Scholander in the 1950s [21], and isolation of AFP by DeVries in the 1960s

[22], AFPs have been studied and used in cryopreservation and food industry (e.g., additives in ice cream).

A typical successful cryopreservation process includes:

1) Adding appropriate CPA;
2) Freezing with the optimized cooling rate;
3) Storing the biomaterials at low temperatures;
4) Thawing the frozen samples;
5) Removing the CPA.

1.3 VITRIFICATION

Effective cryopreservation protocols are still unknown and needed for many types of cells. In addition, a larger sample size and complicated biological structure will escalate the difficulty of cryopreservation. Tissues and organs, unlike an individual type of cell, are often composed of various kinds of cells. The optimal cryopreservation protocol may sometimes be different for differentcell types. The combination and concentration of CPA, membrane properties, and optimal cooling rate could be significantly different between cells. The interaction between single and multiple types of cells in a complex biological system may also affect the outcome of cryopreservation. For example, in the freezing process of blood vessel preservation, excessive water fluxes from dehydrated cells into vessels may lead to vascular damage and structural destruction. The usually proper extracellular ice formation in cell preservation could be treated as devastating in tissue preservation.

Vitrification, an alternative approach to the traditional methods, is considered an effective way to cryopreserve complicated biomaterials. Also known as glassification, vitrification refers to the process that liquids are solidified into an amorphous state instead of in a solid crystalline pattern

[23]. Though the idea of vitrifying liquid solutions traces back one century ago, the rapid development of applications in cryopreservation started in the 1980s [24]. In Figure 1-3 [1], the

Figure 1-3. Frozen Kidney vs. Vitrified Kidney[1].

transparent vitrified rabbit kidney on the right-hand side clearly showed no ice crystals at -140 ℃, compared to the opaque frozen kidney on the left filled with ice. The kidney treated with conventional cryopreservation protocol can lead to the structure break caused by extensive ice formation and solution injury due to the substantial intracellular dehydration. However, the vitrified kidney proved that the side effects in the traditional procedure could be prevented if the glass state is reached and hold without apparent structure change during the cooling process. Without compromise between the two types of cryoinjuries, vitrification provides a new way to

discover the optimal cooling rate for tissues and organs. Therefore, vitrification is considered the most promising technology for the cryopreservation of complex multicellular biomaterials.

Compared to the cells, tissues and organs have a higher tolerance limit to the osmotic pressure and can survive under the higher CPA concentration. To achieve vitrification, the entire sample solution has to reach the glass transition temperature (T_g) at a rapid rate to avoid ice formation and accomplish the phase transition from liquid to non-crystalline amorphous solid. The minimal cooling rate to successfully achieve a vitrified state is defined as the Critical Cooling Rate (CCR). The CCR depends on the type and concentration of CPAs. In most cases, the higher concentration of the CPA cocktail, the lower CCR is required due to the viscous solution inhibiting molecular realignment into crystalline patterns. Hence, the CPA cocktail used in the vitrification protocol, or the vitrification solution, is often composed of higher CPA concentration to lower the CCR of the biological system to a realistic range. For pure water, the critical cooling rate is as high as $\sim 10^7$ ℃/min [25]. Such a high cooling rate is impossible to reach for a large size system like tissue or organ. With the addition of a vitrification solution, the CCR is diminished significantly. Several vitrification solutions and their glass transition temperature and critical cooling rate are listed in Table 1-1 [26].

Table 1-1. Cooling properties of vitrification solutions

Solutions	6 M glycerol	VS55	DP6	M22
Glass Transition Temperature (T_g)	−100 ℃	−123 ℃	−119 ℃	−120 ℃
Critical Cooling Rate (CCR)	−85 ℃/min	−2.5 ℃/min	−40 ℃/min	−0.1 ℃/min

Since the vitrification solved cooling challenges by preventing ice formation in intra- and extracellular fluids, cryoinjuries are no longer threats to monocytes, ova, early embryos, pancreatic islets, blood vessels, and articular cartilage [27-39].

1.4 CHALLENGES IN THE REWARMING PROCESS

Even though biosamples could survive through the cooling process to the low temperatures, they still have to face challenges caused by rewarming / thawing. Similar to the cooling rate in the freezing procedure, the rewarming rate plays an important role in the survival of biomaterials during thawing. If the warming rate is slow, small ice crystals developed during the cooling tend to merge and form large crystals. This ice crystal growth phenomenon is called 'recrystallization' and can damage the membrane and lead to cell death. In contrast, rapid rewarming is favorable since it can prevent recrystallization in the thawing.

The same warming challenge is also applied to the vitrified samples. After cooling below the glass transition temperature, the vitreous state could be maintained at low temperatures and stored for a long time. Once the materials are ready to be rewarmed from storage temperature to the physiological temperature (e.g., 4 ℃ or 37 ℃), the glassy state is quickly shattered due to the unstable phase at that temperature range. There are two major issues to consider for the vitrified materials during thawing. Firstly, a minimum rewarming rate is introduced as the Critical Rewarming Rate (CWR). CWR in the thawing is analogous with CCR in the freezing. The warming rate must be faster enough to reach the liquid state and surpass the kinetic ice crystal growth. A rate lower than the CWR could lead to 'devitrification,' corresponding to the recrystallization in the traditional cryopreservation. Secondly, the temperature profile needs to be uniformly distributed over the entire sample solution to avoid thermal stresses. The thermal stress

induced by a large temperature gradient would cause mechanical injuries and break the biomaterials' structure. Moreover, a recent finding stated that the mouse embryos with non-ideal cooling protocol could be recovered with an extremely rapid rewarming process [40]. Although it is too early to conclude that rapid warming can reverse freezing injuries, there is no doubt that the warming rate is vital in the thawing. As a result, a fast and uniform rewarming process is required for successful vitrification.

Conventional warming protocol typically consists of placing the biomaterials in a 37 ℃ water bath until the thawing is complete, leaves the larger samples exposed to the cyroinjuries. The water bath is a convective rewarming technology where heat is conducted from the exterior surface that directs contact with hot water to the core part of the samples. Due to the relatively low thermal conductivity and large heat capacity of biomaterials, it is hard to obtain a high warming rate through heat conduction. For a simple biological system, a single type of cell suspensions, the small thermal conductivity may be solved by the design of a sample holder (e.g., extended the surface area and reduced the thickness) [41]. However, for large tissues and organs with a much smaller surface area to volume ratio, they cannot be cut into slices or squeeze into a thin film to enlarge the heat transfer area. In this case, the temperature gradient will develop over time and cause large thermal stress to tear the biosamples. It may also overheat the outer layers before the inner portion has been thawed. Therefore, a slow heating rate and large temperature gradient restrained the traditional convective method as an appropriate approach for cryopreservation of large samples. To meet the rapid and uniform warming requirements, volumetric heating technology is needed.

1.5 ELECTROMAGNETIC REWARMING THEORY

Conventional warming protocol typically consists of placing the biomaterials in a 37 ℃ water bath until the thawing is complete, leaves the larger samples exposed to the cyroinjuries. The electromagnetic field generated by charged objects is coupled with the electric field and the magnetic field. A time-varying electric field (on the contrary of a static electric field) induces the magnetic field changing over time, and vice versa. The distribution and propagation of electromagnetic fields are governed by Maxwell's equations. Typically, electromagnetic radiation consists of an electromagnetic wave that is composed of oscillating magnetic and electric fields. In contrast to mechanical waves (water waves or sound waves) that required a medium to travel, the electromagnetic wave can travel through anything that is not electrically conductive – air, solid material, fluid, or vacuum. In a vacuum, the electromagnetic wave travels at $3 \times 10^8\ m/s$, the speed of light. In an isotropic media, the oscillations of the electric field and magnetic field are perpendicular to each other and perpendicular to the direction of energy and wave propagation, forming a transverse wave. This implies the waves are measured by their amplitude (height) and wavelength (distance between the highest or lowest points of two consecutive waves). Another fundamental property to characterize the electromagnetic wave is its 'frequency' that describes a wave's position in the electromagnetic spectrum. The most commonly used frequency band is at radio frequency (RF) wave and microwave. An illustration of electromagnetic waves over the spectrum is shown in Figure 1-4.

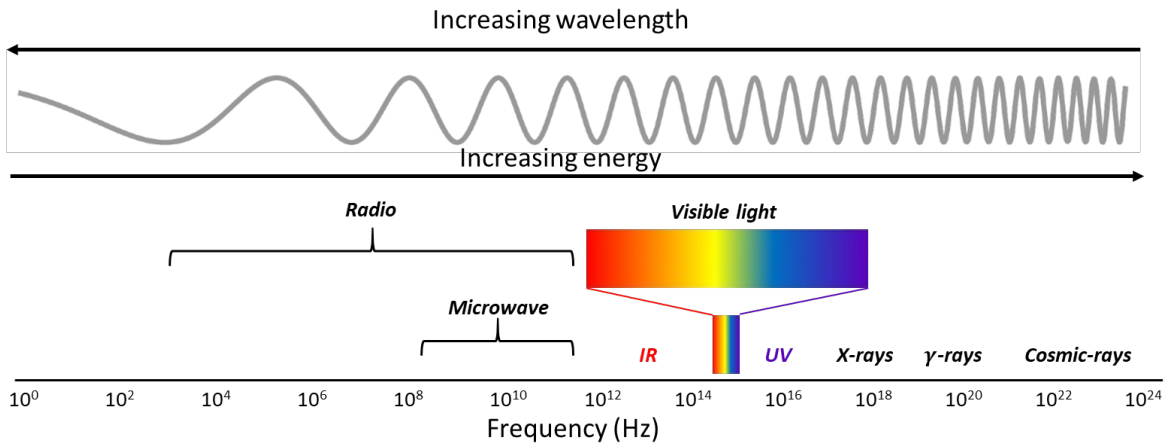

Figure 1-4. Electromagnetic waves over the spectrum

With the decreasing wavelength, the electromagnetic waves' energy increases and positively correlates to the frequency. Electromagnetic waves at a higher frequency, such as X-rays and γ-rays, carry strong power and are broadly applied in radiation therapy to kill the tumor cells by ionizing the molecules. Lower frequency electromagnetic waves (radio frequency, microwave) can hardly excite ionization with small energy density, but the power carried by these waves can still cause the thermal effects with materials.

Microwaves are electromagnetic waves with their wavelengths longer than infrared light but shorter than radiofrequency waves. Specifically, the microwave spectrum is defined as electromagnetic energy ranging approximately from 300 MHz to 300 GHz with corresponding wavelengths from 1m to 1mm. Though different sources have different frequency ranges definition over microwaves, the above broad definition contains both Ultra High Frequency (UHF) and Extremely High Frequency (EHF) bands. Generally, the frequencies over the microwave are divided into multiple bands that are labeled with letters P,L, S, X, K, Q, V, and W. The frequency limit and corresponding wavelength are listed in Table 1.2. The frequency at 2.45 GHz is widely used for commercial microwave ovens.

Table 1-2. Frequency limits and wavelength of microwave bands

Band	Frequency limits (GHz)	Wavelength (cm)
P	0.23 - 0.39	133.3 - 76.9
L	0.39 - 1.55	76.9 - 19.3
S	1.55 - 5.20	19.3 - 5.77
X	5.20 - 10.90	5.77 - 2.75
K	10.90 - 36.0	2.75 - 0.834
Q	36.0 - 46.0	0.834 - 0.652
V	46.0 - 56.0	0.652 - 0.536
W	56.0 - 100.0	0.536 - 0.300

The history of using the microwave as a heating technology trace back to the 1940s, a candy bar was melted by a device generating an active microwave. Based on this observation, scientists and engineers invented food heating and preparation equipment that adopted microwave radiation's thermal effects [42-45]. Later on, microwave applications have become widespread in the food industry and biomedical field. Most of the food ingredients contain a large amount of water that can interact with the electromagnetic field in the commercially available microwave oven due to the water's dielectric property. Water molecules have one positive charged end and one negative charged end. The dipole water molecules will align with the applied electric field. When the electric fields are switching as the oscillating electromagnetic waves, dipole molecules' position also rotates to tail the changing field. The interaction between

the rapidly changing electromagnetic field and water molecules caused mechanical friction on the water's surface and generated heat. Consider the uniform distribution of water molecules in the area, heat is produced volumetrically. Similar to food, biomaterials are mainly composed of water. Thus, the microwave is a promising technology to be used for the volumetric heating in the cryopreservation.

In most of the cases, the cryopreserved samples are nonmagnetic biomaterials. When using the microwave as the heating method, the movements of dipole molecules are mainly induced by the electric section of the electromagnetic field. Compared to the conductive water bath method, a clear advantage of microwave warming is that heat is generated over the entire region of the sample, which diminished the effect of low thermal conductivity. The electrical component characterized the relationship between the sample and electric field is defined as relative complex permittivity,

$$\varepsilon_r = \varepsilon' - i\varepsilon'' \tag{1.1}$$

The complex permittivity is also known as the dielectric property. The real part of complex permittivity ε', also called dielectric constant, represents the capability of storing energy when exposed to an electric field. The imaginary part of the complex permittivity ε'', known as dielectric loss, represents the ability to absorb energy from the electric field. Where $i = \sqrt{-1}$, or,

$$\varepsilon = \varepsilon_0(\varepsilon_r' - i\varepsilon_{eff}'') \tag{1.2}$$

where ε_0 is the permittivity of free space, ε_r' is the relative dielectric constant, and ε_{eff}'' is the effective relative dielectric loss factor.

When a dielectric material is subject to an electromagnetic field, the local volumetric heating rate or the density of microwave power deposition Φ is given:

$$\Phi = \omega \varepsilon_0 \varepsilon''_{eff} |E|^2 \tag{1.3}$$

where ω is the angular frequency of the electromagnetic field, and $|E|$ is the root-mean-square magnitude of the electric field in the dielectric sample, which varies significantly with its position in the field.

The heat transfer equation within the cryopreserved sample under the electromagnetic heating is given by:

$$\rho C \frac{dT}{dt} = \Phi k \nabla^2 T \tag{1.4}$$

where ρ is the material's density, C is the specific heat capacity, k is thermal conductivity, and T is temperature. For fast heating, the second term of the equation is negligible since $\Phi \gg k\nabla^2 T$, then the warming rate can be calculated by:

$$B = \frac{dT}{dt} \approx \frac{\Phi}{\rho C} \tag{1.5}$$

Compared to the conventional heating approach, heat transfer analysis in microwave warming is more complicated due to the complex relationship between the dielectric sample and the electromagnetic field. From equation (1.3), microwave energy absorbed by the cryopreserved sample is controlled by the electric field. As the sample absorbs more energy, the temperature increased. As a result, the dielectric properties of the sample change accordingly, which in turn affect the electric field, and eventually influence the heating performance of the biomaterial.

1.6 PREVIOUS REWARMING ATTEMPTS BY CYROBIOLOGIST

The study of microwave thawing began in the 1960s. Allen et al. found the tissue's different electrical conductivity under different temperatures may significantly affect the thawing result with microwave [46]. In the 1970s, Ketterer reported successful rewarming of a canine kidney [47]. The warming process was monitored with power control to prevent overheating by the end. In total, they claimed approximately 20 kidneys were considered as partial successes. Successful electromagnetic rewarming of dog kidneys was also reported by Guttman using a 1.35 KW Toshiba commercial microwave oven at 2.45 GHz. Sixteen kidneys were frozen to -80 ℃, rewarmed by microwave, and then transplanted. Half of the implanted dogs survived 2-14 months [48]. Pegg attempted to repeat Guttman's work; however, out of 14 dog kidneys that were froze and then thawed by a commercial 2.45 GHz microwave over, none of them maintained biological functionalities after the transplantation [49]. Another trial was performed by Burdette with an electromagnetic illumination system [50]. The system was capable of monitoring transmitted and reflected power and can work at both single frequency (2.45 GHz) and multi-frequency status. Rewarming results of rabbit and dog kidney were presented without functionality analysis by transplantation.

Besides the microwave approach, other techniques about rapid rewarming were also attempted by cryobiologists. In 2014, Jin achieved ultra-rapid rewarming of mouse oocytes by an IR laser pulse [40]. Later, Bischof reported the improved tissue cryopreservation method using radiofrequency coil and magnetic nanoparticles as the heating technology [26]. Porcine arteries and aortic heart valve leaflet tissues were successfully vitrified and thawed. These preceding explorations allowed scientists to implement cutting-edge technologies from electrical engineering, material science, and chemical engineering into the application of cryopreservation.

A major problem with electromagnetic rewarming at the 2.45 GHz frequency is that the limited penetration depth. The electromagnetic wave cannot reach to the core part of biomaterials and caused nonuniform heating within the sample solution. Lower frequencies are favorable for large-scale biomaterials with large penetration depth.

In addition, nonuniform heating in microwave warming will lead to a problem introduced as 'thermal runaway.' The temperature difference in the sample during heating contributes to the spatial nonuniform microwave energy absorption. Liquid water has a much higher absorbtivity of electromagnetic power than ice. In the thawing process, once partial materials are melt, the temperature of that part increases tremendously because more energy was absorbed and created a hot spot. Moreover, the warmer area will continue to absorb more energy since melted water is dominated in the sample volume. As a result, the warm area is getting warmer and warmer while the cold area remains cold. Eventually, the increased temperature gradient may cause a fracture of the sample. Therefore, an electromagnetic system with a lower frequency and dedicated control is needed for cryopreservation.

In the 1990s, Fahy developed a system using a helical coil to create an electromagnetic field at a frequency of tens of MHz [51]. Rewarming of the aqueous solution was attempted, and the rate was insufficient to heat up vitrified samples. Then, a few scientists redesigned the electromagnetic heating in a closed system with confined electromagnetic energies [52, 53]. Different from the household microwave oven that shifted signal around ± 50 MHz, the redesigned system synthesized an electromagnetic wave by a voltage controlled oscillator. This change improved the stability of the frequency and established a resonate state within the chamber to concentrate the electromagnetic energy. In Rachman's design[52], two resonant

states of the chamber were excited (TE111 and TM010). In Robinson's system, three different modes were excited[53].

The multimode cavity is intentionally designed to prevent or break any standing wave pattern within the cavity. The electromagnetic fields in the multimode cavity could be treated as the superposition of multiple plane waves impinging on the cryopreserved sample from various directions. Thus, it is possible to reduce the temperature nonuniformity with a multimode cavity. But it is extremely complicated to calculate and analyze the multimode pattern and makes it nearly impossible to apply any dynamic feedback control system. In this dissertation work, a single mode cavity is built to create a standing wave pattern inside the cavity. The intensity of the electric field is most vigorous at the peaks of the standing wave and lowest (theoretically at zero) at the nodes of the standing wave. With a careful design of the geometry and dimension of the cavity, a control system can be developed to correspond the characteristic wavelength of the microwave source.

1.7 DISSERTATION OUTLINE

The structure of this dissertation is organized as follows.

Chapter 2 shows that the sample solution is frozen through a controlled rate freezer and rewarmed with different heating methods. Post-thaw cell recovery rate and biological functionalities are measured. The results can be used to determine the warming rate effects on the various cooling rates.

In chapter 3, a physical property measurement system is set up to determine the critical electric and thermal properties of CPA solutions. The impact of these properties on the microwave rewarming and effect on the optimal CPA selection is discussed. Numerical modeling of the resonant cavity is conducted to assist the development of the electromagnetic

rewarming system, including the dimension of the chamber, the shape of the sample holder, and simulated rewarming results.

In chapter 4, the development of the real-time resonant frequency monitoring and controlling system is presented to ensure the optimal resonant frequency during the rewarming process. Multiple approaches to achieve dynamic feedback control of frequency are attempted, the rewarming performance is compared among different methods. Additionally, an automatic sample loading system is designed and built.

In chapter 5, 25 mL Jurkat cell suspension is thawed with the electromagnetic resonance rewarming system. Chapter 6 presents the experimental result of the cryopreserved blood vessel.

In the last chapter, the limitations of the current system and the corresponding potential improvements are described. To further enhance the heating performance, the preliminary design of the future system is proposed.

Chapter 2. DETERMINATION OF THE REWARMING RATE EFFECTS ON CRYOPRESERVED SAMPLES COOLED WITH VARIOUS COOLING RATES

2.1 INTRODUCTION

The optimal cooling rate is critical to the successful cryopreservation, so is the rapid rewarming rate. A slow warming rate may cause recrystallization or devitrification in the sample solutions that eventually lead to the rupture of the cells. Small ice crystals within the frozen cells are considered thermodynamically unstable comparing to the larger ice crystals. The small ice crystals' instability leads to a lower melting temperature [54, 55]. As a result, the small crystals tend to group to form large crystals during the thawing process. Thus, slow warming is lethal to the cells since it creates a time window for such recrystallization to arise. The relationship between intracellular ice induced by recrystallization and the cell death had been visually observed under the microscope for yeast cells, higher plant cells [56], ascites tumor cells [57], and Chinese hamster tissue cells [58]. On the other side, rapid warming has been proved beneficial to the cell survival rate, especially for the rapidly cooled biosamples. MacKenzie reported successful survival of the yeast cells that freezing under a cooling rate far beyond the optimal rate. But the yeast cells with the same cooling protocol did not survive with slow rewarming [59]. In his experiments, yeast cells were slowly rewarmed from -196 ℃ to various temperatures, then switched to the fast warming to complete the remaining thawing process. Figure 2-1 shows the correlation between the yeast cells' survival rate and the start temperature of the rapid rewarming. A significant drop in the survival rate was observed once the rapid rewarming beginning temperature reached above -40 ℃. In another test with rapid cooling yeast cells, Bank captured the recrystallization

phenomenon that started to occur at -35 ℃ during the slow rewarming process [60] and explained the cell death in the previous test. The larger ice crystals were observed when the termination temperature of the slow rewarming was at -20 ℃, but no recrystallization was seen at -50 ℃, as shown in Figure 1-3. Similar results were reported by Moor [61].

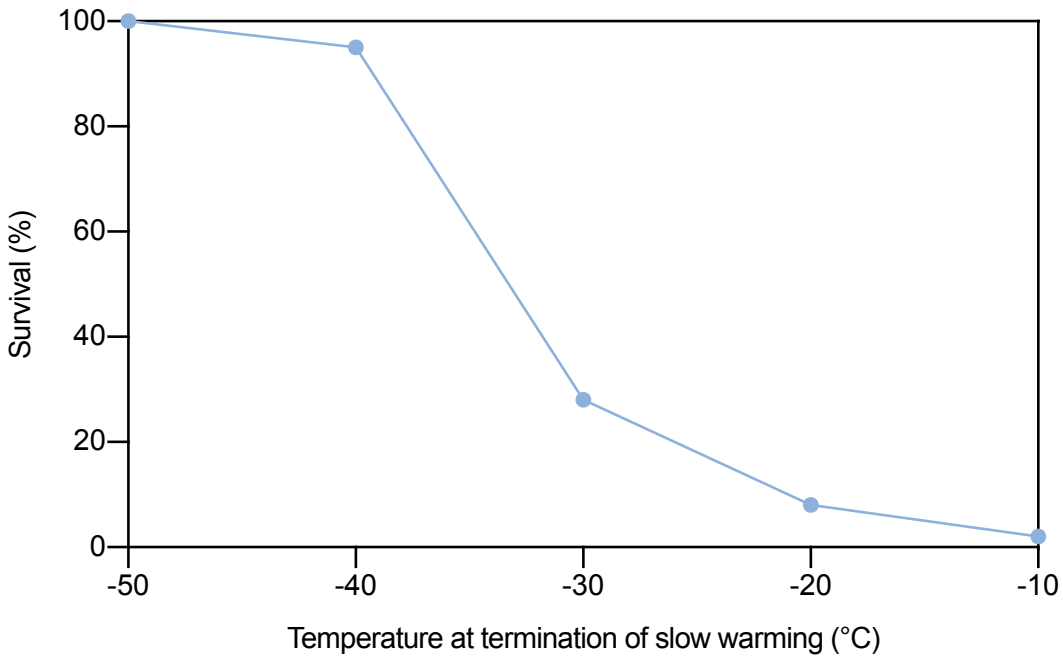

Figure 2-1. Correlation between the survival rate of the rapidly cooled yeast cells and the termination temperature of the slow rewarming (Reproduction from Mazur [62])

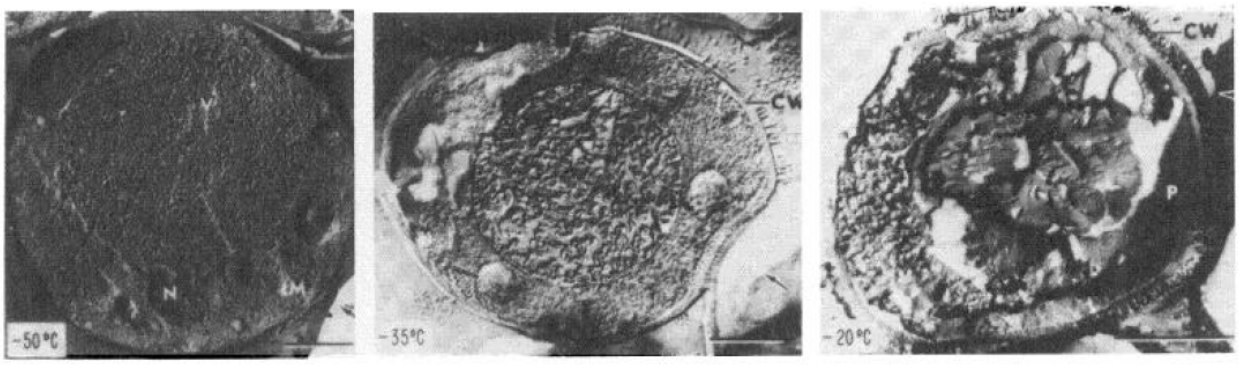

Figure 2-2. Recrystallization of intracellular ice in rapidly frozen yeast cells during slow rewarming process (Reproduction from Mazur [62])

Table 2-1. The survival rate of rapidly frozen cells by slow warming and fast warming (Reproduction from Mazur [62])

Cell Type	Cooling Rate (℃/MIN)	Survival After Warming (%)	
		Slowly	Rapidly
V79	600	5	65
CHO	100	30	75
Mouse and human stem cell	200	0 - 4	25 – 30
Human red blood cells	600	8	63
Mouse and rabbit cell embryos	2 steps	0	80
Mulberry cells	100	5	60
Cultured carrot	2 steps	5	45
Lily pollen	200	0	100
Yeast	450	10^{-6}	8
Neurospora spores	250	8	95

Table 2-1 shows the survival rates of various cells frozen with a fast cooling rate and thawed with slow or rapid rewarming rates. The results indicated biological samples with intracellular ice are more sensitive to the slower warming process due to the recrystallization. However, rapid rewarming that preclude recrystallization did not show the sensitivity and improved the cells' survival rate. In the Society for Cryobiology's 51st annual meeting, Mazur,

who proposed the 'Two-factor Hypothesis' during the cooling process, discussed the possibility that the rapid warming rate is even more crucial to the survival of biomaterials than the concentration of cryoprotective agents and fast cooling rate. Though the previous researchers showed that rapid thawing could improve the viability of the cells, but those cells were rapidly cooled to the storage temperature. In this chapter, the effect of the rewarming rate on the biological system is determined with various cooling rates. The recovery rate of the cells is measured to analyze the performance of the warming process. Cell metabolism is captured to evaluate the post-thaw biological functionalities.

2.2 MATERIALS AND METHODS

2.2.1 *Cell culture and sample preparation*

Jurkat cell, a cell line of human T lymphocyte cells, was chosen as the biological sample due to its importance in acute T cell leukemia, T cell signaling, HIV research, and other clinical studies. The original Jurkat cell lines were purchased from ATCC (American Type Culture Collection, Manassas, VA), then reproduced to passage 3, and cryopreserved at -196 ℃. All of the cells used in this test were thawed with a water bath and cultured with the following procedures.

As an immortalized cell line, Jurkat cells were cultured in an incubator (VWR International, Radnor, PA) that setting at 37 ℃, 5% carbon dioxide, and proper humidity. T25 (Corning Inc., Corning, NY) flasks were used during the culture process. A unit of the cell growth medium was prepared of 450 mL RPMI medium (Life Technologies, Carlsbad, CA), 50 mL fetal bovine serum (Life Technologies), 5 mL Penicillin-Streptomycin (Life Technologies), and 5 mL L-glutamine (Life Technologies).

Cells were cultured to the live cell concentration at $1 \times 10^6\ mL^{-1}$, then aliquoted to individual cryovials and ready for the addition of the CPA.

2.2.2 *Cryoprotective agents*

In clinical applications, cell growth medium with 5% ~ 10% (v/v) DMSO is widely used as the CPA for the cryopreservation of Jukart cells. In this test, an additional 0.25 M Trehalose has been added to the CPA cocktail.

Trehalose is a naturally-derived sugar consisting of two molecules of glucose. It has been found that some bacteria, fungi, plants, and invertebrate animals can synthesize trehalose as a source of energy and to survive the freezing climate and the lack of water (drying state) naturally during the cold winter or in the super dried weather. The mechanism of trehalose's cryoprotective function is different from the other sugars, such as sucrose, glucose, etc. When added to the water-based solutions, trehalose affects both the structure and dynamics of water molecules relative to each other. It takes apart the tetrahedral hydrogen bond network of water, preventing water from crystallizing into ice. It also slows down water molecule dynamics to protect cells from the cryoinjuries. The six major cryoprotective functions of the trehalose are as follows:

1) Reducing and preventing the formation of ice crystals,
2) Regulating the size and shape of ice crystals,
3) Protecting proteins' structure and function,
4) Stabilizing cell membrane structure and integrity,
5) Inhibiting apoptosis,
6) Regulating the osmotic pressure of the cells.

The final concentration of the CPA cocktail used in this test was 10% (v/v) DMSO plus 0.25 M trehalose. The stock solution (20%(v/v)DMSO + 0.5 M trehalose) was added to the cell suspension slowly with a dropwise method until the final concentration of CPA was reached. The CPA addition process was performed on ice to compensate for the heat released from DMSO.

2.2.3 *Cooling device and protocols*

A programmable controlled rate freezer (CryoMed 7456, ThermoFisher Scientific) was implemented to mimic different controlled cooling processes. From slow to fast, the cooling rates were 0.1, 0.5, 1, 5, 10, and 20 ℃ min^{-1}, respectively. In addition to the controlled cooling rates, the fastest cooling was achieved by injecting the sample into the liquid nitrogen directly.

An example of the cooling protocol for the controlled rate freezer is given as follow:

1) Wait at 4 ℃,
2) Cooling the sample temperature to -4 ℃, at 1 ℃ min^{-1},
3) Cooling the chamber temperature to -40 ℃, at 25 ℃ min^{-1},
4) Heating the chamber temperature to -12 ℃, at 10 ℃ min^{-1},
5) Cooling the sample temperature to -85 ℃, at 0.1 ℃ min^{-1},
6) The cooling ends at -85 ℃.

2 mL of sample solution (1 mL cell suspension + 1 mL CPA) was used as the sample volume with cooling rates at 0.1, 0.5, and 1 ℃ min^{-1}. Considering the cooling capacity of the controlled rate freezer may not fulfill the cooling needs, a smaller volume of 500 µL (250 µL cell suspension + 250 µL CPA) was selected to achieve the faster cooling rate at 5, 10, and 20 ℃ min^{-1}. The same 500 µL sample volume was also applied to the liquid nitrogen injected cooling process.

A thermal couple (Omega Engineering, Norwalk, CT) was inserted at the center of the sample solution, and a data acquisition system (TracerDAQ, Measurement Computing Corporation, Norton, MA) was connected to monitor and record the sample temperature during the entire cooling process.

2.2.4 *Rewarming methods*

Three rewarming methods were applied to succeed at different warming rates. The rapid rewarming was achieved by the electromagnetic warming system. The details of the development of the EM system will be introduced in the following chapters. An optic fiber temperature sensor (TS4-02, Micronor) was placed at the center of the sample to acquire the inner temperature. The heating was conducted till the central temperature reached 0 ℃.

The conventional water bath method was implemented as intermediate warming rates. The cryopreserved sample solutions were fully immersed into the pre-warmed, 37 ℃ water bath. The water bath was shaking at 60 RPM in an orbital motion to reduce the temperature gradient within the sample solution. The rewarming process was terminated until the thermal couple reading reached 0 ℃.

Air natural convection at room temperature was used as the slow warming approach. The cryopreserved samples were put on the countertop without other temperature sources or motion disturbances. The thawing was ended once the thermal couple reading reached 0 ℃, and no noticeable ice crystals were observed within the sample solution.

2.2.5 *Determination of the biological characteristics of the cells*

Cell membrane integrity was determined by Trypan blue (Life Technologies) staining assay to calculate the recovery rate of the Jurkat cells. Since cells have a high selectivity to the compounds that traverse the membrane, the live cell with an intact membrane won't be colored. The dye can penetrate into the dead cells due to the larger permeability to the Trypan blue, and then the stained cells can be observed under the microscope. A cell counter (Countess II, Invitrogen) was used to count live cells, dead cells, and cell density. The recovery rate of the Jurkat cells was determined according to the following equation:

$$\text{Recovery rate} = \frac{\text{\# of live cells before cryopreservation}}{\text{\# of live cells after cryopreservation}} \times 100\% \qquad (2.1)$$

Post-thawed cell metabolic activity was assessed by alamarBlue assay (Invitrogen, Carlsbad, CA). AlamarBlue is a highly sensitive cell proliferation assay in which the resazurin is converted to resorufin during the cellular metabolic reaction [63]. The reagent is a redox indicator since it is not interfering in any way with the reaction of the electron transport chain and detects the level of oxidation during respiration. After the warming procedure, 90 µL of cell suspension were mixed with 10 µL alamarBlue assay solution in a 96 well plate and then incubated at 37 ℃. The absorbance was measured by a microplate reader (Multiskan FC, Thermo Fisher Scientific) in duplicate for each well at 4h, 24 hr, 48 hr, and 72 hr. The positive control group consisted of fresh Jurkat cells that did not go through the cryopreservation procedures. The average value of two readings of the blank samples (90 µL growth medium with 10 µL alamarBlue assay solution) was subtracted from the average value of the sample plates to yield relative absorbance units. The SkanIt 6.0 (Thermo Fisher Scientific) software was used to measure the plates with absorbance

parameters set to wavelengths at 570 nm and 600 nm. The absorbance readings were normalized to the positive control groups and presented as a percentage.

2.3 RESULTS

2.3.1 *Cooling temperature profile and cooling rates*

The recorded temperature profiles of Jurkat cells under different cooling rates are shown in Figure 2-3.

Figure 2-3A shows the temperature profiles of samples directly injected into the liquid nitrogen. The average cooling rate was calculated as 340.3 ± 14.2 ℃ min^{-1}. Figure 2-3B shows the temperature profiles of cooling rates at 5, 10, and 20 ℃ min^{-1} respectively. The average cooling rate was calculated as 4.8 ± 0.7, 9.6 ± 1.1, and 21.4 ± 1.8 ℃ min^{-1}. Figure 2-3C shows the temperature profiles of cooling rates at 0.1, 0.5, and 1 ℃ min^{-1} respectively. The average cooling rate was calculated as 0.10 ± 0.03, 0.48 ± 0.04, and 1.07 ± 0.12 ℃ min^{-1}

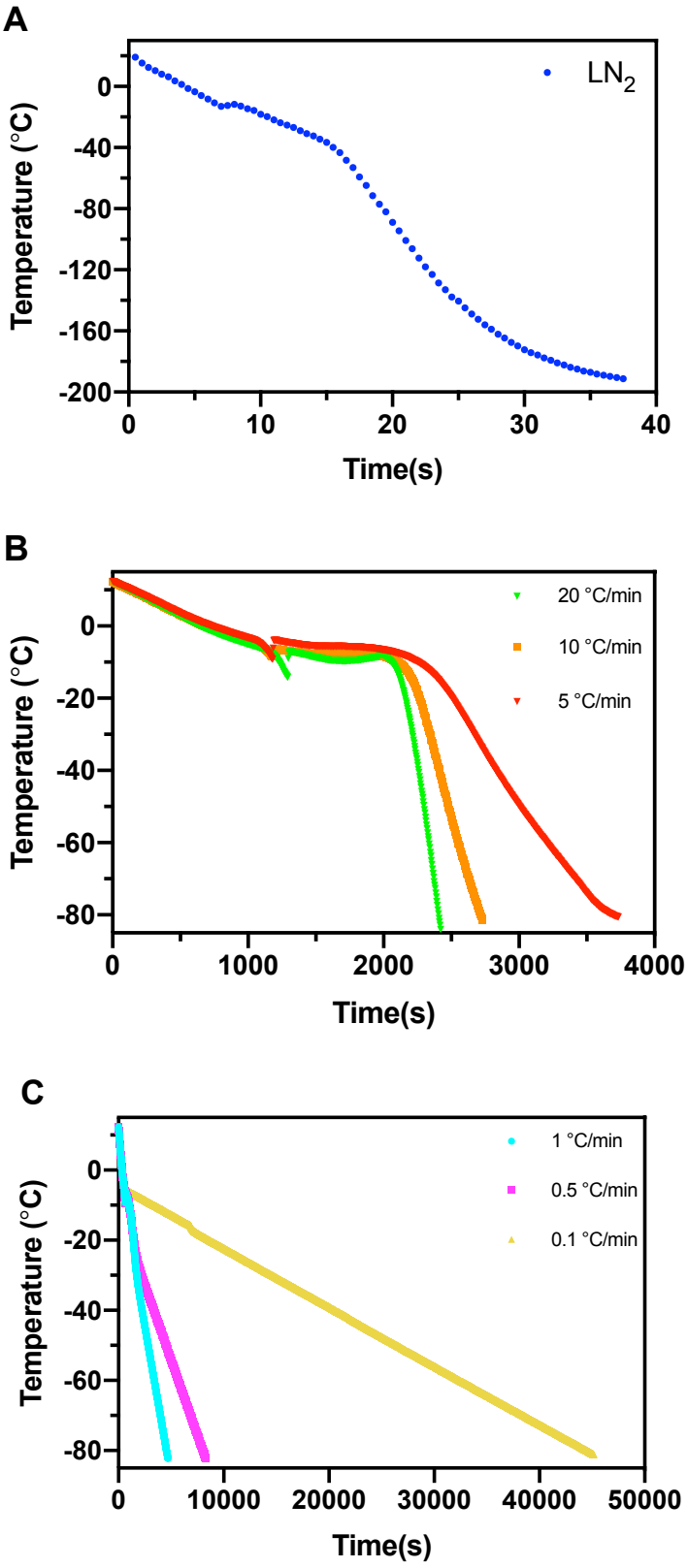

Figure 2-3. Temperature profiles of the different cooling rates

2.3.2 *Rewarming temperature profile and rewarming rates*

The temperature profiles of the Jurkat cells with different warming methods from -85 ℃ to 0 ℃ are shown in Figure 2-4. Figure 2-4 A shows the temperature profiles of air warming. The average warming rates of 500 μL and 2 mL samples are 8.95 ± 1.41 ℃ min^{-1} and 8.03 ± 0.86 ℃ min^{-1}. Figure 2-4 B shows the temperature profiles of water bath warming. The average warming rates of 500 μL and 2 mL samples are 78.42 ± 4.01 ℃ min^{-1} and 67.11 ± 3.47 ℃ min^{-1}. Figure 2-4 C shows the temperature profiles of electromagnetic warming. The average warming rates of 500 μL and 2 mL samples are 1482 ± 57.46 ℃ min^{-1} and 1195 ± 63.27℃ min^{-1}.

The temperature profiles of the Jurkat cells with different warming methods from -190 ℃ to 0 ℃ are shown in Figure 2-5. Figure 2-5 A shows the temperature profiles of air warming. The average warming is 10.16 ± 2.13 ℃ min^{-1}. Figure 2-5 B shows the temperature profiles of water bath warming. The average warming rate is 76.08 ± 2.25 ℃ min^{-1}. Figure 2-5 C shows the temperature profiles of electromagnetic warming. The average warming rate is 588.10 ± 18.15℃ min^{-1}.

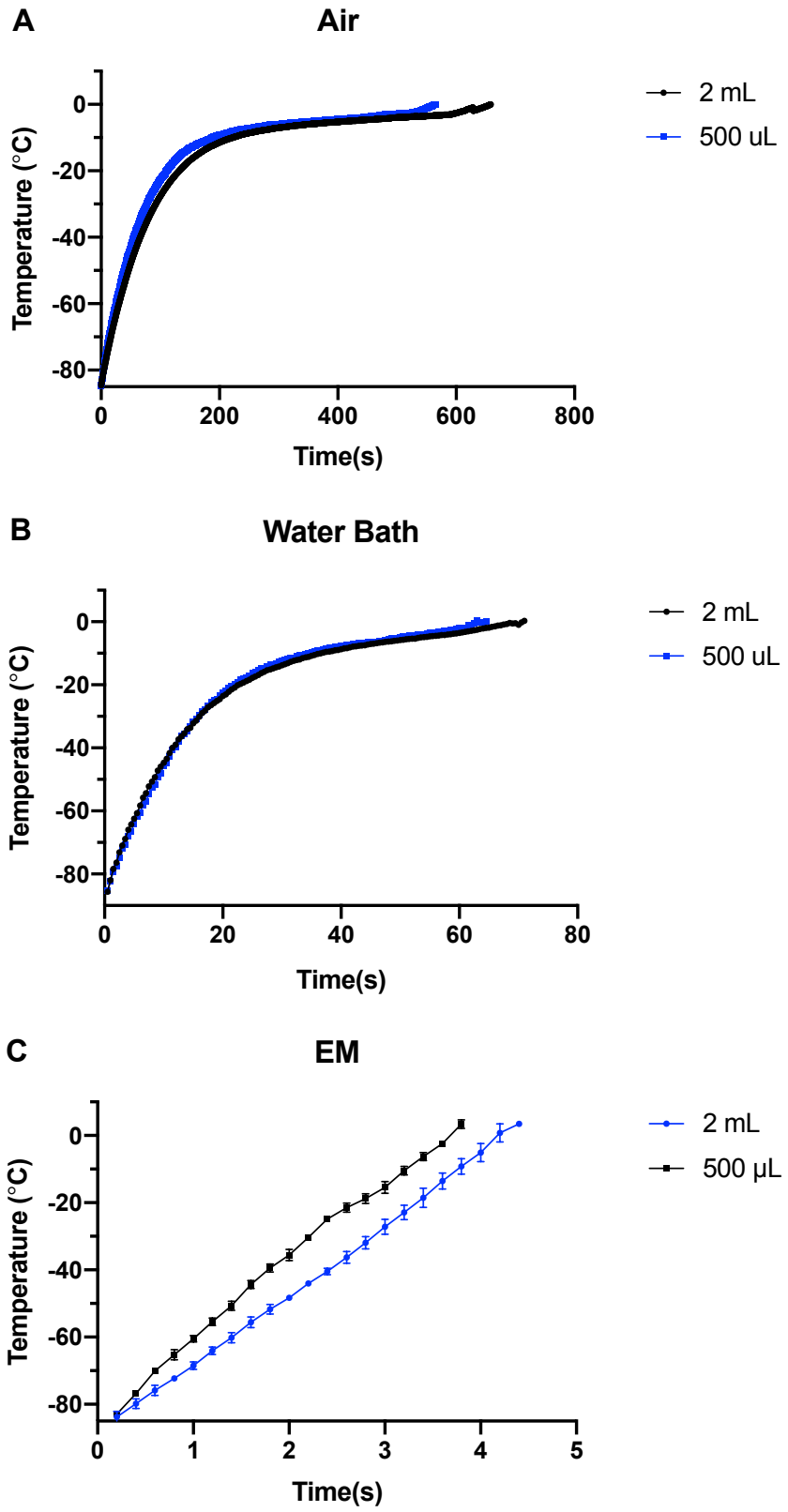

Figure 2-4. Temperature profiles of the different warming methods from −85 ℃ to 0 ℃

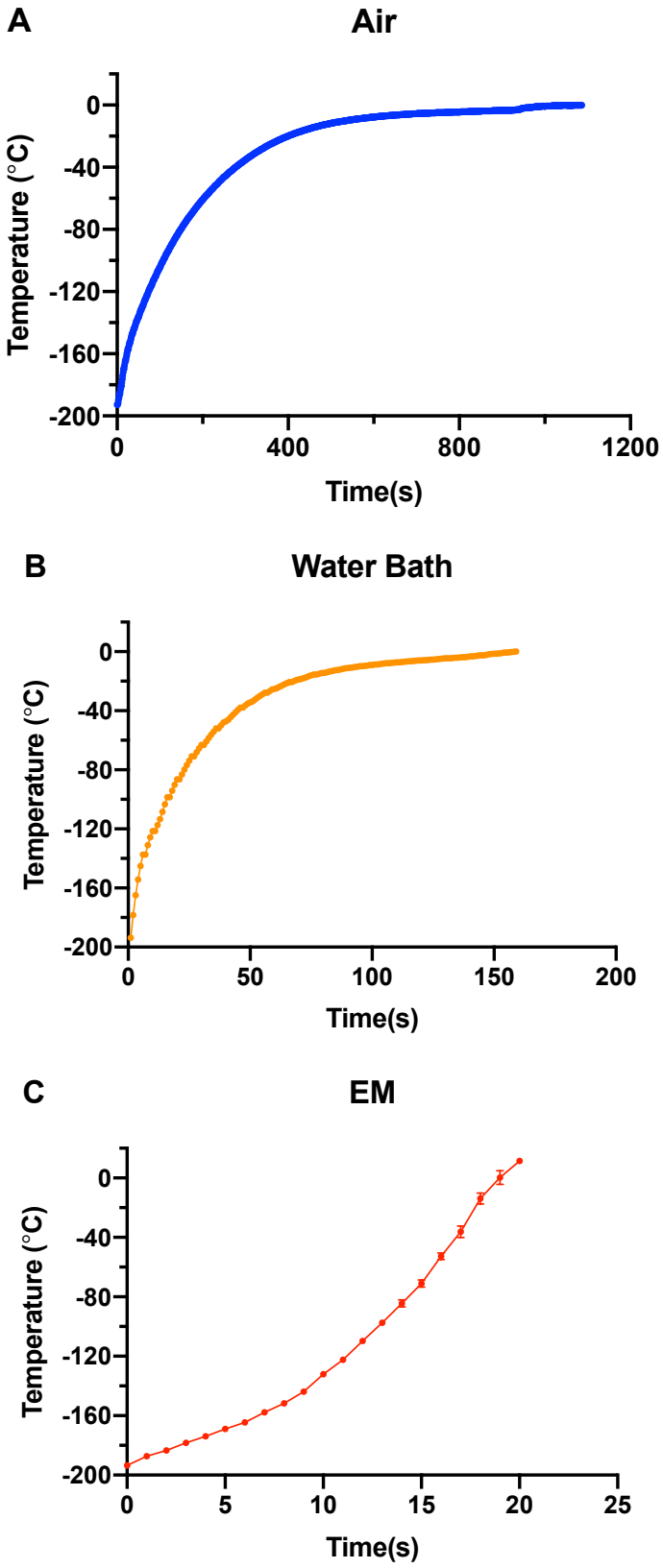

Figure 2-5. Temperature profiles of the different warming methods from −190 ℃ to 0 ℃

2.3.3 *Determination of the recovery rate of the cells*

The recovery rates of the Jurkat cells of different cooling and rewarming processes are shown in Figure 2-6.

Figure 2-6 A shows the recovery rates of the Jurkat cells at the 0.1 ℃ min^{-1} cooling rate. Air warming achieved the recovery rate at $2.98 \pm 1.12\%$, while water bath and electromagnetic warmings are $6.03 \pm 4.16\%$ and $6.05 \pm 2.42\%$. The recovery rate of EM rewarming is significantly higher than air warming ($P = 0.0057$).

Figure 2-6 B shows the recovery rates of the Jurkat cells at the 0.5 ℃ min^{-1} cooling rate. Air warming achieved the recovery rate at $10.07 \pm 6.76\%$, while water bath and electromagnetic warmings are $12.39 \pm 7.47\%$ and $13.27 \pm 4.42\%$. There is no statistical significance for the rewarming rates due to the high variability.

Figure 2-6 C shows the recovery rates of the Jurkat cells at the 1 ℃ min^{-1} cooling rate. Air warming achieved the recovery rate at $67.40 \pm 7.82\%$, while water bath and electromagnetic warmings are $83.18 \pm 4.51\%$ and $89.23 \pm 2.69\%$. The recovery rate of EM rewarming is significantly higher than the water bath ($P < 0.001$) and air warming ($P < 0.0001$).

Figure 2-6 D shows the recovery rates of the Jurkat cells at the 5 ℃ min^{-1} cooling rate. Air warming achieved the recovery rate at $55.11 \pm 6.90\%$, while water bath and electromagnetic warmings are $80.79 \pm 10.05\%$ and $88.78 \pm 5.71\%$. The recovery rate of EM rewarming is significantly higher than the water bath ($P = 0.0081$) and air warming ($P < 0.0001$).

Figure 2-6 E shows the recovery rates of the Jurkat cells at the 10 ℃ min^{-1} cooling rate. Air warming achieved the recovery rate at $41.14 \pm 9.37\%$, while water bath and electromagnetic

warmings are $53.33 \pm 10.90\%$ and $85.48 \pm 6.26\%$. The recovery rate of EM rewarming is significantly higher than the water bath ($P < 0.0001$) and air warming ($P < 0.0001$).

Figure 2-6 F shows the recovery rates of the Jurkat cells at the 20 ℃ min^{-1} cooling rate. Air warming achieved the recovery rate at $5.03 \pm 1.85\%$, while water bath and electromagnetic warmings are $20.93 \pm 3.29\%$ and $35.92 \pm 7.64\%$. The recovery rate of EM rewarming is significantly higher than the water bath ($P < 0.0001$) and air warming ($P < 0.0001$).

Figure 2-6 G shows the recovery rates of the Jurkat cells at the liquid nitrogen cooling process. Air warming achieved the recovery rate at $0.94 \pm 1.70\%$, while water bath and electromagnetic warmings are $1.41 \pm 0.89\%$ and $4.54 \pm 0.65\%$. The recovery rate of EM rewarming is significantly higher than the water bath ($P < 0.0001$) and air warming ($P = 0.0007$).

2.3.4 *Determination of the metabolic activity of the post-thawed cells*

The post-thawed Jurkat cell metabolic activity of each experimental group is shown in Figure 2-7.

Figure 2-7 A shows the normalized cell metabolic activity of the cooling rate at 0.1 ℃ min^{-1}. The trends of metabolic activity appeared to be similar for both the water bath and air warming, while EM warming shows increased cell metabolic activity over time.

Figure 2-7 B shows the normalized cell metabolic activity of the cooling rate at 0.5 ℃ min^{-1}. All of the three rewarming methods showed similar trends in the increased cell metabolic activity over time.

Figure 2-7 C shows the normalized cell metabolic activity of the cooling rate at 1 ℃ min^{-1}. All of the three rewarming methods showed similar trends in the increased cell

metabolic activity over time. Start from day 2, and the metabolic activities are comparable to the positive control group.

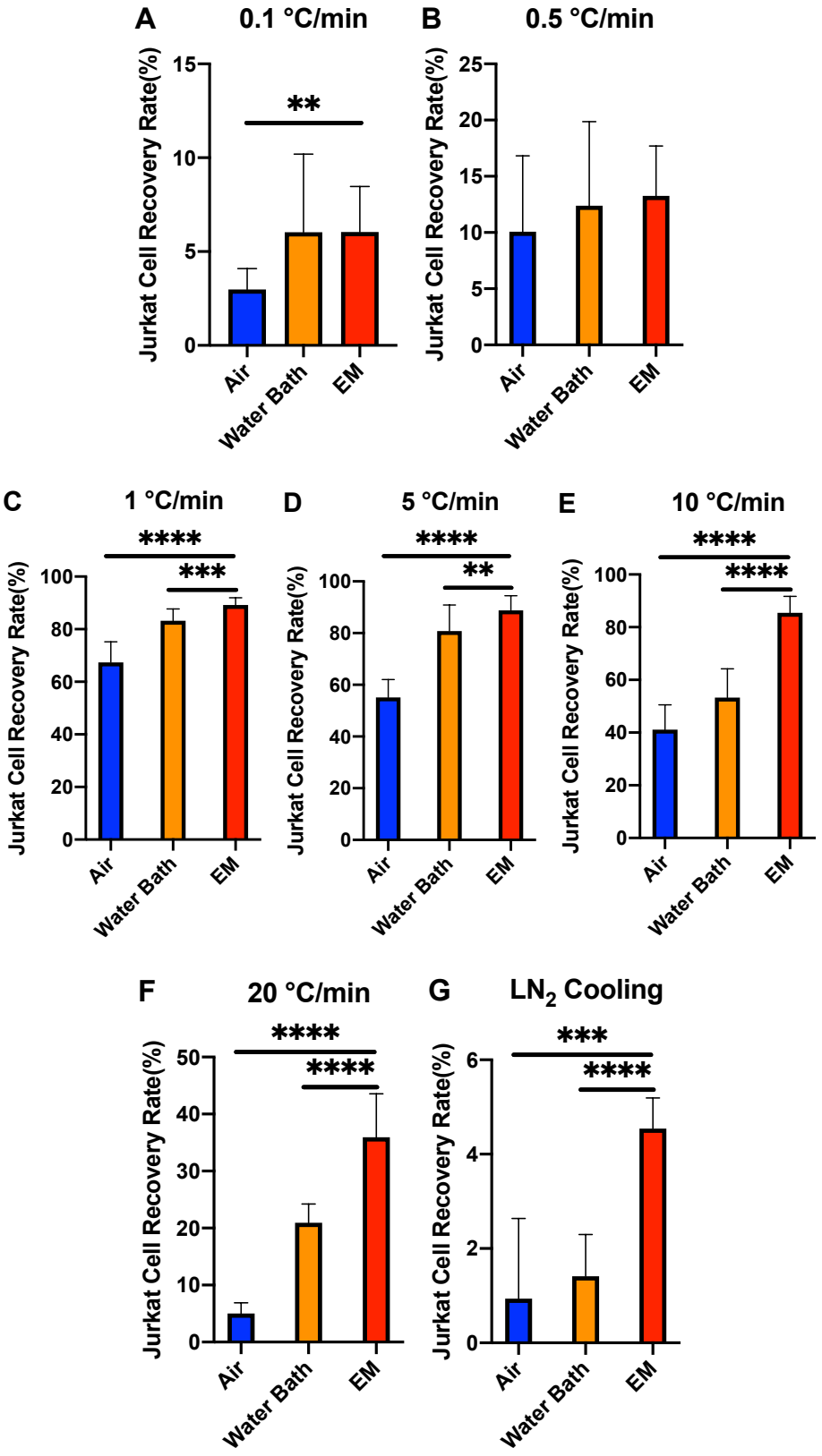

Figure 2-6. The recovery rate of the cells at different cooling and warming processes

Figure 2-7 D shows the normalized cell metabolic activity of the cooling rate at $5\ ℃\ \mathrm{min}^{-1}$. While all of the three rewarming methods showed similar trends on the increased cell metabolic activity over time, the EM rewarming is higher than water bath and air warming.

Figure 2-7 E shows the normalized cell metabolic activity of the cooling rate at $10\ ℃\ \mathrm{min}^{-1}$. The EM warming appeared to show increased metabolic activity over time, while water bath and air warming showed similar trends.

Figure 2-7 F shows the normalized cell metabolic activity of the cooling rate at $20\ ℃\ \mathrm{min}^{-1}$. The EM warming and water bath appeared to show increased metabolic activity over time, while the air warming resulted in a small increment every day.

Figure 2-7 G shows the normalized cell metabolic activity of the liquid nitrogen cooling process. All of the three rewarming methods resulted in almost no cell metabolic activity from day 0 to day 3.

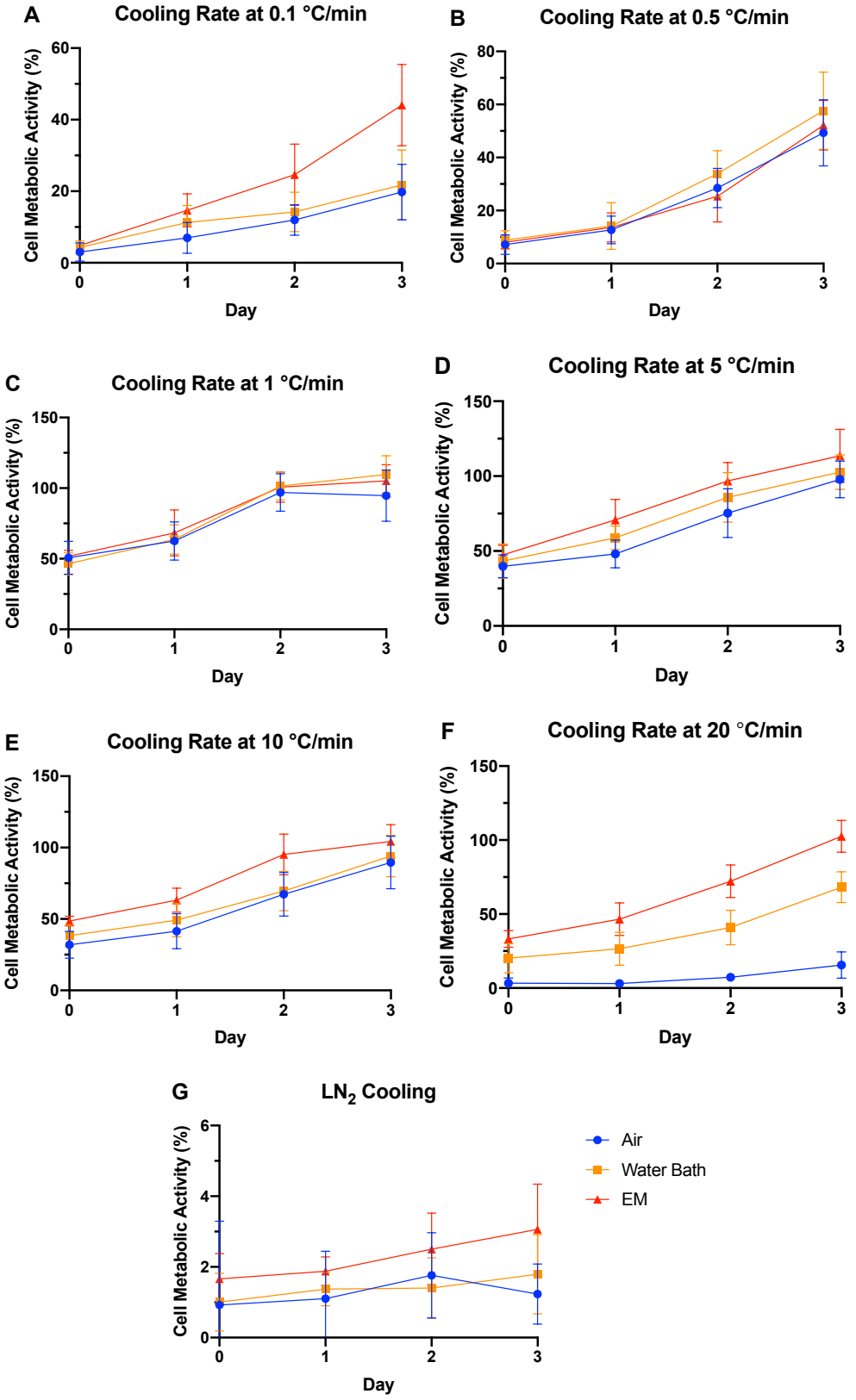

Figure 2-7. The cell metabolic activity at different cooling and warming combinations

2.4 DISCUSSION

In most of the clinical applications and fundamental researchers, the water bath rewarming is considered as the gold standard rewarming method in the cryopreservation due to its convenience and easy access. However, the limited warming rate restrained the further application of the water bath. The importance of the warming rate can be discovered from the experimental results.

For the cooling rate at $1\ ℃\ \mathrm{min}^{-1}$, all of the three rewarming methods achieved the highest recovery rates of the Jurkat cell. Among the different warming methods, the EM system with the fastest thawing process showed statistical significance in the rewarming rate and survival rate than the other two approaches. The high survival rate implies the optimal cooling rate of the Jurkat cell is around $1\ ℃\ \mathrm{min}^{-1}$. The results matched the previous study on the cooling process of the Jurkat cell. When the cooling rate increased, the recovery rate of the Jurkat cell significantly dropped with the water bath and air warming. The EM warming maintained a much higher recovery rate at rapid cooling, proved that the rapid thawing could protect the cells by preventing the recrystallization during the warming process. Though a fast cooling rate may induce the formation of intracellular ice in the freezing, the rapid warming stopped the aggregation of intracellular ice from forming larger crystals. Thus, part of the cells was rescued during the warming process. In slow warmings like a water bath or natural air convection, there is sufficient time for the development of large ice crystals resulting in the low survival rate of the cells. At the liquid nitrogen cooling process, all of the warming methods achieved a very low survival rate. The result implied the ultrafast freezing caused the rupture of the cells during the cooling due to a large amount of intracellular ice. In other words, the cells were killed before the warming rate. Therefore, even a rapid rewarming rate cannot recover the dead cells.

For the slower cooling rate, the recovery rate of the different warming groups also dropped. A slower cooling process allows the water to transport to the outside of the cell membrane. As a result, a higher concentration of the solute inside the cell caused the solute injury. Despite the small amount of remaining water within the cell, rapid warming can still avoid recrystallization. Therefore, in comparison to the water bath and air warming, the EM system succeeds the highest recovery rate at the slow cooling process.

The post-thawed Jurkat cell metabolic activity of each cooling rate and rewarming rate combination was quantified by alamarBlue assay normalized by each group's positive control for 3 days. The gradual increase in absorbance over time showed continued biological functions of the Jurkat cells after cryopreservation. Except for the liquid nitrogen cooling process, the EM warming achieved an increase of the metabolic activity in all of the other cooling rates and even comparable or surpassed the positive control group at the 1, 5, 10, and 20 $℃\ \mathrm{min}^{-1}$ rates. The results proved the successful preservation of the biological functionality of the cells by the rapid thawing. Water bath and air warming also reached increased metabolic activity in most of the cooling rates. However, the percentage of the absorbance was lower than the EM system. The trends are consistent with the membrane integrity results.

2.5 CONCLUSIONS

In this chapter, the effects of the rewarming rates on cryopreserved samples cooled with various cooling rates were determined. Jurkat cells were cooled at different rates and then warmed with natural air convection, water bath, and electromagnetic resonance system. The recovery rate of the cells and post-thawed metabolic activity were measured to evaluate the preservation of the

biological functionalities. Results showed the rapid warming achieved a higher survival rate of the cells and better metabolic activity over time in both slow and fast cooling processes.

Chapter 3. DEVELOPMENT OF THE ELECTROMAGNETIC RESONANCE REWARMING SYSTEM

In a successful cryopreservation protocol, rapid heating is desirable to avoid recrystallization. When trying to preserve large scale biological systems, such as tissues and organs, uniformed warming is also critical to prevent severe mechanical injury caused by thermal stress. Warming by conduction is not feasible due to the slow warming and large temperature gradients within the sample, leading to structural damage to the cells. Additionally, conductive warming may also overheat the outer layers while the core part remains frozen. Thus, electromagnetic warming technology seems to be the only practical approach to rapid and uniform heating of large biomaterials.

To design and development of such an electromagnetic rewarming system, knowledge of interactions between applied electromagnetic filed and the biological samples are needed. Because of the presence of the sample solution, the established electromagnetic field inside the resonant cavity will be distorted. Multiple factors will affect the outcome of the rewarming, including the resonant frequency, geometric size, and shape of the sample, electrical and thermal properties, etc. To obtain a better understanding of the electromagnetic heating, both theoretical and experimental studies are required. There are two major advantages of theoretical study. First, with the numerical modeling, the detailed filed pattern and temperature profile within the sample can be calculated and analyzed. Second, simulation allows us to change the system configurations, test conditions, and sample parameters. It is a cost-effective way to study electromagnetic warming under various conditions. The results could be served as guidelines for the experimental approach.

Prior to the establishment of the model, some critical physical properties of the sample solution are required. The procedure of properties measurement and the following numerical simulation of the electromagnetic resonance rewarming will be discussed in this chapter.

3.1 DETERMINATION OF THE DIELECTRIC PROPERTIES OF THE CPA SOLUTIONS

The dielectric properties of the biosamples are the electrical factors that describe the relations between applied electromagnetic fields and molecular charge distributions [64]. Combine with thermal properties, the dielectric properties play key roles in the absorption of the electromagnetic energy and affect the temperature profile inside the samples [65, 66]. Besides, the dielectric properties are sensitive to the temperature. In most cases, the higher temperature, the higher absorbability of the electromagnetic power. Therefore, in the thawing process, the warmer area absorbs more heat to further increase the temperature while the colder area remains a low temperature. Eventually, the increased temperature gradient will induce the thermal stress that tears up the biomaterials, especially for the large tissues and organs. Thus, it is important to measure the dielectric properties to optimize the electromagnetic heating system.

3.1.1 *Cavity perturbation method*

The transmission and reflection techniques are commonly used in the biomedical fields to measure the dielectric properties of biomaterials [67-71]. However, a fixed material without morphological change is required to apply these methods. In the case of cryopreservation, the broadly interested temperature zone covers from subzero to the body temperature that directly involves the phase change of the biosamples. Hence, transmission and reflection methods do not work for the electromagnetic system. To measure the small signals at a low temperature for biomaterials, accurate equipment with high sensitivity is needed. The cavity perturbation method

has been adopted to measure the dielectric properties of various materials due to its capability to capture the low loss dielectric materials [72-75]. Marsland measured three perfusion solutions, including HP6 + glycerol, EC1 + glycerol, and MS + DMSO, from -30 ℃ to 20 ℃ with an open-ended coaxial probe [76]. Evans measured the dielectric properties of glycerol, propylene glycol, ethylene glycol, and dimethyl sulfoxide in several aqueous concentrations that were high enough to allow supercooling. The temperature and frequency were ranging from -80 ℃ to 20 ℃ and 100 MH to 2GHz [77]. Evans also proposed a new index in terms of the dielectric properties of CPA to characterize the uniformity of the electromagnetic field during the warming. Relative dielectric property of 50% DMSO solution was tested at the temperature from -75 ℃ to 20 ℃ and frequencies from 27 MHz to 2.954 GHz [78]. Robinson measured the dielectric properties of ethanediol, dimethyl sulfoxide, 2,3-butanediol, and propane-1,2 solutions at 434 MHz and temperatures from -70 ℃ to 10 ℃ [65].

In this section, a resonant chamber was designed to measure the dielectric properties at 434 MHz. The fundamental principle of the resonant cavity perturbation method is to measure the cavity characteristics before and after a sample has been added. By measuring the change of the resonant frequency Δf and inverse of the quality factor $\Delta(\frac{1}{Q})$, the dielectric property of the sample solution was obtained. The theoretical derivation is shown in the following equations [79, 80],

$$\frac{\Delta\tilde{\omega}}{\tilde{\omega}} = \frac{\Delta f}{f_0} + \frac{i}{2}\left(\frac{1}{Q} - \frac{1}{Q_0}\right) \tag{3.1}$$

$$\frac{\Delta\tilde{\omega}}{\tilde{\omega}} = \frac{\int_{V_s}(\Delta\varepsilon\mathbf{E}\mathbf{E}_\mathbf{0}^* + \Delta\mu\mathbf{H}\mathbf{H}_\mathbf{0}^*)dV}{\int_{V_c}(\varepsilon\mathbf{E}\mathbf{E}_\mathbf{0}^* + \mu\mathbf{H}\mathbf{H}_\mathbf{0}^*)dV} \tag{3.2}$$

where $\tilde{\omega}$ is the complex augular frequency of the cavity, f_0 is the resonant frequency of the empty chamber, Q_0 is the quality factor of the empty chamber, V_s is the volume of the sample, V_C is the

volume of the chamber, $\mathbf{E_0}$ and $\mathbf{H_0}$ are electric and magnetic fields inside the empty chamber, **E** and **B** represent electric and magnetic fields inside the chamber with the sample added, ε and μ are complex permittivities and permeability of the sample, and i is the imaginary number. For a non-magnetic sample, μ is equivalent to the permeability of free space μ_0. Then, the eq. (3.2) can be simplified

$$\frac{\Delta\tilde{\omega}}{\tilde{\omega}} = -(\varepsilon_r - 1)\frac{\int_{V_s}(\mathbf{E}_{\text{int}}\mathbf{E}_\mathbf{0}^*)dV}{2\int_{V_c}|\mathbf{E}_0|^2 dV} \tag{3.3}$$

$$\varepsilon_r = \varepsilon' - i\varepsilon'' \tag{3.4}$$

where $\mathbf{E}_{\text{int}}$ stands for the incident electric field within the sample. ε_r is the relative permittivity of material and calculate by the permittivity ε divided by the permittivity of the free space ε_0. ε' is the real part of the relative permittivity, or called the dielectric constant. It describes the amount of polarization and characterizes the electromagnetic power stored in the material. ε'' is the imaginary part of the relative permittivity, or called the dielectric loss. It describes the amount of loss at a given frequency and characterizes the electromagnetic power dissipation. Substituting eq. (3.4) into eq.(3.3),

$$\frac{\Delta\tilde{\omega}}{\tilde{\omega}} = -(\varepsilon_r - 1)\frac{\int_{V_s}\mathbf{E}_{\text{int}}\mathbf{E}_\mathbf{0}^* dV}{2\int_{V_c}|\mathbf{E}_0|^2 dV} = -(\varepsilon_r - 1)\frac{\int_{V_s}\mathbf{E}_{\text{int}}\mathbf{E}_\mathbf{0}^* dV}{2\int_{V_c}|\mathbf{E}_0|^2 dV} + i\varepsilon''\frac{\int_{V_s}\mathbf{E}_{\text{int}}\mathbf{E}_\mathbf{0}^* dV}{2\int_{V_c}|\mathbf{E}_0|^2 dV} \tag{3.5}$$

comparing the shift of the resonant angular frequency in eq.(3.1) and (3.5), it can be obtained,

$$-\frac{\Delta f}{f_0} + \frac{i}{2}\left(\frac{1}{Q} - \frac{1}{Q_0}\right) = -\left(\frac{1}{C}\right)K(\varepsilon' - 1) + i\left(\frac{1}{C}\right)K\varepsilon'' \tag{3.6}$$

where C is proportional to $\frac{1}{V_s}\int_{V_c}\frac{|\mathbf{E}_0|^2}{|\mathbf{E}_{0,\max}|^2}$, $\mathbf{E}_{0,\max}$ is the value of the highest electric field intensity that locates at the center position of the rectangular chamber[81]. K is a shape factor that

determined by the geometry of the sample due to the different polarization over different sample shapes. Separate eq. (3.6) to obtain the following relationships,

$$\Delta f = C_1 K(\varepsilon' - 1) \tag{3.7}$$

$$\Delta(\frac{1}{Q}) = C_2 K^2 \varepsilon'' \tag{3.8}$$

where C_1 and C_2 are constants. The value of K depends on the sample shape, e.g., for a spherical sample, $K = \frac{3}{\varepsilon'+2}$.

Plugin the value gives,

$$\Delta f = k_1 \frac{\varepsilon'-1}{\varepsilon'+2} \tag{3.9}$$

$$\Delta(\frac{1}{Q}) = k_2 \frac{\varepsilon''}{(\varepsilon'+2)^2} \tag{3.10}$$

where k_1 and k_2 are unknown constants to be determined.

3.1.2 *Measurement system setup*

To measure the k_1 and k_2, a rectangular resonant cavity was designed and established. The dimension of the cavity was calculated as $680 \times 350 \times 400$ mm, resonant frequency at 434 MHz. The exterior surface wall was built with copper due to the material's high conductivity and low cost.

As shown in Figure 3-1, the measurement system consists of a resonant cavity, a network analyzer (E5061B, Agilent Technologies, Santa Clara, CA), a temperature meter (ReFlex, Neoptix, Quebec, Canada), and a fiber optic temperature sensor (TS4-02, Micronor LLC, Camarillo, CA).

In the cryopreservation, the majority of the volume in the sample solution is filled with the CPAs. Then, the CPAs dominate the physical properties of biomaterials. Hence, various CPAs at different concentrations were prepared to measure the dielectric properties.

Prior to the measurement, 25 mL of CPA solution in a cylindrical holder was frozen to -80 ℃ with a -80 ℃ freezer. Three CPA solutions were prepared, including 10% (w/v) DMSO, 10% DMSO + 0.1 M Trehalose, and 10% DMSO + 0.25 M Trehalose. During the measurement, the holder was transferred from the freezer to the center position of the cavity quickly. Slow warming is preferred to precisely capture the properties at different temperatures. Thus, the sample solution was warmed with natural convention by the surrounding air at room temperature. The change of the temperature was monitored and recorded by the fiber optic sensor installed within the holder. The network analyzer was used to track the real-time resonant frequency and reflection signal S_{11} of the sample solution during the rewarming process. An analytic method was applied to solve the quality factors at various temperatures from the recorded resonant frequencies and power reflection parameters [82].

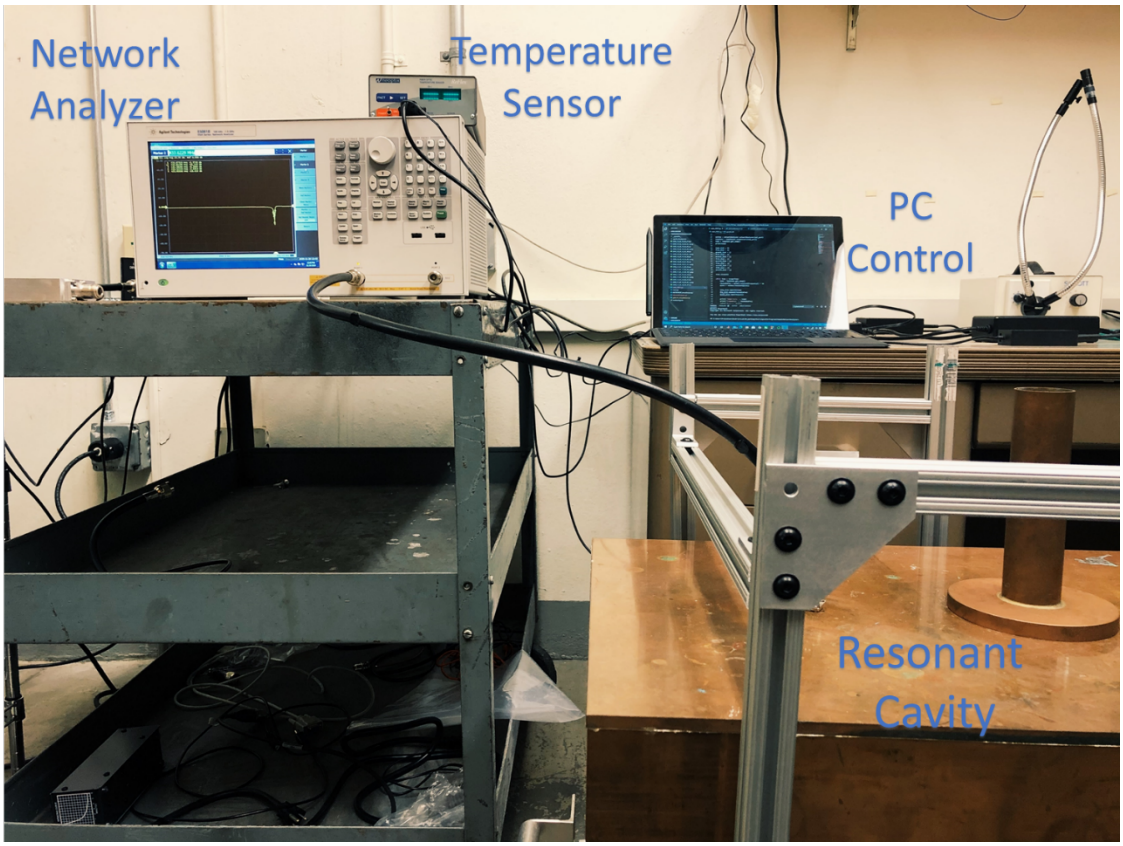

Figure 3-1. The measurement system of the dielectric properties of CPA solutions

3.1.3 *Calibration procedures*

Calibration of the newly designed resonant cavity is needed before the determination of the k_1 and k_2 constants. Water, methanol, ethanol, 1-propanol, 2-propanol, ethylene glycol, and cyclohexane solutions with known dielectric properties were used as standard solutions [53]. The dielectric properties of the standard solutions are given in Table 3-1.

Table 3-1. The dielectric properties of the standard solutions in previous literature

Solution	ε', Dielectric Constant	ε'', Dielectric loss
Water	80	1.9
Methanol	33	3.52
Ethanol	22	7.04
1-Propanol	13	8.57
2-Propanol	12	8.08
Ethylene glycol	36	12.09
Cyclohexane	2.02	0

Figure 3-2 shows the change of the resonant frequency before and after the insertion of the standard solutions. Figure 3-3 shows the change of the inverse of the quality factor. The correlation factor R^2 was calculated as 0.9938 for the fitting of the resonant frequency and 0.9914 for the inverse of the quality factor to validate the goodness of fit. Then k_1 and k_2 can be determined from the slope as 0.9867 MHz and 0.0089.

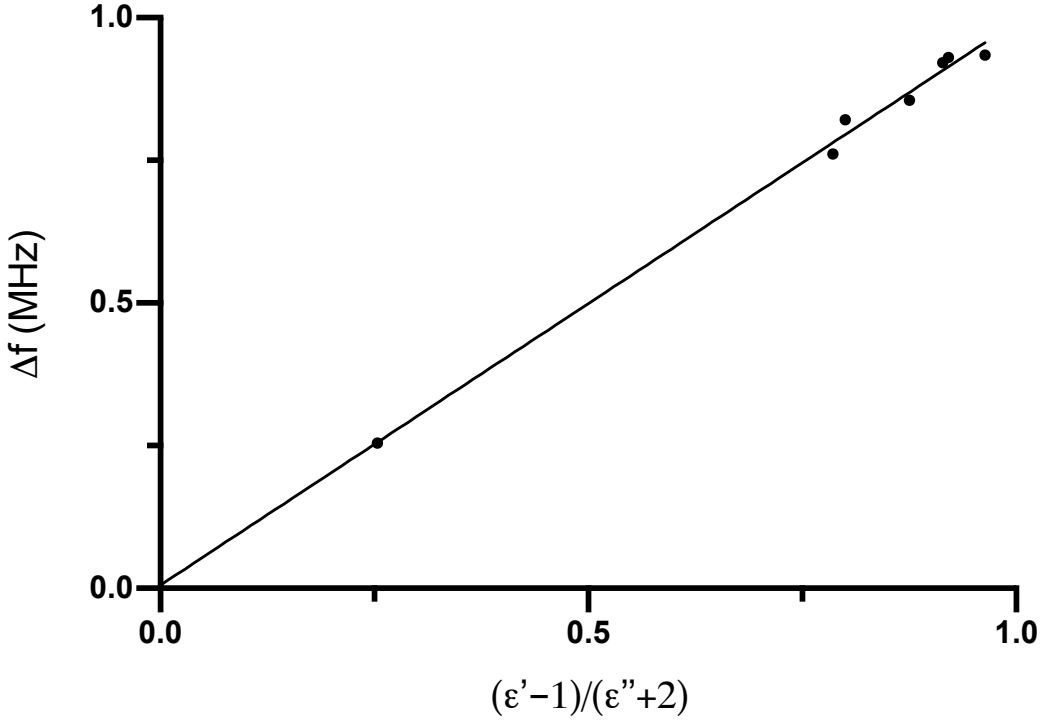

Figure 3-2. The change of resonant frequency after the insertion of standard solutions

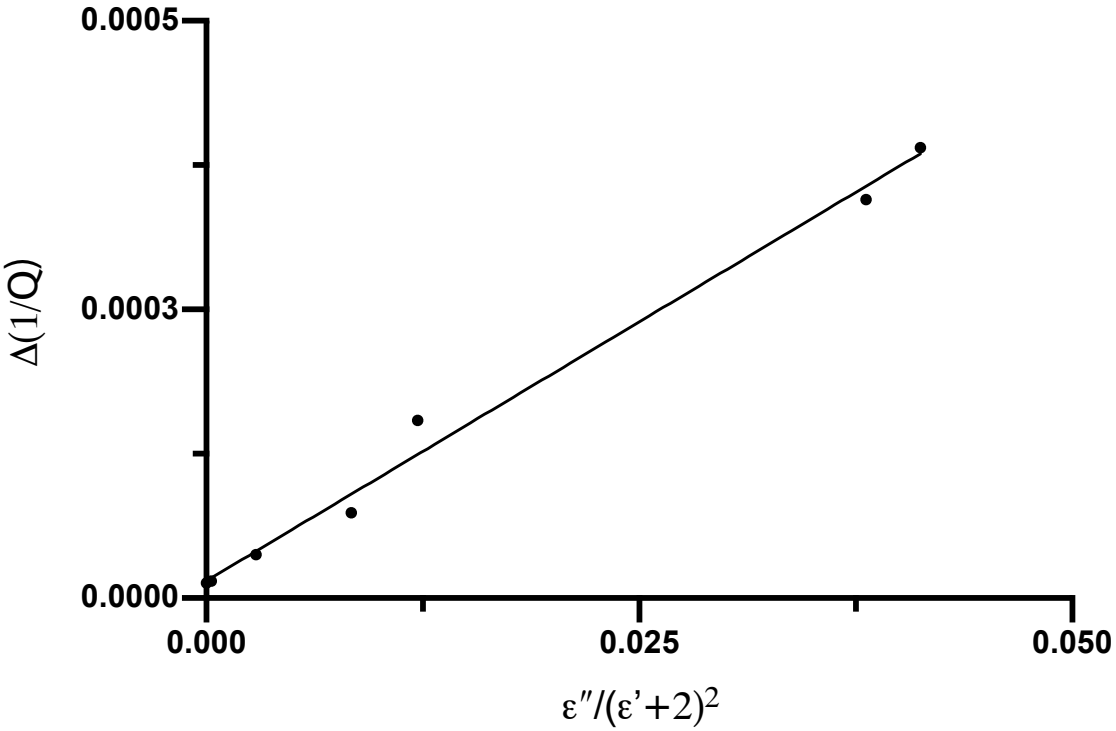

Figure 3-3. The change of inverse of the quality factor after insertion of standard solutions

Once k_1 and k_2 have been obtained, the calibration process is done, and the measurement system is ready to use.

3.1.4 *Results and discussion*

Figure 3-4 shows the dielectric constant, ε', of the CPA solutions versus temperature. For all of the tested CPA solutions, the dielectric constant increased as the temperature increased from -120 ℃ to 0 ℃. Figure 3-5 shows the dielectric loss, ε'', versus temperature. The distribution of the electromagnetic power decreased exponentially from the boundary to the center location. To define the distance that the electromagnetic power has decreased to 1/e of the initial magnitude at the surface, a new property, penetration depth, is introduced. After obtaining the dielectric properties, ε' and ε'', penetration depth can be calculated [83],

$$\delta = \frac{c}{2\pi f \sqrt{\frac{\varepsilon'}{2}\left[\sqrt{1+(\frac{\varepsilon''}{\varepsilon'})^2}-1\right]}} \tag{3.11}$$

The addition of the trehalose raised the dielectric constant of the DMSO solutions, especially between -70 ℃ to 0 ℃. The dielectric loss describes the ability of the sample solution to absorb the electromagnetic power and affect the rewarming rate during the thawing process. The larger the dielectric loss, the more energy is absorbed by the sample solution indicating a higher rewarming rate. From the measurement results, the dielectric loss of all tested solutions increased with the temperature until a peak value was reached at around -15 ℃, which indicates the rewarming rate improved as the temperature increased till to the phase change temperature region. Similar to the dielectric constant, the addition of the trehalose also boosted the dielectric loss of the DMSO solution. However, that doesn't mean the higher concentration of trehalose is always better due to the osmotic injury to the biomaterials.

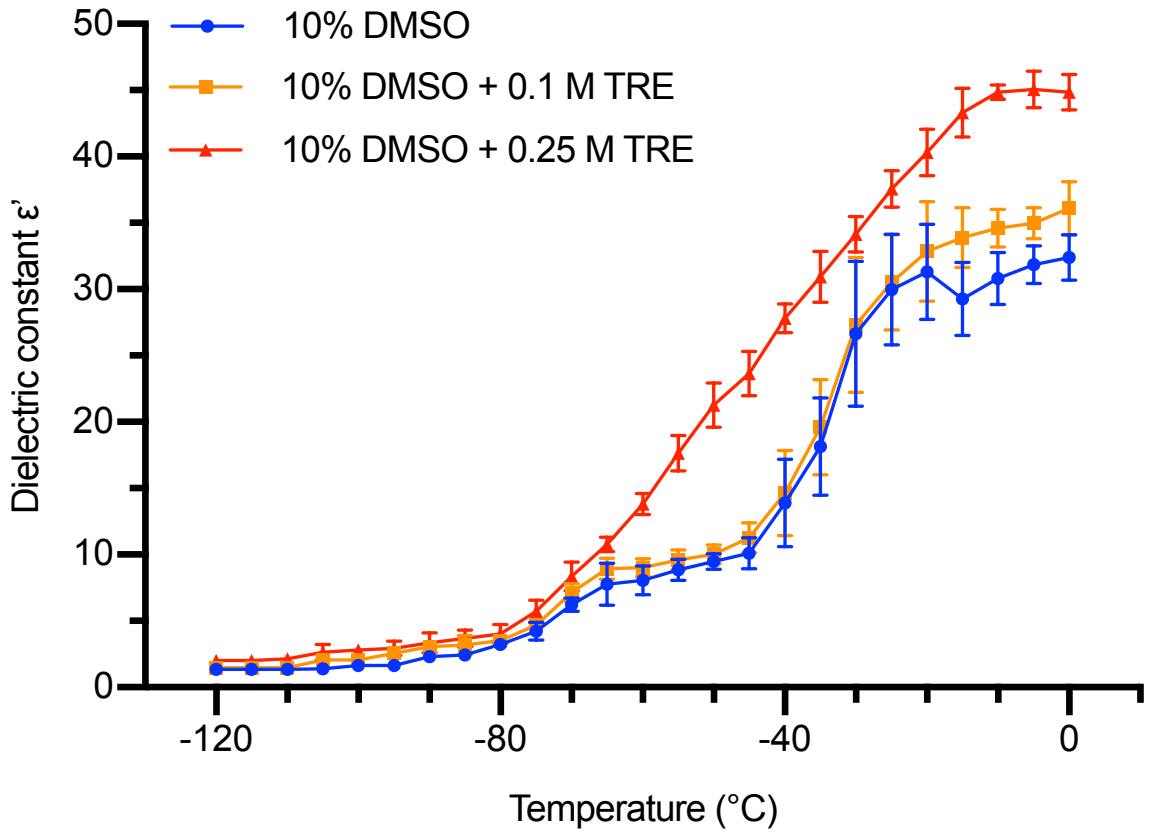

Figure 3-4. Dielectric constant, ε', versus temperature for 10% DMSO, 10% DMSO + 0.1 M Trehalose, and 10% DMSO + 0.25 M Trehalose. The mean values $\pm$ standard deviations at each temperature point were determined based on four replicates (n=4).

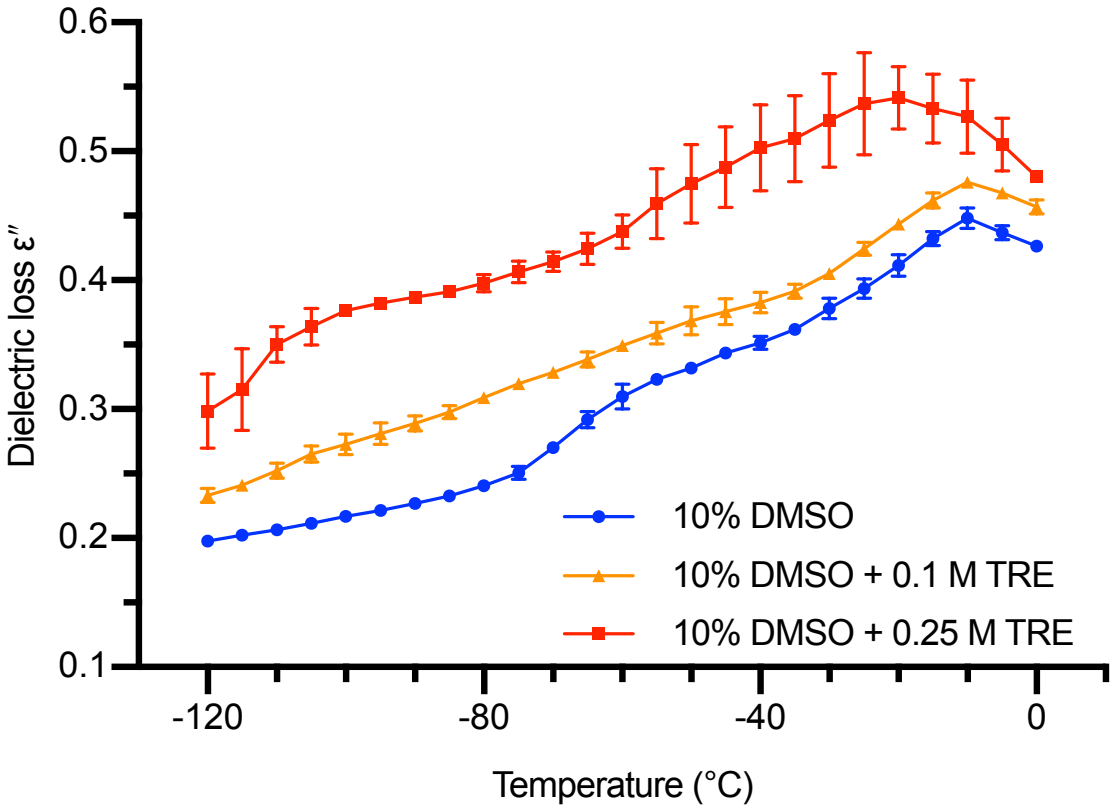

Figure 3-5. Dielectric loss, ε'', versus temperature for 10% DMSO, 10% DMSO + 0.1 M Trehalose, and 10% DMSO + 0.25 M Trehalose. The mean values $\pm$ standard deviations at each temperature point were determined based on four replicates (n=4).

3.2 DETERMINATION OF THE THERMAL PROPERTIES OF CPA SOLUTIONS

Electrical properties characterize the absorption of electromagnetic power. The energy dissipation as heat within the sample solution is determined by the thermal properties. Thermal conductivity, K, denotes the materials' ability to conduct the heat. Heat capacity, C_P, defines the amount of energy needed to produce a unit change of sample's temperature. Since major parts of the interesting temperature range in the cryopreservation are below zero, the potential phase change of the CPA solutions and biomaterials are involved, it is essential to determine the thermal properties at the low-temperature region to better analyze and utilize the electromagnetic power.

3.2.1 *Thermal conductivity*

Thermal conductivities of the previous CPA solutions were measured with a thermal-needle approach using a microfabricated thermal conductivity sensor. The sensor was designed by former lab members Liang at el [84], and assembled in a cleanroom. As shown in Figure3-6, the other components in the measurement system including, CryoMed controlled rate freezer, a digital multimeter, and a data acquisition system(Integra 2700, Keithley, Cleveland, OH).

The freezer was used to create a uniform thermal environment at different temperatures. The Keithley multimeter sent a constant small testing current to the thermal conductivity sensor and then captured the voltage response. The data acquisition system recorded the responses and converted them to resistance using Ohm's law. Thermal conductivity was calculated from the following equation,

$$K = \left(\frac{E_C^2 \alpha}{4\pi L}\right)\left(\frac{R_0}{R}\right) / \left(\frac{dR}{dln(t)}\right) \tag{3.12}$$

where E_C stands for the constant testing current flow from the multimeter. L is the effective length of the measuring element. R_0 is the resistance at the initial measurement. R is the resistance at the final measurement.

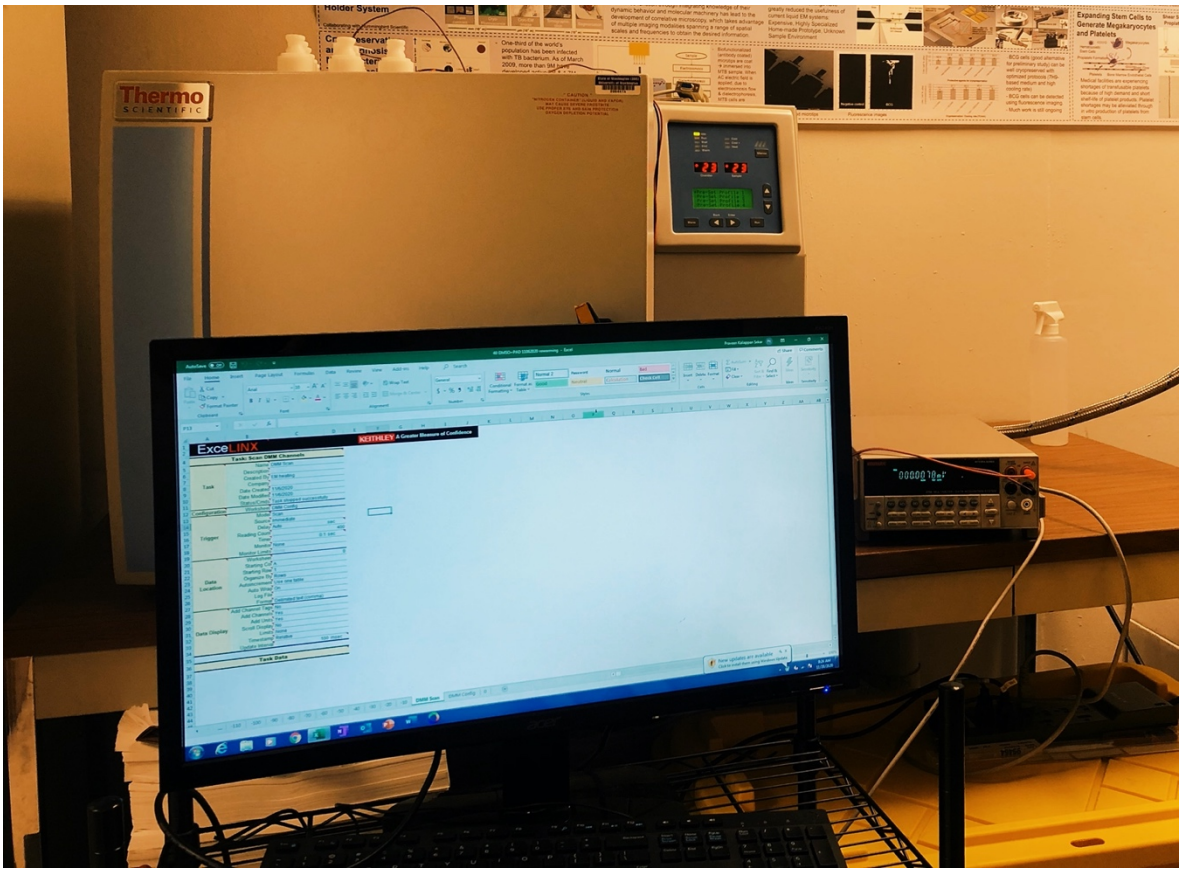

Figure 3-6. The measurement system of thermal conductivity

CPA solutions were loaded to a 25 mL cylindrical sample holder. The thermal conductivity of the sample solutions was determined from -120 ℃ to 0 ℃.

3.2.2 *Heat capacity*

Similar to thermal conductivity, heat capacity is also a temperature-dependent property. As shown in Figure 3-7, a differential scanning calorimetry (DSC 8500, Perkin Elmer, Waltham, MA) was used to precisely measure the difference of the heat flow between the CPA solutions and

reference solution. The isothermal step scan method was adopted to reduce the experimental inaccuracy. The heat capacity was calculated from the following equation,

$$C_P = \frac{\Delta Q_{DSC}}{m\Delta T} \tag{3.13}$$

where ΔQ_{DSC} is the heat flow through the sample solutions captured by DSC. m stands for the mass of the sample. T is the temperature.

Figure 3-7. The measurement system setup of the heat capacity

Measurements of each sample solution were repeated three times. The heat capacity was calculated from -120 ℃ to 0 ℃.

3.2.3 *Results and discussion*

Figure 3-8 shows the thermal conductivity of tested CPA solutions at different temperatures. For all of the three CPA solutions, the thermal conductivity decreased as temperature increased from −120 ℃ to 0 ℃. The mean values ± standard deviations at each temperature point were determined based on four replicates (n=4).

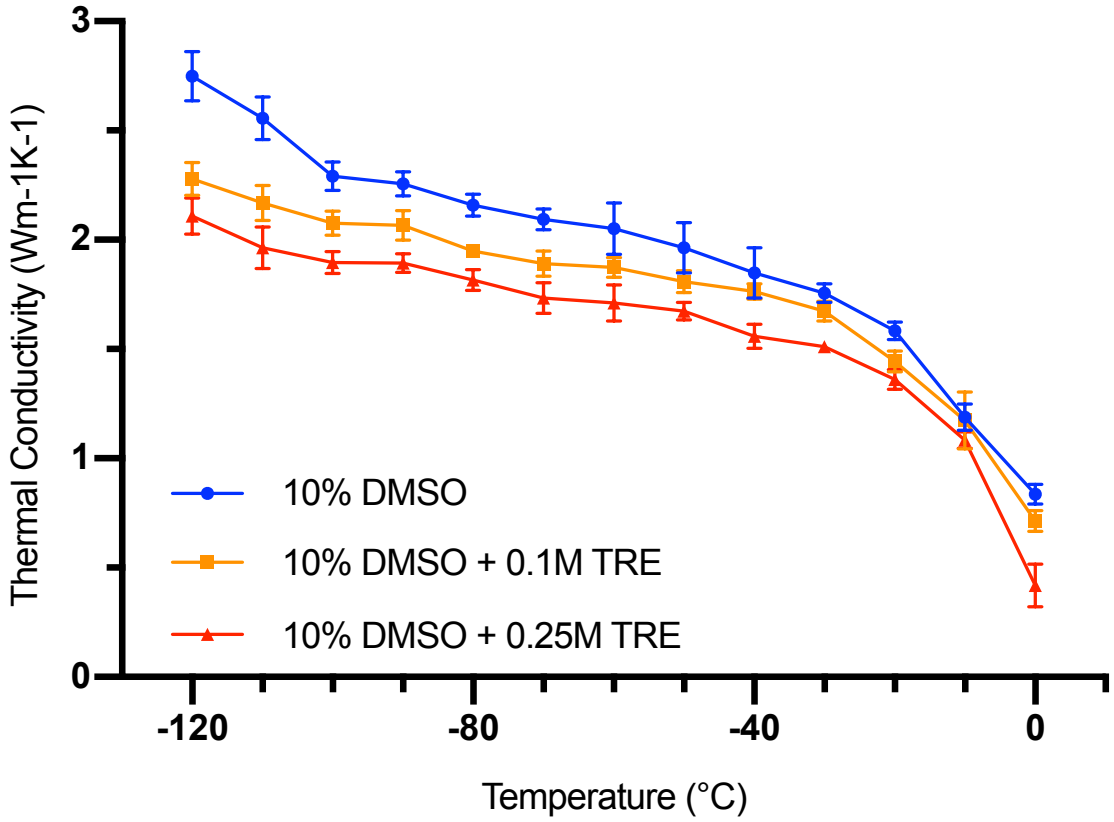

Figure 3-8. Thermal conductivity, K, versus temperature for 10% DMSO, 10% DMSO + 0.1 M Trehalose, and 10% DMSO + 0.25 M Trehalose

Thermal conductivity characterizes the heat transfer by conduction within the biological samples. When using electromagnetic power as the heat source, the combined heat transfer equation can be presented as,

$$\rho C \frac{\partial T}{\partial t} = \nabla \cdot (K \nabla T) + \pi f \varepsilon_0 \varepsilon'' |E|^2 \tag{3.14}$$

where ρ (kg m^{-3}) is the density of the sample solution, C (J $kg^{-1}K^{-1}$) is the specific heat capacity, K (W $m^{-1}K^{-1}$) is the thermal conductivity, capital T (K) is the temperature, and small t (s) is the time. The second term on the right-hand side represents the electromagnetic power absorbed by the sample solutions.

The measurements results of the specific heat capacity of the CPA solutions are shown in Figure 3-9. The mean values ± standard deviations at each temperature point were determined based on four replicates (n=4).

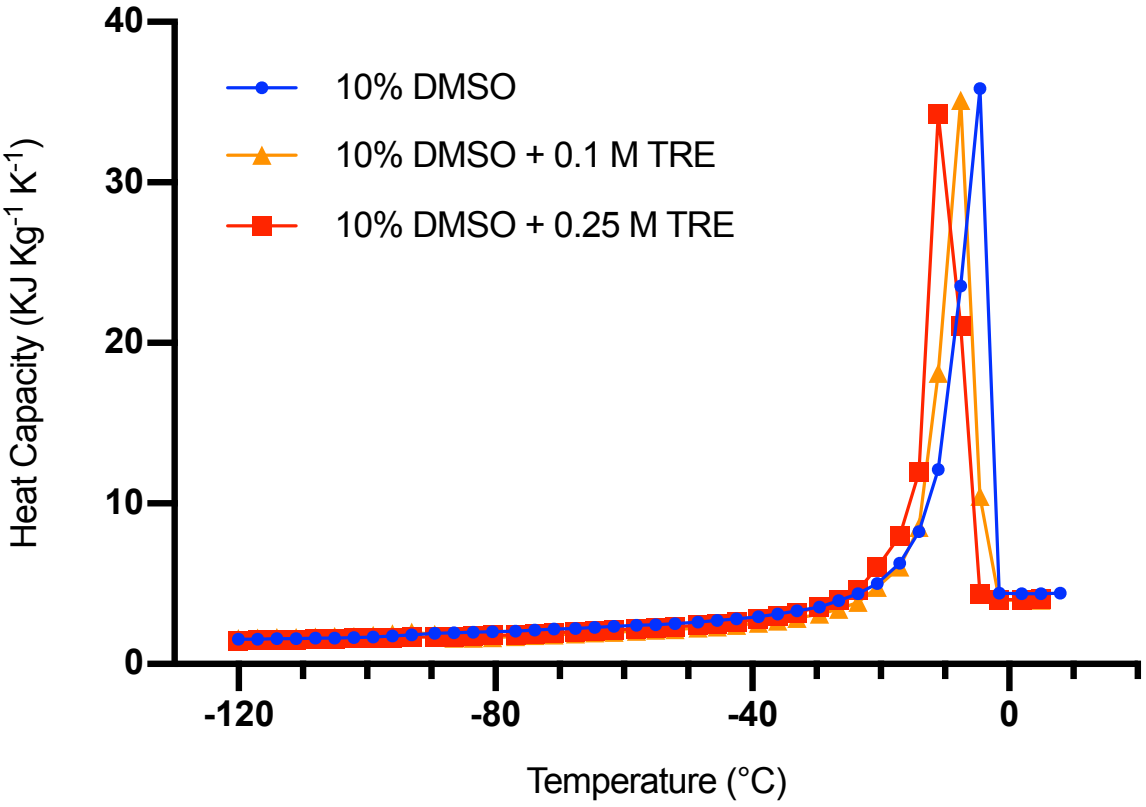

Figure 3-9. Specific heat capacity, C_P, versus temperature for CPA solutions

Due to the considerable amount of heat required during phase transition, the heat capacity has a larger impact on the numerical simulation of the electromagnetic rewarming model. The

latent heat of CPA solutions may deeply affect the warming rate during the phase change region. No significant difference was observed in the measurement of heat capacity among the three CPA solutions. The addition of the trehalose in 10% DMSO solution slightly decreased the temperature of the peak Cp value.

Based on the analysis of the tested electrical and thermal properties, 10% DMSO + 0.25 M trehalose solution has the highest absorption of electromagnetic energy and a relatively low heat capacity. The results implied 10% DMSO + 0.25 M trehalose solution might achieve the fastest warming rate in the electromagnetic heating.

3.3 NUMERICAL SIMULATION OF ELECTROMAGNETIC FIELDS AND HEATING PROCESS IN THE ELECTROMAGNETIC RESONANT CAVITY

3.3.1 *Introduction*

Prior researchers have tried different setups of the electromagnetic cavity for the rapid and uniform rewarming of the biological samples. Evans [85], Pegg [53], and Luo [86] have built the cavity that resonant around 434 MHz. Evans and Pegg's cavity worked under multimode, while Luo adopted the single mode. The advantages of the multimode cavity are fewer limitations to the sample position and volume. A multimode cavity can be treated as the superposition of the multiple plane waves impinging on the biomaterial from different directions. The distribution of the electric field is nearly homogeneous at every position in the cavity. Therefore, there is no specific position that the sample has to be placed or restrictions on the sample's size and shape. However, it is extremely hard to calculate and monitor the resonant state due to the various power input. On the other hand, the field intensity can be analyzed precisely for a single mode cavity. Additionally, the peak value of the electric field in the single mode cavity is much larger than the multimode one.

Though, a cryopreserved specimen has to be placed at the central location with the strongest electromagnetic field to achieve fast thawing. Plus, the volume of the sample was limited to the appropriate size based on the analysis of the electromagnetic filed distribution to avoid the large temperature gradient. Thus, further improvements are needed before the experimentally study with the actual CPA solutions and biomaterials.

A variety of numerical techniques have been developed to perform the theoretical studies for the design of electromagnetic rewarming systems [87-89]. Three methods are the most widely used, including (1) the finite difference time domain (FDTD) method, (2) the method of moment (MOM), and (3) the finite element method. FDTD method was used to obtain the temperature distribution of the electromagnetic rewarming [90]. In spite of the accurate computation, FDTD consumes too much computing resources due to the required tiny grids over the entire computational domain. MOM was used to predict the distribution of the electric field [88]. Though the moment method is a great technique for analyzing the homogeneous dielectrics in the frequency domain, it is not suited to the analysis of complex inhomogeneous geometries, i.e., single mode resonant cavity. A simulation model of electromagnetic rewarming assisted with superparamagnetic nanoparticles was conducted [91]. However, the large power input of 8000 W to reach the sufficient warming rate is not achieveable in the real world test [92]. Ma [93] and Torres [94] solved Maxwell's question with the FDTD method and calculated the temperature profile of a dielectric sample within a rectangular holder. Pathak simulated various feed options with a multi-grid 3D FDTD and finite-difference heat transfer model [95]. In Zhang's research, a 3D numerical model was used to predict the electromagnetic field distribution, power distribution, and temperature profile of the sample solution inside a microwave cavity [96]. In this section, a

numerical model based on the finite element method with electromagnetic wave propagation and heat transfer theories was built and validated.

3.3.2 *Governing equation and theoretical background*

For a nonmagnetic sample with the following electrical parameters, complex electric permittivity, ε, F m^{-1}; electrical conductivity, σ, S m^{-1}; and magnetic permeability of the free space, $\mu = \mu_0$, H m^{-1}. The distribution of the electric field can be obtained through the Maxwell equations on the frequency domain,

$$\nabla \times \mathbf{E} = -j\omega\mu\mathbf{H} - \mathbf{M} \tag{3.15}$$

$$\nabla \times \mathbf{H} = j\omega\varepsilon\mathbf{E} + \sigma\mathbf{E} + \mathbf{J} \tag{3.16}$$

where $\mathbf{E}$ (V m^{-1}) is the electric field intensity, $\mathbf{H}$ (A m^{-1}) is the magnetic field intensity. $\mathbf{M}$ (A m^{-1}) and $\mathbf{J}$ (A m^{-2}) are the equivalent primary sources that are negligible since there is no electrical or magnetic current source in the domain. ω(rad s^{-1}) is the angular frequency of the electromagnetic field. ε stands for the complex electric permittivity and $\varepsilon = \varepsilon' - i\varepsilon''$, where ε' is the dielectric constant, and ε'' is the dielectric loss that represents the ability to absorb electrical power. The density of the absorbed energy, q, is introduced,

$$q = \pi f \varepsilon_0 \varepsilon'' |\mathbf{E}|^2 \tag{3.17}$$

where f (Hz) stands for the frequency of the electromagnetic field. q (Wm^{-3}) is the energy density absorb from the electromagnetic field.

3.3.3 *Determination of the geometry of the resonant chamber*

The resonant chamber is made of copper plates because of its high electrical conductivity and relatively low cost. The resonant frequency is designed at 434 MHz with TE101 mode. To

determine the specific dimension of the chamber, Maxwell's equations were adopted. Maxwell's equations are a set of partial differential equations that are based upon Gauss's law, Gauss's law for magnetism, Faraday's law, and Ampère's law with Maxwell's addition. Within the resonant chamber where there is no electrical charges and no magnetic currents, the governing equations are,

$$\nabla \cdot \mathbf{E} = 0 \tag{3.18}$$

$$\nabla \cdot \mathbf{B} = 0 \tag{3.19}$$

$$\nabla \times \mathbf{E} = -\frac{\partial \mathbf{B}}{\partial t} \tag{3.20}$$

$$\nabla \times \mathbf{B} = \frac{1}{c^2}\frac{\partial \mathbf{E}}{\partial t} \tag{3.21}$$

$$c = \sqrt{\frac{1}{\mu_0 \varepsilon_0}} \tag{3.22}$$

where μ_0 is the permeability of the free space, and ε_0 is the permittivity of the free space. By taking the curl of eq.(3.20) and (3.21), the wave equations can be represented,

$$\frac{1}{c^2}\frac{\partial^2 \mathbf{E}}{\partial t^2} - \nabla^2 \mathbf{E} = 0 \tag{3.23}$$

$$\frac{1}{c^2}\frac{\partial^2 \mathbf{B}}{\partial t^2} - \nabla^2 \mathbf{B} = 0 \tag{3.24}$$

where $\mathbf{B} = \mu \mathbf{H}$ and $\frac{\partial^2 \mathbf{E}}{\partial t^2} = -\omega^2 \mathbf{E}$. As shown in Figure 3-10, the boundary conditions of the chamber can be defined,

$$\mathrm{E}_y = E_z = 0 \ @ \ x = 0, a \tag{3.25}$$

$$\mathrm{E}_x = E_z = 0 \ @ \ y = 0, b \tag{3.26}$$

$$\mathrm{E}_x = E_y = 0 \ @ \ z = 0, d \tag{3.27}$$

Apply the boundary conditions to the wave equations, the electric field in x, y, and z directions can be represented,

$$\mathrm{E}_x = (\frac{j\omega\mu}{h^2})(\frac{n\pi}{b})\cos(\frac{m\pi}{a}x)\sin(\frac{n\pi}{b}y)\sin(\frac{p\pi}{d}z) \tag{3.28}$$

$$\mathrm{E}_y = -(\frac{j\omega\mu}{h^2})(\frac{n\pi}{a})\sin(\frac{m\pi}{a}x)\cos(\frac{n\pi}{b}y)\sin(\frac{p\pi}{d}z) \tag{3.29}$$

$$\mathrm{E}_z = 0 \tag{3.30}$$

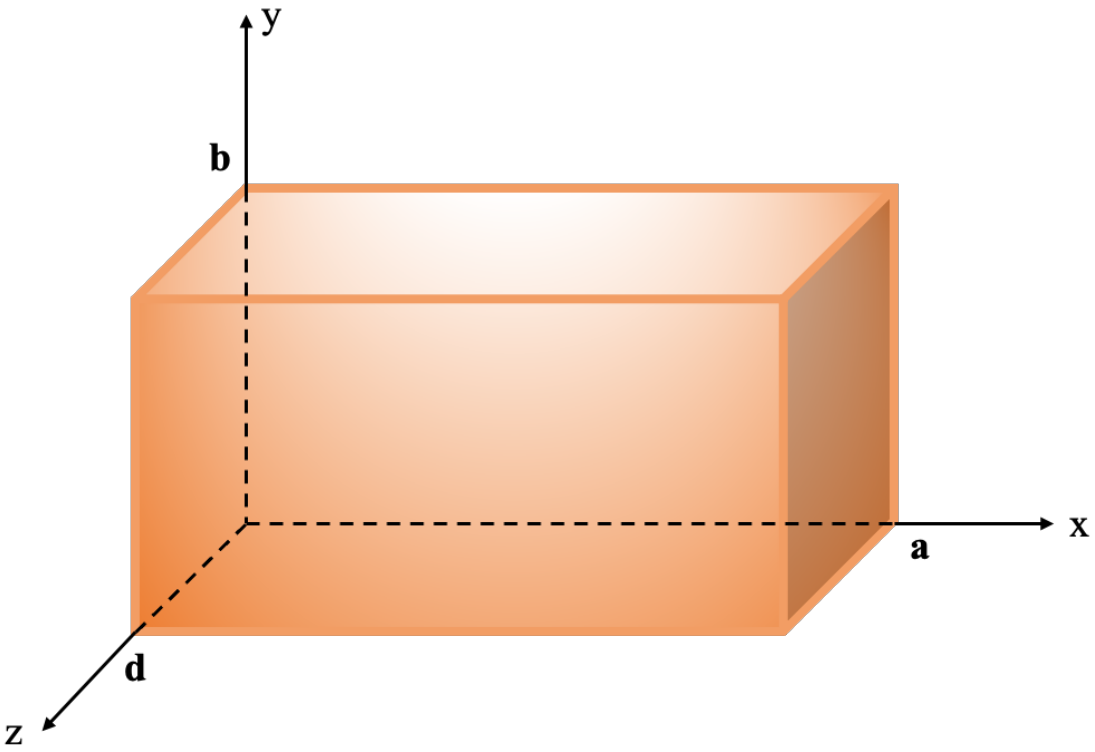

Figure 3-10. Schematic of the copper rectangular resonant cavity

The magnetic field in x, y, and z directions can be solved as,

$$\mathrm{H}_x = -H_0(\frac{1}{h^2})(\frac{m\pi}{a})(\frac{p\pi}{d})\sin(\frac{m\pi}{a}x)\cos(\frac{n\pi}{b}y)\cos(\frac{p\pi}{d}z) \tag{3.31}$$

$$\mathrm{H}_y = -H_0(\frac{1}{h^2})(\frac{n\pi}{b})(\frac{p\pi}{d})\cos(\frac{m\pi}{a}x)\sin(\frac{n\pi}{b}y)\cos(\frac{p\pi}{d}z) \tag{3.32}$$

$$\mathrm{H}_z = H_0 cos(\frac{m\pi}{a}x)\cos(\frac{n\pi}{b}y)\sin(\frac{p\pi}{d}z) \tag{3.33}$$

where m, n = 0, 1, 2 ..., p = 1, 2, 3 ... Since $h^2 = \left(\frac{m\pi}{a}\right)^2 + \left(\frac{n\pi}{b}\right)^2$, therefore, m and n cannot be 0 at the same time. The resonant frequency for TE_{mnp} modes is introduced by,

$$(f_r)_{mnp}^{TE} = \frac{1}{2\pi\sqrt{\mu\varepsilon}}\sqrt{(\frac{m\pi}{a})^2 + (\frac{n\pi}{b})^2 + (\frac{p\pi}{d})^2} \quad (3.34)$$

In this study, the TE_{101} mode was selected. The dimension of the resonant chamber was calculated as length at 680 mm, width at 350 mm, and depth at 400 mm.

3.3.4 *Numerical modeling setup*

Applying the finite element method, the numerical modeling of the electromagnetic resonant rewarming was accomplished with COMSOL Multiphysics (COMSOL Inc, Burlington, MA). As shown in Figure 3-11, the model of the rewarming system consists of the resonant cavity, the electromagnetic power input, the coaxial transmission line, the probe antenna, and the cryopreserved sample solution. Table 3-2 presents the dimension and physical properties of the rewarming system.

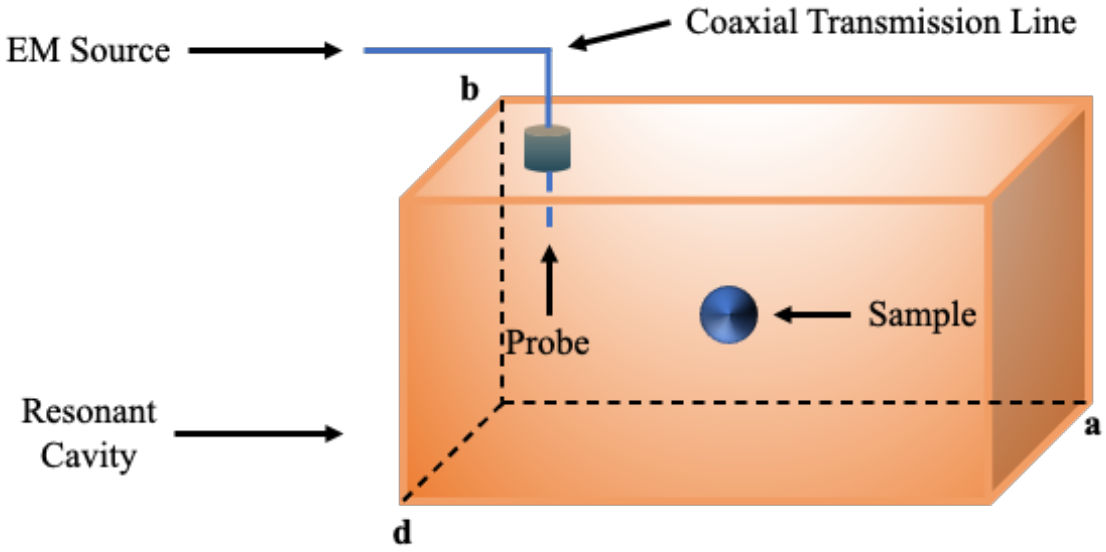

Figure 3-11. Schematic of the simulated electromagnetic resonant rewarming system

The Nyquist criterion was applied to the meshing grid of the simulation [97]. The maximum size of the element grid was constrained smaller than half of the wavelength of the electromagnetic wave. Six grids per wavelength in the finite element analysis were also employed to solve Maxwell's equation [98]. Tetrahedral grids were selected in this study due to the smaller grid size comparing to the discretization of the resonant rewarming system. Once the tetrahedron grid was applied, the grid size of the resonant chamber was calculated to be less than 10% of the wavelength of electromagnetic wave. Figure 3-12 shows the mesh preparation, different meshing approaches were adopted for different components of the system. Refined meshes were created near the boundaries of surfaces, while the area around probe antenna and central part of the sample holder were treated with the enhanced meshing.

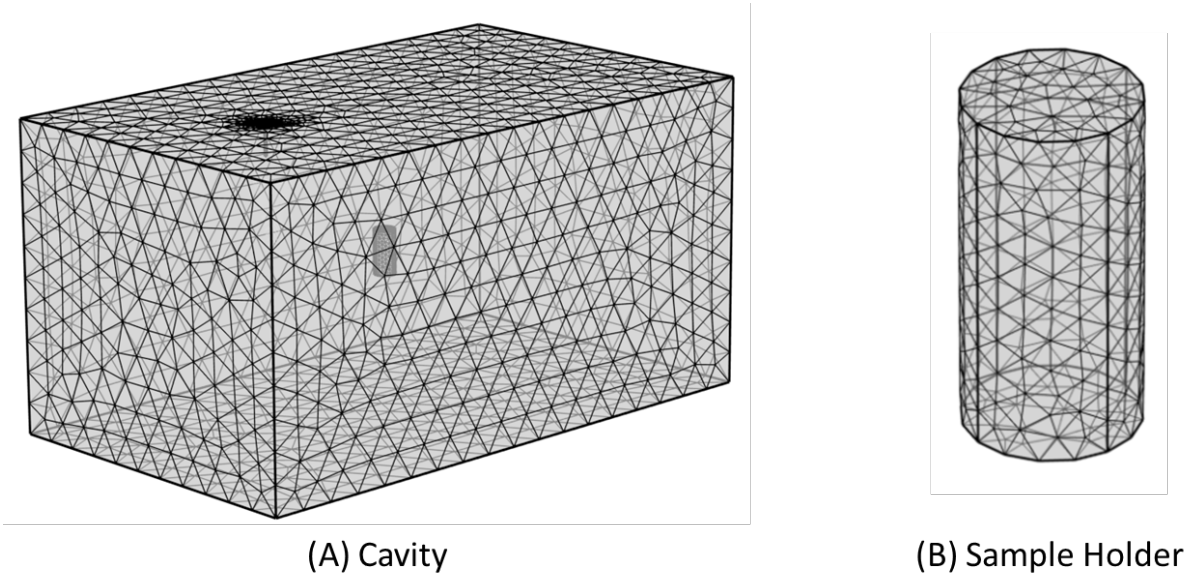

Figure 3-12. Meshed computation model of the resonant cavity

Table 3-2. The dimension and physical properties of the resonant cavity system

Parameters	Value	Unit
Length of the cavity	680	mm
Width of the cavity	400	mm
Height of the cavity	350	mm
Length of the probe antenna	40	mm
Radius of the probe antenna	1.5	mm
Coaxial transmission line impedance	50	Ω
Power input	400	W
Electrical conductivity of copper wall	5.9×10^7	Sm^{-1}
Relative permittivity of air	1	
Electrical conductivity of air	0	Sm^{-1}

3.3.5 *Experimental setup*

To validate the computational model, heating experiments of the electromagnetic rewarming were performed, and the heating results were compared with the simulation outputs. The electromagnetic signal was produced by a signal synthesizer (E4432B, Agilent Technologies, Santa Clara, CA) and then boosted by a power amplifier (5006FE, OPHIR RF, Los Angeles, CA). The amplified electromagnetic wave was transmitted to the resonant cavity through the coaxial transmission line. A 25 mL cryopreserved sample solution (10% DMSO + 0.25 M Trehalose) was

placed at the center of the cavity. A fiber optic temperature sensor was placed in the sample solution to monitor and record the temperature change. The rewarming test was performed from -80 ℃ to 0 ℃.

3.3.6 *Simulation results and discussion*

3.3.6.1 Validation of the numerical model

The computed resonant frequency of the cavity was 434.8 MHz, which was consistent with the theoretical calculation. Figure 3-13 shows the comparison of the electric field intensity between the analytical results and simulated results. At the resonant state, the electric field intensity of both analytic and simulated results was aligned. The magnitude of the electric field increased significantly as the position towards the center location. To utilize the most of the electromagnetic power and achieve the rapid rewarming, the cryopreserved sample should be placed at the center position inside of the resonant cavity.

Beyond the electric field intensity, modeling of the coupled electromagnetic-heat transfer process was also validated by the experimental result. Figure 3-14 shows the comparison of the temperature profile between the experimental result and the simulated result. The simulated warming process demonstrated a similar tendency to the experimental group. The average warming rate of the numerical model was calculated as $57.47\ ℃\ \mathrm{min}^{-1}$, while the heating experiment achieved at $54.95\ ℃\ \mathrm{min}^{-1}$. The consistent results further proved the reliability of the numerical model. The difference in the warming rate between the two approaches might be caused by the unsatisfactory fabrication of the resonant chamber. Limited by machining accuracy, the manufactured chamber may contain the curved surface on the sidewalls and lead to the potential electromagnetic power leakage at the connectors.

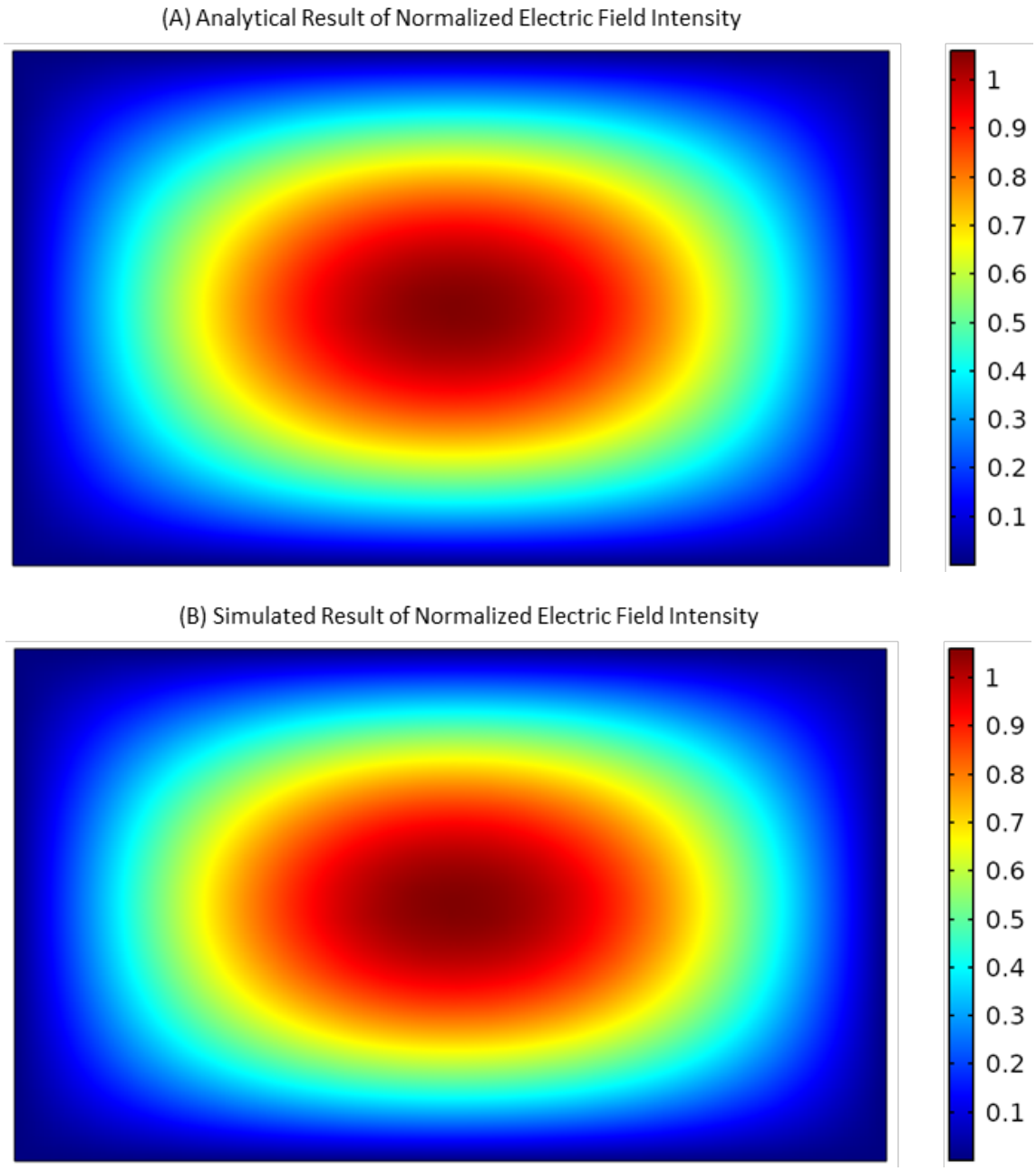

Figure 3-13. Comparison of the electric field distribution between analytical results and simulated results

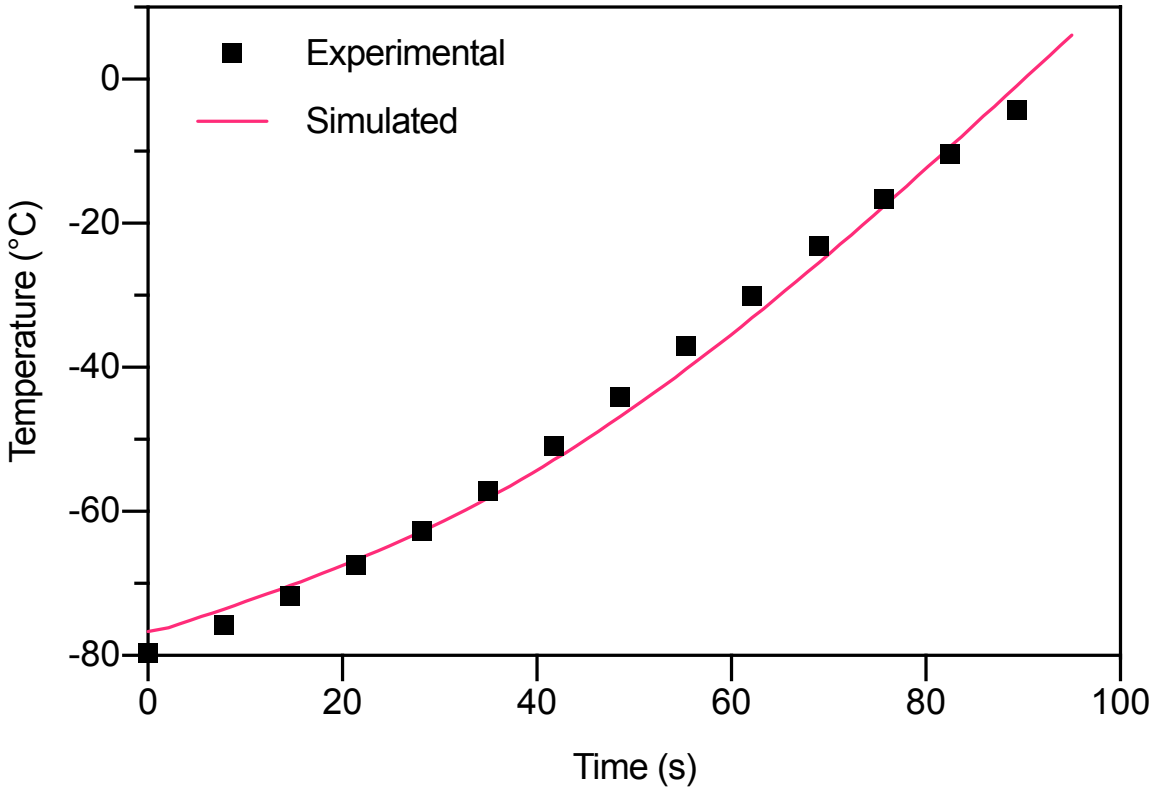

Figure 3-14. Comparison of the temperature profile in the heating process between the experimental result and the simulated result. The mean value at each temperature point of experimental result were determined based on three replicates (n=3).

3.3.6.2 Determination of the shape of the sample holder

In a single-mode resonant cavity, it is also critical to determine the shape of the sample to avoid uneven temperature distribution that leads to the thermal stress induced fracture of the cryopreserved biomaterials. Due to the complex interaction between electromagnetic and heat transfer and inaccurate real-time temperature monitoring, it is hard to investigate the effect of the sample shape analytically and experimentally. Thus, the rewarming rate and temperature distribution of different shapes of the sample holder were evaluated by the numerical simulation. The same computational configurations in the previous heating test were applied in this study.

Table 3-3 shows the dimensions of four different sample shapes. The volume of the samples was controlled at 25 mL. The rewarming process was simulated from -80 ℃ to 0 ℃.

Table 3-3. The dimensions of different shapes of the sample holder

Parameters	Value (mm)
Radius of spherical holder	18.14
Radius of cylindrical holder	13.3
Height of cylindrical holder	45
Axis-a of ellipsoidal holder	14
Axis-b of ellipsoidal holder	18
Axis-c of ellipsoidal holder	23.7
Edge length of cubic holder	29.25

Figure 3-15 shows the temperature profile of different sample shapes. From rapid to slow, the average rewarming rates of the cylindrical, ellipsoidal, spherical, and cubic samples were obtained to be $57.47, 54.36, 43.15,$ and 31.52 ℃min^{-1}, respectively. Cylindrical and ellipsoidal holders achieved higher warming rates and reached 0 ℃ within 100 seconds.

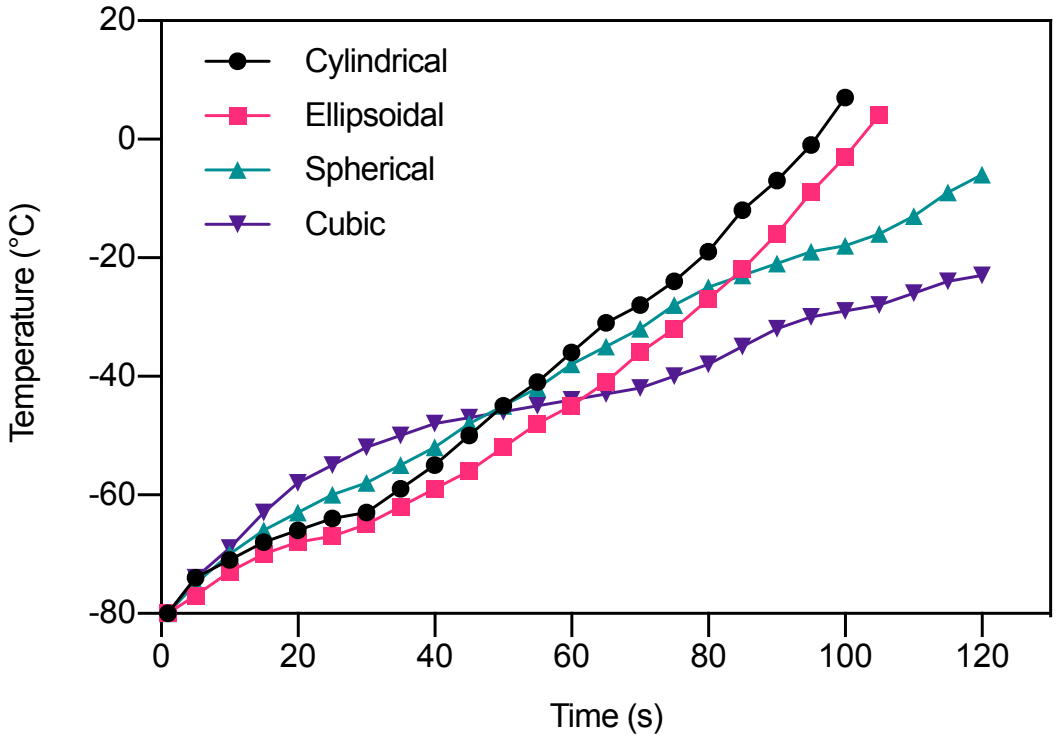

Figure 3-15. Simulated results of the temperature profile of different sample holder shapes

The post-thawed temperature distribution of different sample holder shapes was also analyzed and shown in Figure 3-16. The temperature gradient was calculated by the difference of the maximum and minimum temperatures of the holder divided by the distance. For cylindrical, ellipsoidal, spherical, and cubic holders, the temperature gradients were $0.97, 0.42, 1.03$, and $1.84\ °\mathrm{Cmm}^{-1}$, respectively. Cubic holder was neither quickly nor uniformly heated, which confirmed the previous research that samples with sharp surfaces and edges were not optimal choices to be warmed by the electromagnetic system [65, 88].

Ellipsoidal holder performed the best in the uniformity and realized a relative higher warming rate. Robinson proposed ellipsoidal holder was a better shape in the electromagnetic chamber; a cone-shaped sample holder was used to mimic the ellipsoidal shape in his work [65]. However, it is extremely hard to fabricate a precisely measured ellipsoidal holder with thin-layer

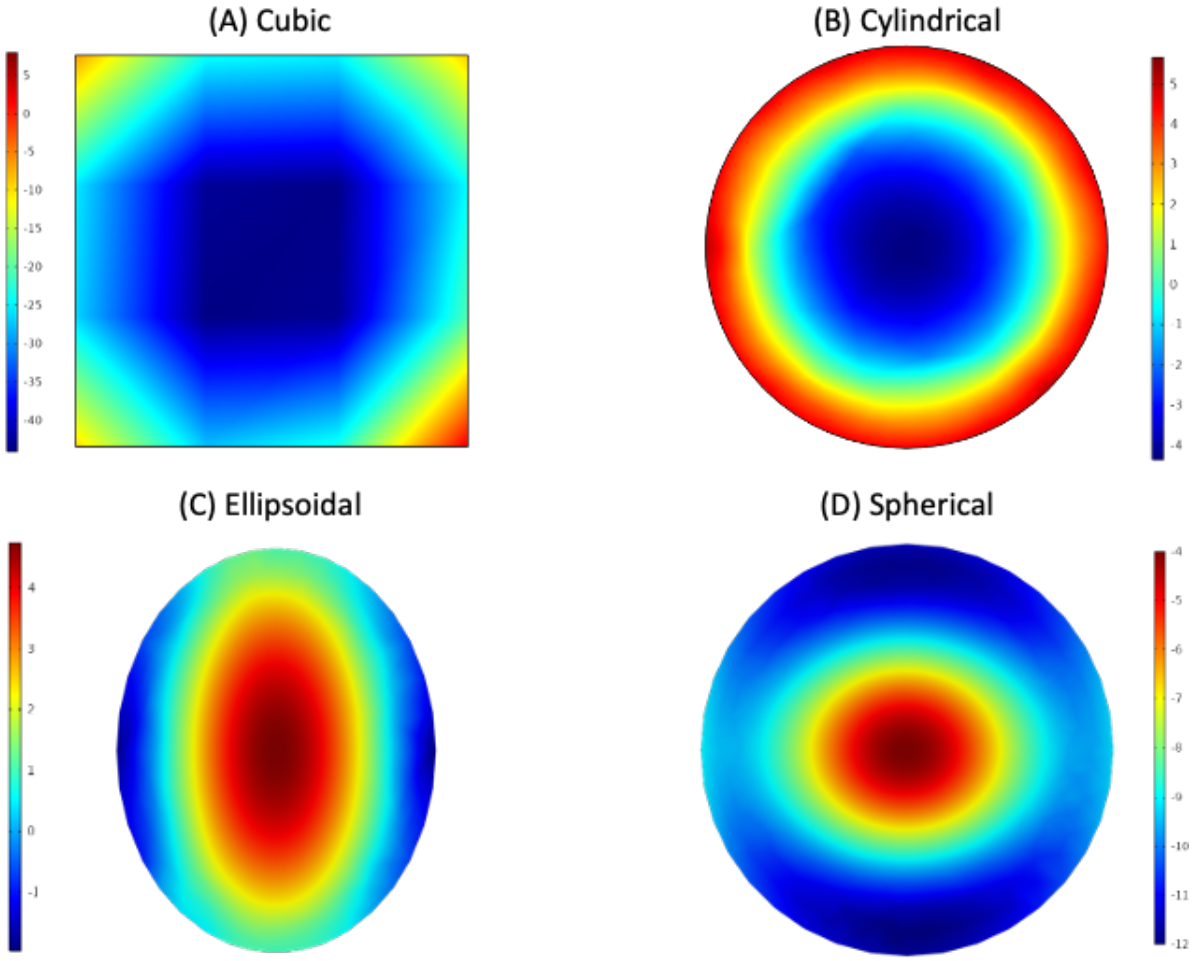

Figure 3-16. Simulation results of the post-thawed temperature distribution of the different sample holder shapes. (A) Cubic holder; (B) Cylindrical holder; (C) Ellipsoidal holder; and (D) Spherical holder

material to reduce electromagnetic absorption. Imperfect manufacture may compromise the overall warming performance. On the other hand, the cylindrical holder was the fastest holder shape with the second-best uniformity. The rapidity of the cylindrical sample heating indicated a promising application on the cryopreservation of large biological systems. In addition, it is fairly simple to manufacture a cylinder with customized dimensions, while there are multiple commercially

available cylindrical products on the market. Although the central temperature is still lower than the edge, a further improvement to dimmish the temperature difference is discussed in chapter 5.

3.4 SUMMARY

In this chapter, methods and systems to measure the essential electrical and thermal properties of CPA solution were developed and set up. The cavity perturbation technique was adopted in the measurement system. The optimal CPA solution for electromagnetic warming was determined. 10% DMSO with 0.25 M trehalose was selected due to its large absorbability to electromagnetic power. A numerical simulation model was presented and validated with the experimental data to assist the design and optimization of the resonant cavity system. Through the computation, the effects of the different sample holder shapes were studied. Combine the heating performance and easy fabrication, the cylindrical holder was decided the most suitable shape to carry the CPA solution.

Chapter 4. DEVELOPMENT OF THE REAL-TIME RESONANT FREQUENCY MONITORING & CONTROLLING AND AUTOMATIC SAMPLE LOADING SYSTEM

4.1 INTRODUCTION

A rapid and uniform rewarming method is imperative to the successful cryopreservation of large biomaterials. Volumetric heating technology by electromagnetic rewarming, is a promising approach. For both single mode and multimode resonant systems, it is challenging but critical to maintain the resonant state within the cavity during the entire warming process to hold the fast and homogenous thawing. Dielectric constant and dielectric loss are two temperature-dependent electrical properties. In the warming, the dielectric properties change as the temperature increases, which shift the resonant frequency of the biosample. If the feeding frequency of the electromagnetic power does not match the resonant frequency, the resonant state is not maintained. At an off-resonant state, the electromagnetic power absorbed by the samples will be dropped extensively. Moreover, the power that was not absorbed by the biomaterials will be reflected in the rewarming system and cause severe damage to the equipment and potential electromagnetic radiation hazards to the surrounding. Therefore, it is crucial to establish a sub-system to achieve real-time monitoring and controlling of the resonant frequency to keep the resonant state at all times.

Additionally, in the cryopreservation, the biosamples are generally stored at -80 ℃ to -196 ℃. In such a low-temperature environment, it is extremely dangerous for the operator to transfer and load the samples to a rewarming system by human hands. Though some cryogenic

protective equipment (goggles, gloves, clothing, etc.) may reduce the risk of low temperature, it is still inefficient and time-consuming to manually loading a large number of samples. Besides, the single mode resonant cavity requires the sample to be precisely placed at a specific position to obtain the best heating performance. The positioning error caused by the manually loading may compromise the warming effects and results in permanent damage to the biomaterials. Thus, an automatic sample loading system is needed to reduce the labor cost and improve position accuracy.

Combing these improvements of the warming system with vitrification, a cooling technique to suppress the formation of ice crystals during the freezing procedure, make the cryopreservation of large volume biomaterials possible. To prepare for the later tests with biological samples, vitrification solution was used in the development and assessment of sub-systems for electromagnetic warming. However, different compositions and concentrations of vitrification solutions have drastically different dielectric properties that affect warming outcomes. The same measurement systems and methods of the essential properties in chapter 3 were adopted to determine the optimal vitrification solution for the electromagnetic rewarming.

In this chapter, the effects of the vitrification solution to electromagnetic heating are discussed. Ideal vitrification solution is determined through the measurements of the dielectric properties. Further improvements are added to the picked solution to ensure the quality of the vitrification process. Thereafter, a resonant frequency adjusting system with dynamic feedback control and automatic sample loading system is designed and manufactured.

4.2 Effects of the vitrification solution on the electromagnetic heating

A much higher concentration of cryoprotectants, the chemical agents to protect the cells from cryoinjuries, are used to prepare vitrification solution. The solution develops an amorphous

glass state at the low temperature to completely prevent the formation of ice crystals during the cooling procedure. Meanwhile, the solute concentration inside the cells won't further increase during the vitrification due to the absence of the extracellular ice. As a result, a higher survival rate of the biomaterials is expected.

In order to prevent recrystallization or devitrification, rapid warming is still needed. The disappearance of ice crystals also benefits electromagnetic heating. At a frequency around 434 MHz, ice's absorbability of the electromagnetic power is significantly lower than the aqueous solution. In another way, the rewarming rate achieved by the vitrification solution should be higher than the lower concentration of CPAs.

There are two major factors of a solution to accomplish the glass state during the cooling, solute concentration and cooling rate. In general, the higher the concentration, the lower the required cooling rate. For a given solution, the critical cooling rate (CCR) is the lowest required freezing rate to succeed the vitrification. Similarly, the critical warming rate (CWR) is the lowest required heating rate to prevent devitrification. The CCR and CWR of several vitrification solutions are given in Table 1-1.

4.2.1 *Determination of the optimal vitrification solution*

Most of the previous cryobiologists focused the study of vitrification solutions on the solute injuries, toxicity, ions stability, and the tendency to achieve vitrification during the cooling process [99-103]. This study emphasizes the effects of the vitrification solution on the warming process. The ability of the vitrification solution to absorb electromagnetic energy depends on the dielectric properties. The same measurement system and methods introduced in chapter 3 were applied to determine the dielectric constant and dielectric loss of the vitrification solutions. The preselected

solutions were based on the work by Fahy and Brockbank that involve the design and toxicity research of several vitrification solutions [104, 105]. Table 4-1 shows the composition of DPVP, EPVP, and PPVP. Table 4-2 shows the composition of VS55 and VS83.

Table 4-1. Composition of vitrification solutions: A

Solution	Concentration (g/dL)			
	D	E	P	PVP
DPVP	41			6
EPVP		44		6
PPVP			36	6

D: dimethyl sulfoxide; E: ethylene glycol; P: propylene glycol; PVP: polyvinylpyrrolidone

Table 4-2. Composition of vitrification solutions: B

Composition	VS55	VS83
5X Euro Collins (mL)	200	200
HEPES buffer (g)	2.39	2.39
Propylene glycol (g)	168.38	252.57
Formamide (g)	139.56	209.34
Dimenthyl sulfoxide (g)	242.14	363.21
Water (mL)	to 1 L	to 1 L

The dielectric properties were obtained at every 5 ℃ between -120 ℃ to 0 ℃.

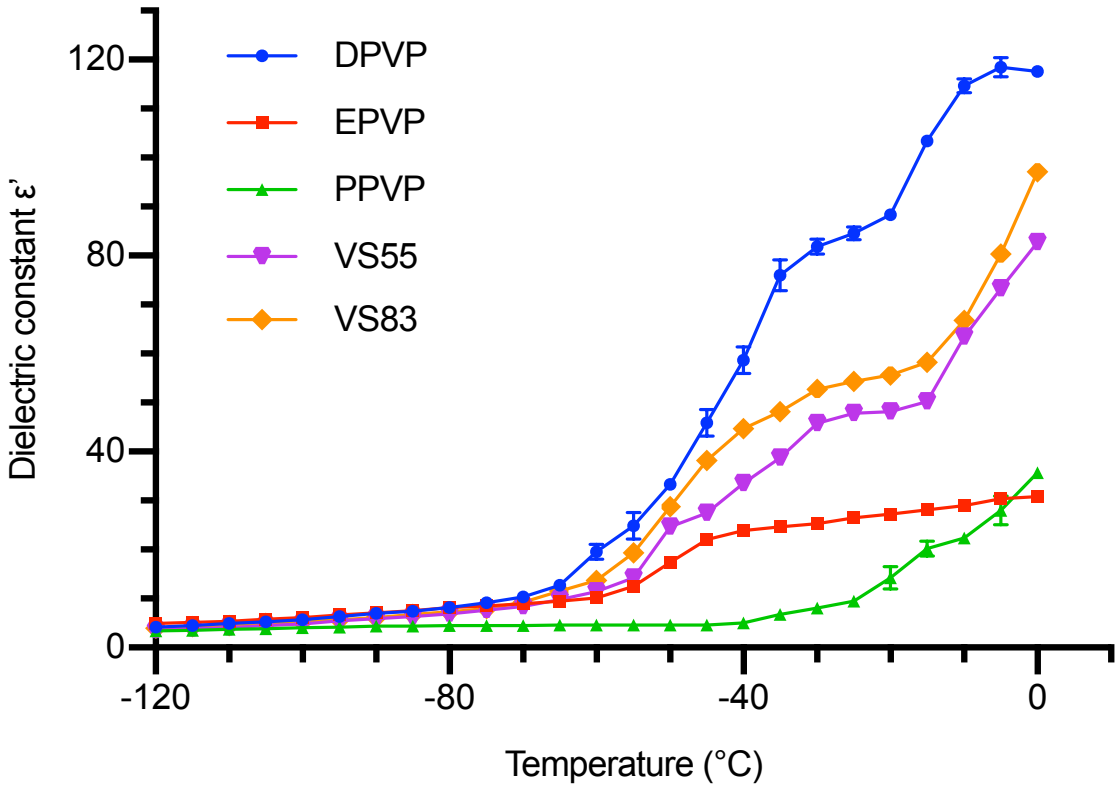

Figure 4-1. Dielectric constant, ε', versus the temperature for DPVP, EPVP, PVP, VS55, and VS83. The mean values $\pm$ standard deviations at each temperature point were determined based on four replicates (n=4).

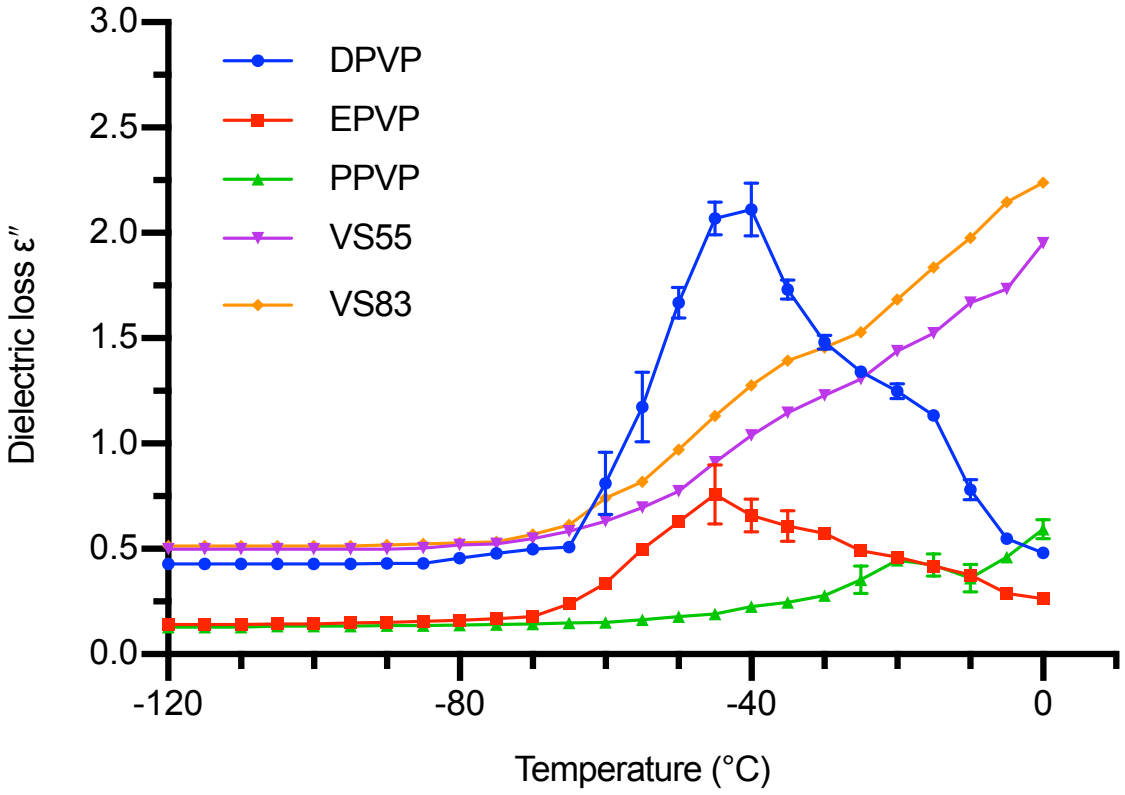

Figure 4-2. Dielectric loss, ε'', versus the temperature for DPVP, EPVP, PVP, VS55, and VS83. The mean values $\pm$ standard deviations at each temperature point were determined based on four replicates (n=4).

Figure 4-1 shows the dielectric constant of the tested vitrification solutions. For all of the solutions, the dielectric constant, ε', remained stable between -120 ℃ and -80 ℃, then the value increased as the temperature increased. DPVP solution has the largest peak value of the dielectric constant among all of the tested solutions.

Figure 4-2 shows the dielectric loss of the tested vitrification solutions. Similarly, the dielectric loss, ε'', remained stable or slightly changed for all of the solutions between -120 ℃ and -80 ℃. Though, DPVP, VS55, and VS83 solutions showed higher value, implying they may succeed faster warming at this temperature range. DPVP and EPVP solutions reached the peak value around -40 ℃, then the dielectric loss decreased as the temperature increased. PPVP, VS55, and VS83 showed the trend of increasing temperature leading to the increased ability to absorb the electromagnetic power. Referring to the thermal runaway phenomenon, the warmer region continued to receive more energy, reinforce the same area to become even warmer. While the colder area remains cold due to the lower absorbability of the electromagnetic power. Therefore, PPVP, VS55, and VS83 may enlarge the temperature gradient inside the solution.

The inverted 'U' shape of DPVP and EPVP solutions indicated the lower ability to transfer the electromagnetic energy to heat above -40 ℃. In that case, the warming rate of the high-temperature area would slow down, make the time window for the colder area to pick up the heat, and reduce the temperature difference within the solution. The diminished temperature gradient could save the biomaterials from thermal stress and mechanical fracture. Together with the largest value of dielectric constant and relative large dielectric loss between -120 ℃ to -40 ℃, DPVP solution was the most suitable vitrification solution in electromagnetic warming.

4.2.2 *Improvements of the selected vitrification solution*

Despite the higher concentration of the solute, another factor that affects the glassification is the cooling rate. To achieve a fast rate, liquid nitrogen was used as the cooling source. Vitrification also depends on the temperature uniformity during the freezing since the thermal stress induced by a large temperature gradient may break the structure under the glass state. To prevent large temperature difference in the conductive cooling, the sample solution should not directly contact the liquid nitrogen so that solution is cooling by vapor without stimulating the liquid nitrogen into the boiling state.

The experimental setup of the cooling process is shown in Figure 4-3. 25 mL of DPVP solution was loaded into the cylindrical sample holder. Then, the holder was placed in a 3D printed rack and transferred to the liquid nitrogen dewar. A nylon string was used to hold the rack at an appropriate height to ensure the solution was cooled by the vapor phase nitrogen.

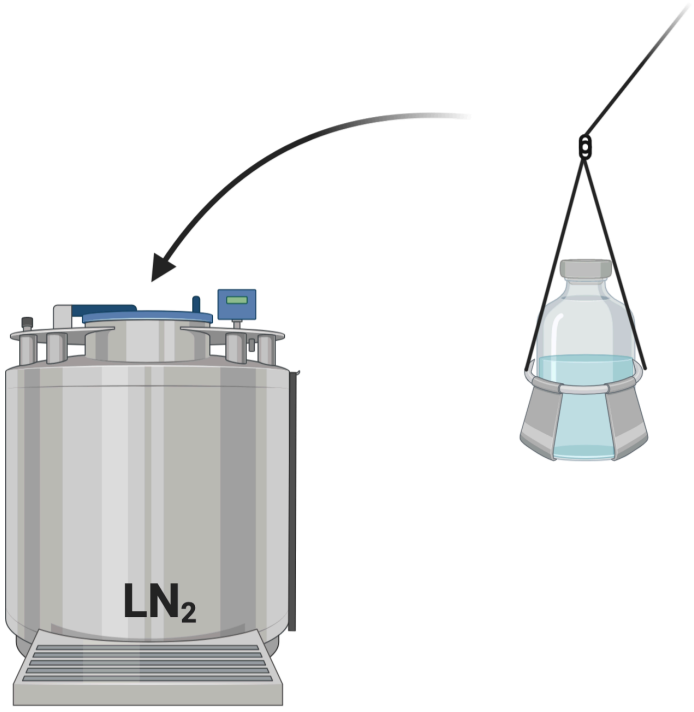

Figure 4-3. Schematic of the cooling of the vitrification solution

The temperature of the solution was monitored by the fiber optic sensor. Once the temperature reached to −140 ℃, the rack was pulled out from the dewar to check the state of the solution. As shown in Figure 4-4, three states of the solution have been observed.

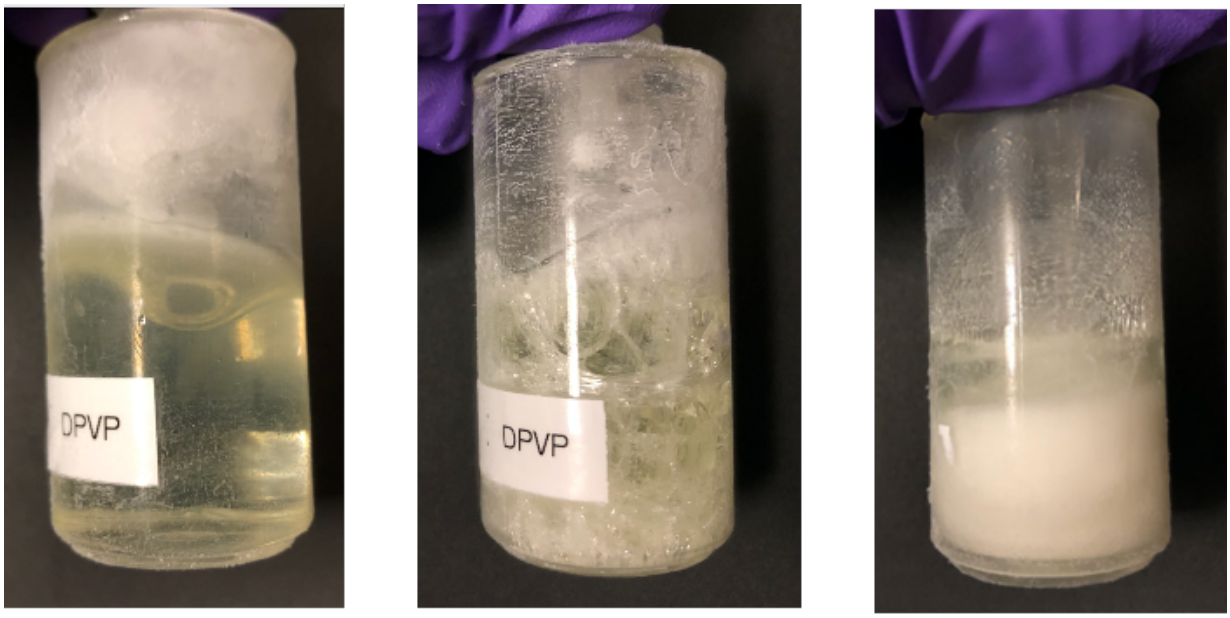

A. Vitrified B. Cracked C. Frozen

Figure 4-4. Represent pictures of DPVP solutions at −140 ℃

Figure 4-4 A shows the vitrified state of the DPVP solution. The transparent solid indicates the cooling rate achieved by the liquid nitrogen vapor was higher than the critical cooling rate and uniformed temperature distribution within the sample holder. Figure 4-4 B shows the cracked solution. While the surrounding transparent solid proved the successful vitrification was partially accomplished, the fractures were caused by the mechanical stress from the non-uniformed cooling. A lower position of the rack in the dewar may induce the crack since the exterior surface was too close to the liquid nitrogen and caused faster cooling. In general, it is required for small volume of biomaterial to be directly immersed into the liquid nitrogen to succeed the vitrification [100, 106]. However, the same method would not work for the large system due to the inhomogeneous temperature distribution by conductive cooling. Hence, it is vital to control the distance between

the sample and the liquid nitrogen level. Figure 4-4 C shows the frozen state of DPVP solution. The opaque solid represented the crystallization during the cooling that might because of the higher position of the rack. The successful vitrification is beneficial to the development of the resonant frequency control system and later test with biological systems. Therefore, further improvement of the selected DPVP solution is needed.

To ensure effective vitrification, a higher final concentration of CPA was considered. But, the continued addition of DMSO may cause severe osmotic damage to the cells. For that reason, glycerol was picked since the low P_s, permeability of the cell membrane to glycerol, to reduce the cell volume change during the CPA loading. Glycerol at different concentrations (2.5%, 5%, and 10% w/v) was added to the DPVP solution and then transferred to the dewar at the same position height to observe the solution state.

The cooling test for each solution was replicated at least 5 times. The results were shown in Table 4-3.

Table 4-3. Composition of vitrification solutions: C

Solution	Replicates	State		
		Vitrified	Cracked	Frozen
DPVP + 2.5% Glycerol	5	1	3	1
DPVP + 5% Glycerol	7	4	3	0
DPVP + 10% Glycerol	10	10	0	0

For the 10% glycerol group, a vitrified state was achieved at each trial out of ten replicates. Thus, the final composition and concentration of the vitrification solution were 41% DMSO, 10% glycerol, and 6% PVP.

4.3 REAL-TIME RESONANT FREQUENCY MONITORING & CONTROLLING SYSTEM

The single-mode electromagnetic resonant cavity was designed upon Maxwell's equations. The dimension, resonant frequency, and induced resonant state was calculated based on the cavity only. Figure 4-5 shows the comparison of the electric field intensity before and after the addition of DPVP solution. The results proved the insertion of an external object would change the distribution and intensity of the electromagnetic field. After that, the resonant frequency was changed accordingly. Moreover, the frequency and related resonant state were constantly changing during warming since the increasing temperature would affect the dielectric properties. As a consequence, it is imperative to develop a real-time resonant frequency monitoring and controlling system to maintain rapid and uniform warming.

There are multiple ways to track the shift of the temperature-dependent resonant frequency. The use of network analyzer and spectrum analyzer approaches are introduced and discussed in the following.

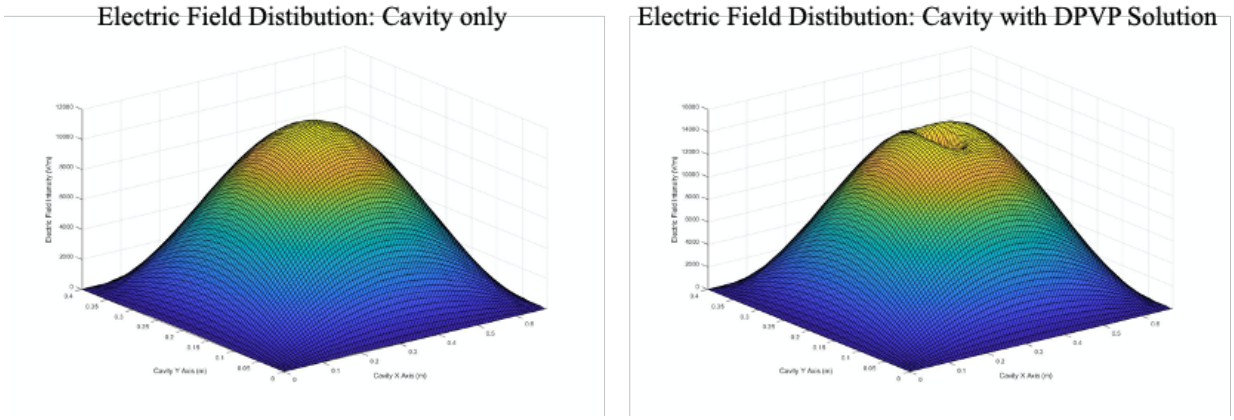

Figure 4-5. Comparison of the electric field distribution before and after the sample insertion

4.3.1 *Network analyzer approach*

Figure 4-6 shows the schematic of the system setup. The network analyzer was set up to measure the scattering parameters of the probe antenna in the cavity system. A small electric current was sent by the network analyzer to the antenna. Then, the reflection coefficient, S_{11}, describes the reflected power from the antenna was captured by the analyzer at different frequencies. The frequency that has the lowest return loss was determined as the resonant frequency. The fiber optic temperature sensor and temperature meter were used to record the change of the sample temperature. Overall, the real-time change of the return loss, resonant frequency, and temperature were recorded by a computer program developed in Python. Thereafter, an empirical equation that describes the relationship between resonant frequency and temperature of the sample solution was obtained. In the rewarming test, the program would actively adjust the input frequency of the electromagnetic power based on the feedback from the temperature meter to maintain the resonant state within the cavity.

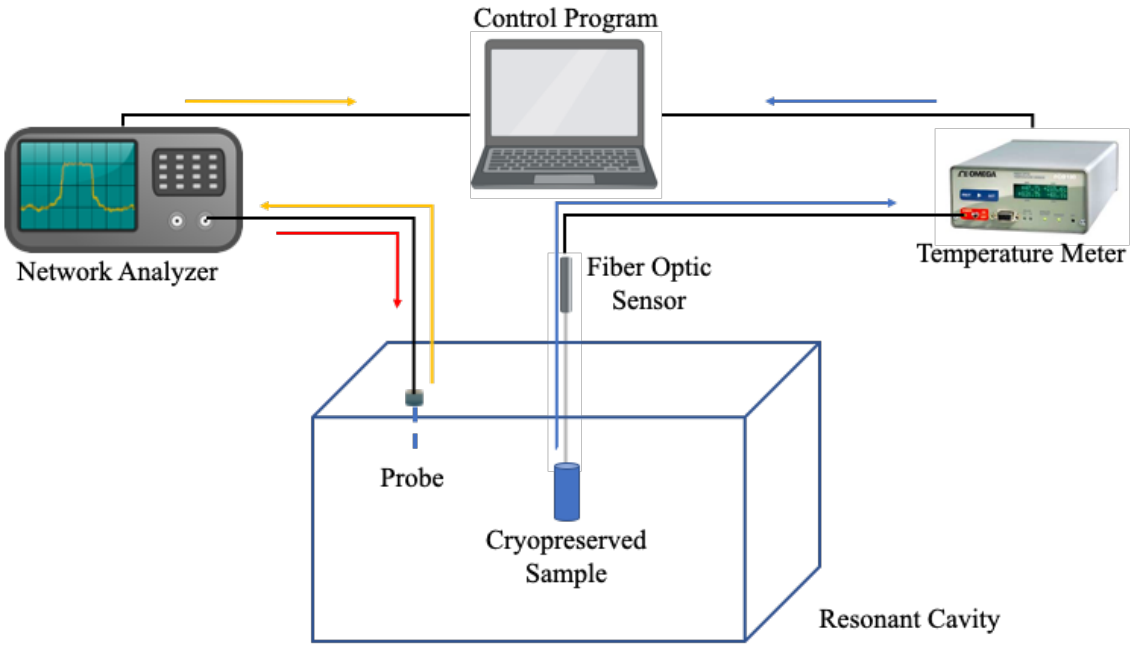

Figure 4-6. Schematic of the resonant frequency tracking system: network analyzer approach

4.3.2 *Spectrum analyzer approach*

Another method to check the resonant state was through the spectrum analyzer. Figure 4-7 shows the schematic of the system setup. Unlike the network analyzer, the spectrum analyzer could not send a radio frequency signal to the probe but only receive the reflected power from the cavity. Therefore, a signal generator was added to initiate the electromagnetic wave. By adjusting the input frequency of the electromagnetic source, the reflected power at different frequencies was obtained through the spectrum analyzer. The minimal return loss was attained at the resonant state. Combine with the readings from the temperature meter, the resonant frequency at various temperatures was determined.

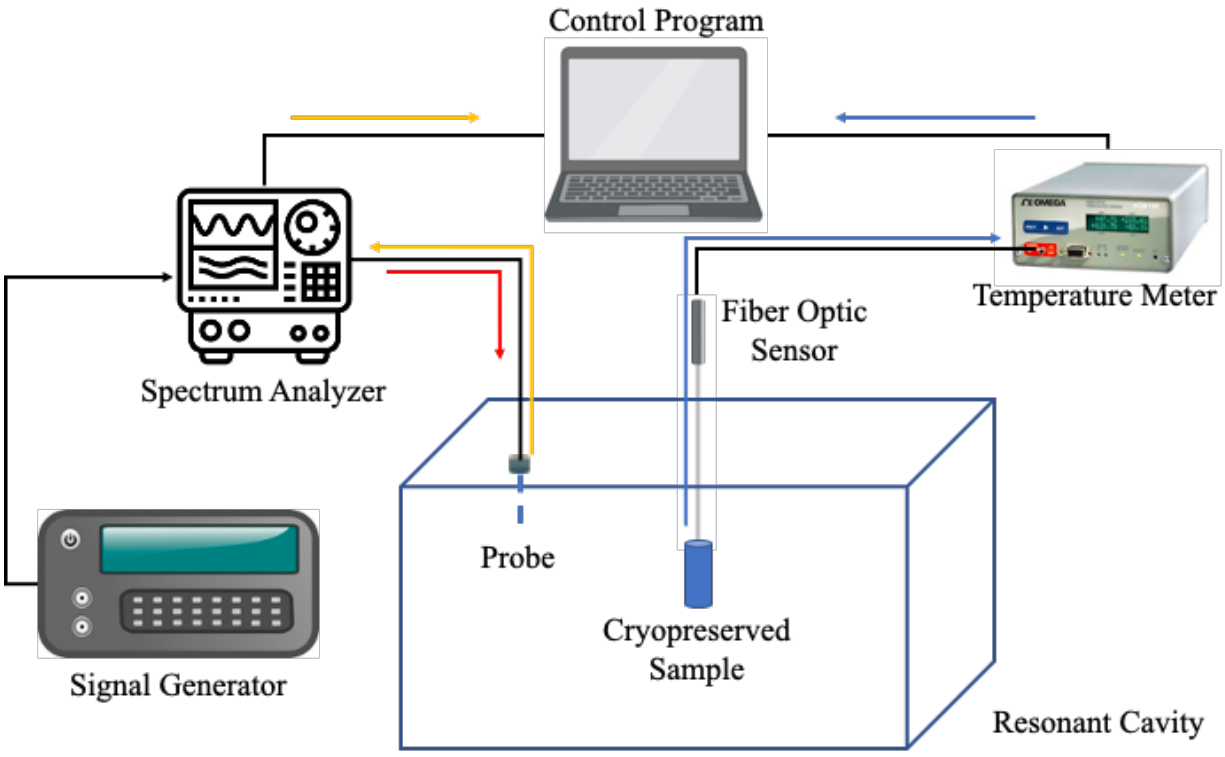

Figure 4-7. Schematic of the resonant frequency tracking system: spectrum analyzer approach

4.3.3 *Equipment and personnel protection system*

In the electromagnetic rewarming test, the amplified power could be as high as 500 W. If an off-resonant state happened, a considerable amount of the energy would be reflected from the cavity and causing serious damage to the system and surrounding environment. A protection system including directional coupler, circulator, and dummy loads was designed to ensure the safety of the heating equipment and operator.

Directional coupler (ZGBDC 20, Mini-Circuits, Brooklyn, NY) transmitted the amplified power to the cavity and directed the reflected power to the spectrum analyzer through the coupled port. Only a portion of reflected power, a thousandth in this study, was admitted through the coupled port to meet the spectrum analyzer's power input limitation. The rest amount of the reflected power was pointed to the circulator (SFC1402, Fairview Microwave Inc, Lewisville, TX), a three ports ferromagnetic component that was used to regulate the signal flow in a single direction. At last, the excessive power was absorbed by the dummy load (Model 264, MFJ Enterprises, Starkville, MS) served as a heat sink that converts the electromagnetic energy to heat.

4.3.4 *Automatic resonant frequency adjusting system with dynamic feedback control*

An overview of the automatic resonant frequency monitoring and the controlling system was illustrated in Figure 4-8. The entire system could be split into five subsystems.

The electromagnetic subsystem, as shown in the red dashed border, consisted of the signal generator and the power amplifier. The protection subsystem, in the dark blue dashed border, is composed of the circulator, directional coupler, and dummy loads. The cavity subsystem, in the orange dashed border, contains the resonant chamber, coaxial cable, and the probe antenna. In the green dashed border, the monitoring subsystem entails the spectrum analyzer, network analyzer,

and temperature meter. The control subsystem, in the black dashed border, includes the cable connectors and a PC with the embedded control program.

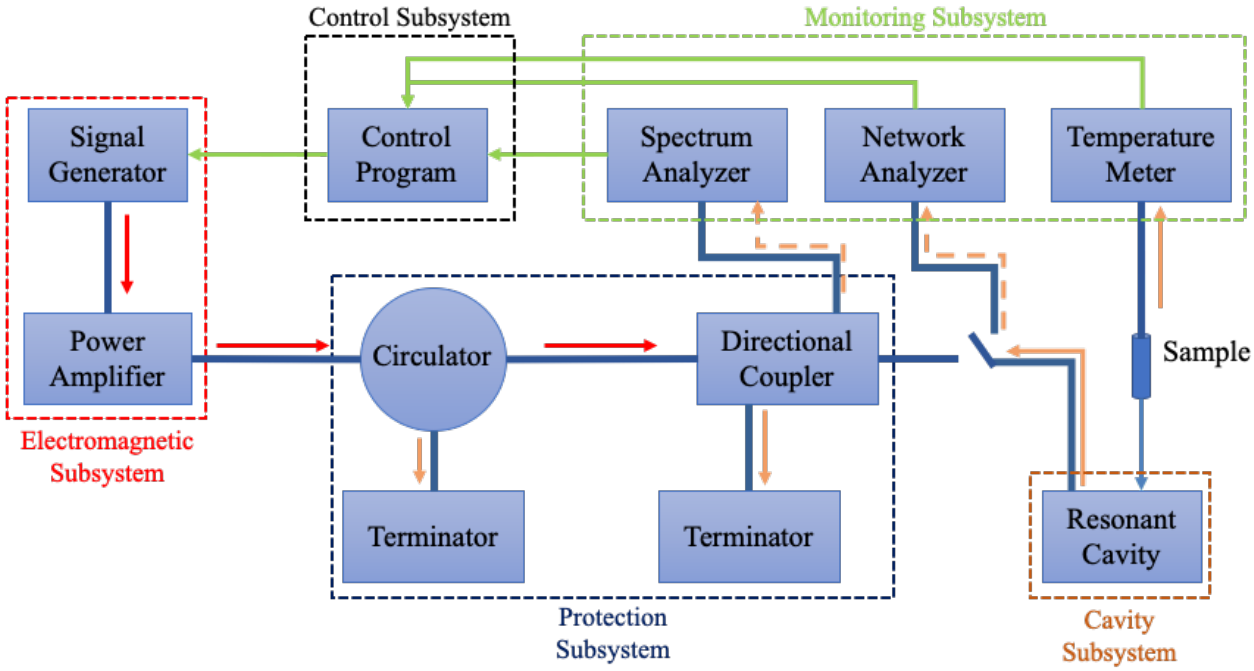

Figure 4-8. Overview of the automatic resonant frequency monitoring and controlling system

During the rewarming, electromagnetic waves were generated by the signal source. Followed the red arrow, the electromagnetic energy was amplified and transmitted to the resonant cavity to heat the cryopreserved samples. Depends on the resonant frequency system setup, the reflected power (shown in orange arrow) was directed to the network analyzer or spectrum analyzer. Based on the feedback from the monitoring system, the control program was updating the input frequency to the signal generator to maintain the resonant state within the cavity.

4.3.5 *Experimental setup*

25 mL of DPVPG solution (41% DMSO, 6% PVP, and 10% Glycerol) in a cylindrical holder was cooled by liquid nitrogen vapor to −150 ℃. Then, the sample holder was transferred to the cavity for the following tests.

In the test of the network analyzer approach, the solution was first rewarmed with natural air convection, while the change of resonant frequency, return loss, and the temperature were recorded. Based on the empirical relationship between resonant frequency and temperature, the warming test was repeated with manual and automated control to the input frequency of the electromagnetic power.

In the test of the spectrum analyzer approach, the solution was warmed by manually adjusting the input frequency based upon the feedback of the reflected power. The frequency, magnitude of the reflected power, and temperature were recorded. The control program automatically generated a fitted curve that represented the resonant frequency and temperature. Then, the rewarming test was performed again with the automated control to the input frequency.

DPVPG solution was also heated with a constant input frequency. In all of the rewarming tests, the amplified power was set at 400 W.

4.3.6 *Results and discussion*

Figure 4-9 shows the comparison of the temperature profile between manually and automated control to the input frequency in the network analyzer approach. The average warming rate achieved by manually and automated control was 93.59 and 114.84 ℃ min^{-1}, respectively. The control program improved the warming rate by 22.71%.

Figure 4-10 shows the comparison of the temperature profile between manually and automated control to the input frequency in the spectrum analyzer approach. The average warming rate achieved by manually and automated control was 105.21 and 155.74 ℃ min^{-1}, respectively. The control program improved the warming rate by 47.99%.

The mean values $\pm$ standard deviations at each temperature point were determined based on six replicates (n=6).

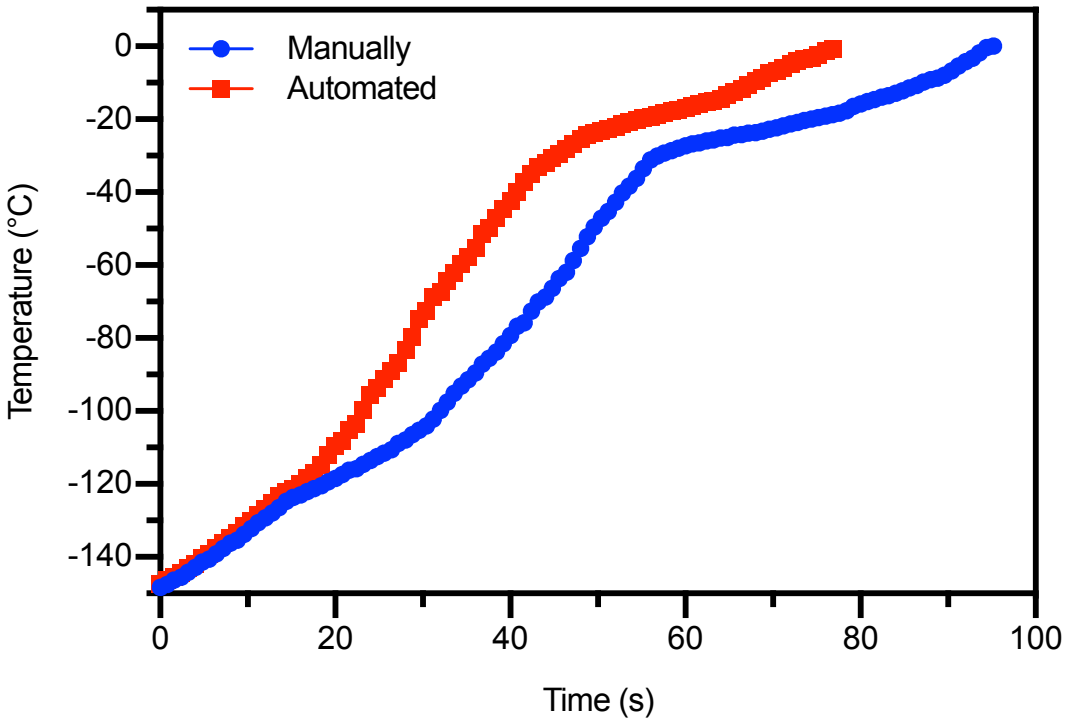

Figure 4-9. Temperature profile of the network analyzer approach: manually *vs.* automated

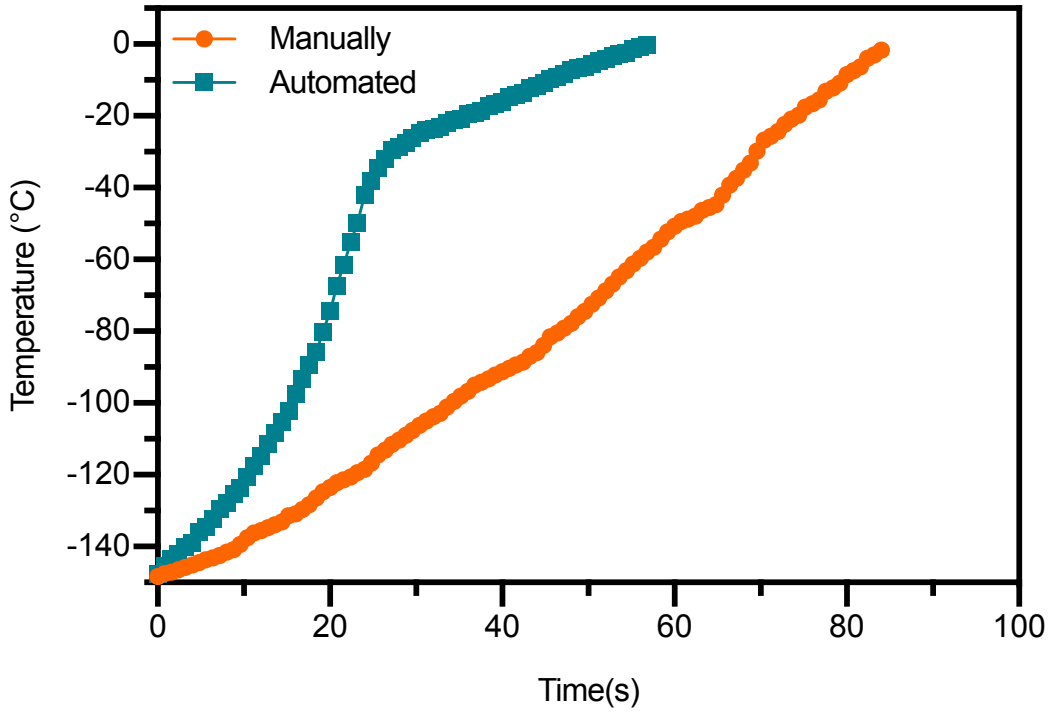

Figure 4-10. Temperature profile of the spectrum analyzer approach: manually *vs.* automated

Figure 4-11 adds the temperature profile of the rewarming process without any adjustment to the input frequency. The average warming rate was $47.38\ ℃\ \mathrm{min}^{-1}$.

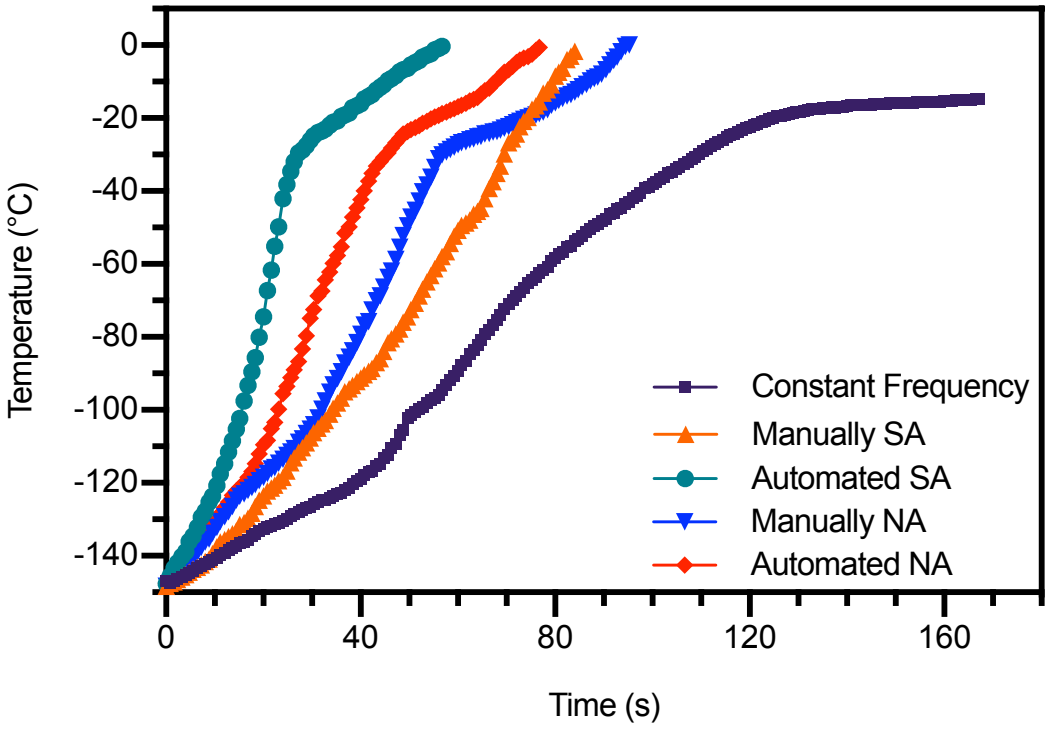

Figure 4-11. Temperature profile of DPVPG solution in the rewarming process: constant frequency, manually controlled frequency, and automated controlled frequency. SA: spectrum analyzer, NA: network analyzer.

The results indicated any frequency adjustment methods would improve the rewarming performance. The constant frequency method experienced the slowest rewarming rate, especially at the higher temperature range where the actual resonant frequency was shifted a lot from the initial input frequency. Around $-20\ ℃$, the rewarming curve was almost flat that implied devitrification might happen within the sample solution.

Between the two approaches to the monitoring and controlling of the resonant frequency, the spectrum analyzer method accomplished faster thawing. A potential reason caused the slower

warming of the network analyzer approach was the inaccurate temperature measurement during the determination of the empirical equation. Due to the position of the fiber optic sensor and the low thermal conductivity of the solution, the non-uniform temperature distribution may lead to the mismatch of the resonant frequency. The same issue would not affect the results from the spectrum analyzer method since the program was always looking for the frequency that has the highest absorbability to the electromagnetic power. Even though there was an error in the temperature measurement, the obtained frequency still suggested the lowest reflected energy.

4.4 AUTOMATIC SAMPLE LOADING SYSTEM

The vitrified sample was transferred from the liquid nitrogen dewar to the resonant chamber by human hand. At such low temperatures, the liquefied gases could cause frostbite or cryogenic burns to the operator if not handled properly. Moreover, the sample could be misplaced at the wrong position inside the cavity and compromised the heating performance due to the reduced electromagnetic field. To reduce the cold environment exposure and human error, an automatic sample loading system was designed and manufactured.

4.4.1 *Design of the sample loading system*

There were two major requirements for the sample loading system, fast-moving and precise positioning. The fast-moving could reduce the temperature change due to the natural convection during the loading process, and the precise positioning would guarantee the sample locates at the strongest electromagnetic field.

Figure 4-12 shows the 3D drawings of the automatic sample loading system. A linear actuator was used to deliver the sample to the center point inside the cavity. Since an external object would affect the electromagnetic field, the linear actuator should retract from the cavity

after the sample dropoff. The travel of the actuator was accomplished and controlled by the step motor. At the bottom of the actuator, a clamp was designed to pick up and drop off the sample holder. A separated aluminum frame supported the entire sample loading system to minimize the disturbance from the step motor's vibration to the cavity.

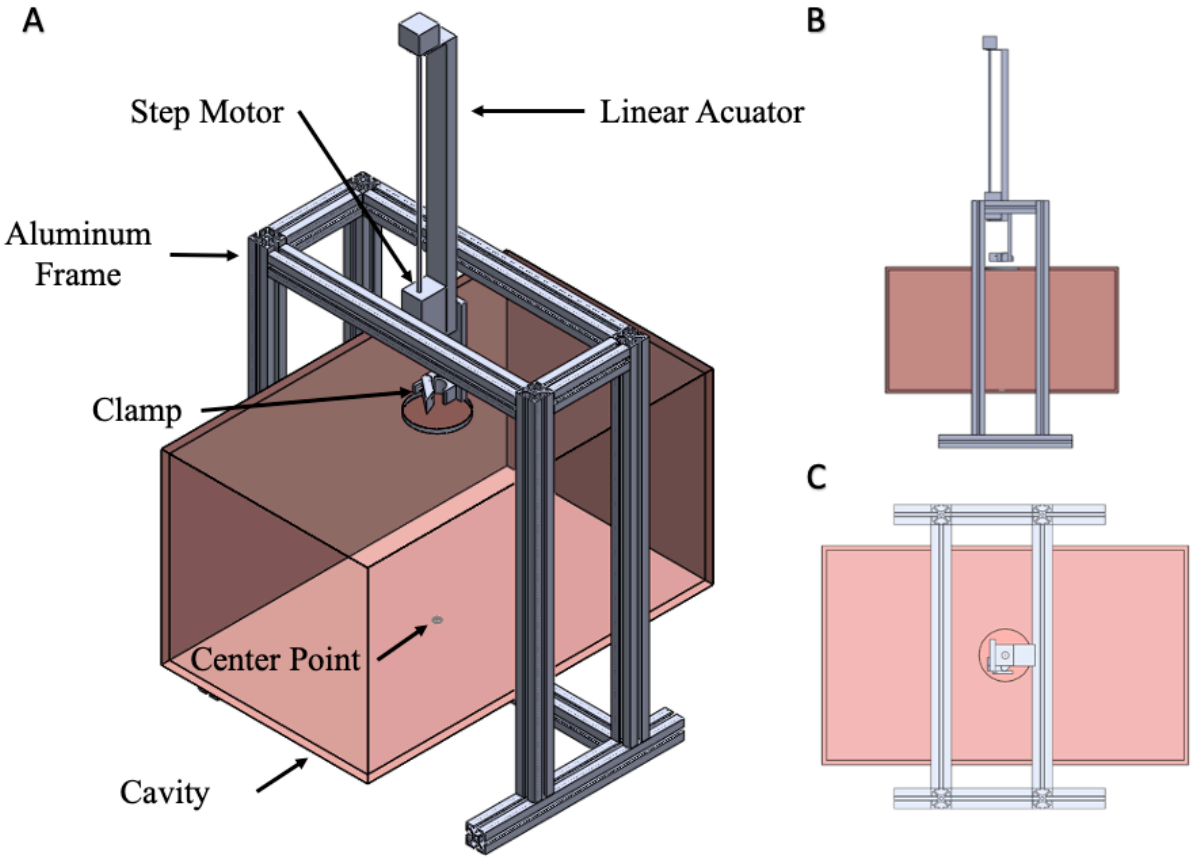

Figure 4-12. 3D drawings of the automatic sample loading system. A) components of the sample loading system. B) front view of the system. C) top view of the system.

Figure 4-13 shows the detailed design of the clamp. A concave surface was fabricated to work with the arm to brace the cylindrical sample holder. The arm was connected to a DC motor by a string. Through the DC motor control, the string was fastened or released to achieve the pick-up and drop off of the holder. To avoid the fracture at low temperature, the string was made of nylon, polyethylene, and Dacron fabric and tested the durability in the liquid nitrogen dewar.

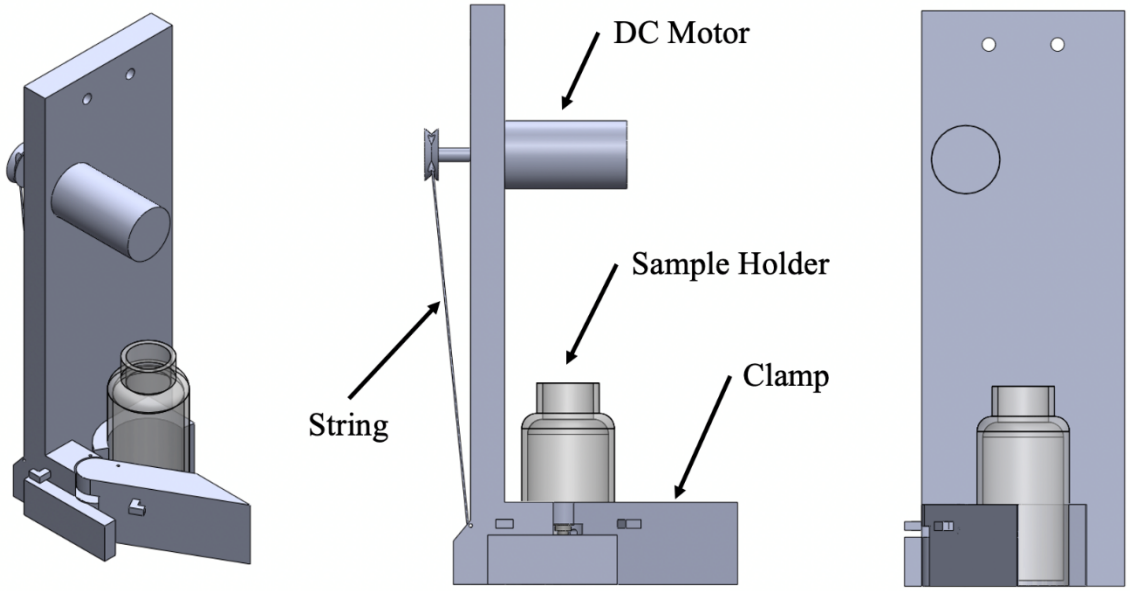

Figure 4-13. 3D drawings of the clamp. Left, the overview of the clamp; Middle, side view of the clamp; Right, front view of the clamp.

A control program was developed in Python (Python 3.0) to manage the delay between each step of the step motor and limit the DC motor's voltage.

4.4.2 *Experimental setup*

As shown in Figure 4-14, 25 mL of vitrified DPVPG solution at -150 ℃ was transferred to the clamp. Then, the control program initiated the sample loading protocol. The linear actuator moved down to the designated position, and the clamp released the sample holder. Finally, the actuator returned to the start position, and the system was ready for the rewarming procedure. The fiber optic sensor was placed within the sample to monitor the temperature change during the sample loading.

In Figure 4-15, the left figure shows the overview photograph of the automatic sample loading system. The middle and right displayed the initial and final states of the clamp.

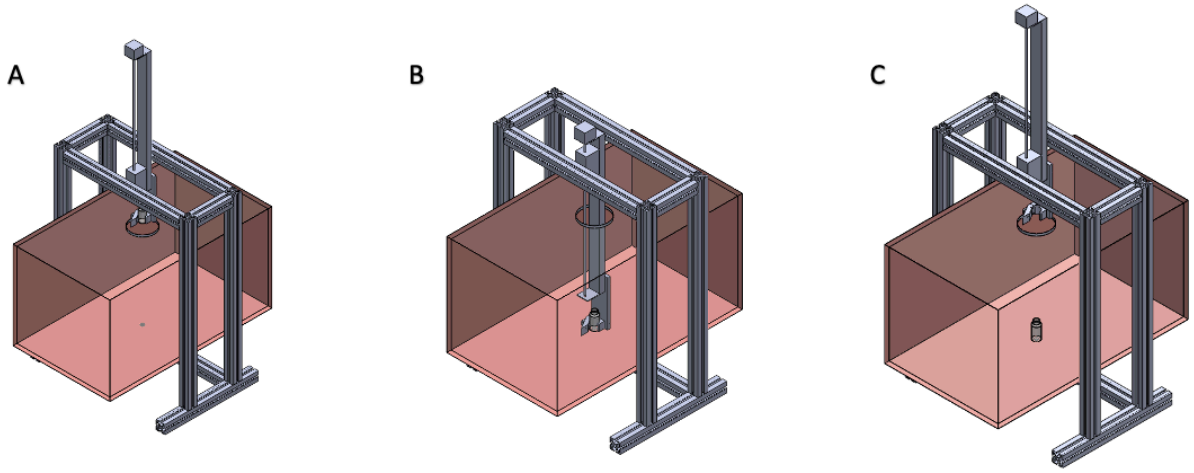

Figure 4-14. Schematic of the sample loading process. A) initial state, sample picked up by the clamp; B) middle state, sample released; C) final state, linear actuator retracted.

Figure 4-15. Photograph of the automatic sample loading system. Left, the overview of the system setup; Middle, the initial state of the system; Right, the final state of the system.

4.4.3 *Results and discussion*

The average time of the sample loading process was 37 seconds, and the sample holder was accurately placed at the designated center point inside the cavity. Figure 4-16 plotted the temperature profile of the sample solution during the loading process. The average change of the temperature of center and edge positions were 3.4 ℃ and 5.6 ℃. Due to the relatively short time, no significant temperature change was observed. The mean values ± standard deviations at each time point were determined based on four replicates (n=4).

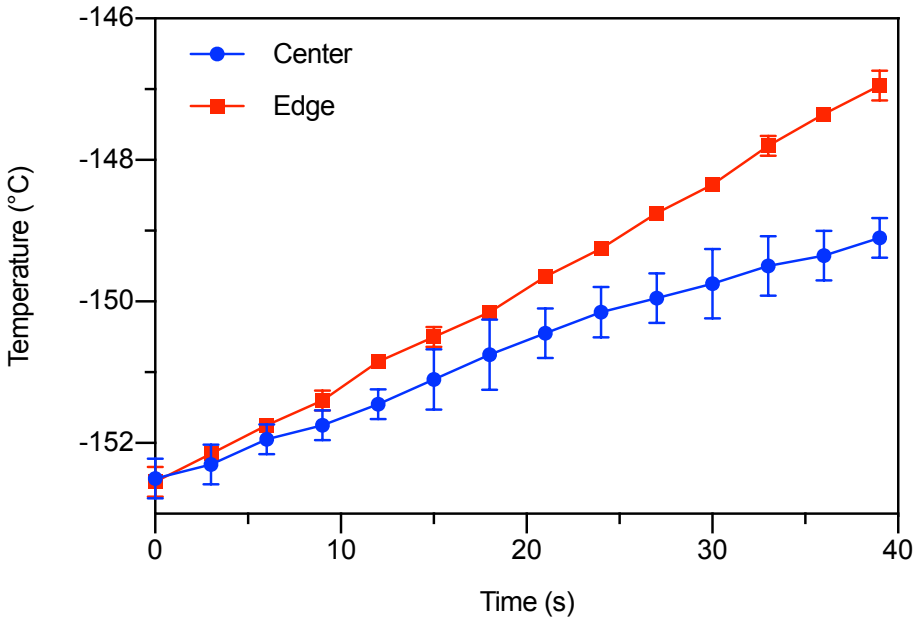

Figure 4-16. Temperature profile of DPVPG solution during the sample loading process

The majority of the time, 28 seconds, spent on the travel of the linear actuator. It is possible to lower the stepwise holding of the step motor to further reduce the total sample loading time. However, the increased moving pace would intensify the vibration of the actuator and lead to an unstable status of the sample holder.

A mounting bracket kit was designed and fabricated with 3D printing materials. As shown in Figure 4-17, the triangular bracket could enhance the support between the aluminum frame and

step motor to reduce the vibration on the linear actuator. The updated system allows the faster moving of the sample holder to meet the testing requirements of specific biomaterials that are highly sensitive to the temperature change within a short period of time.

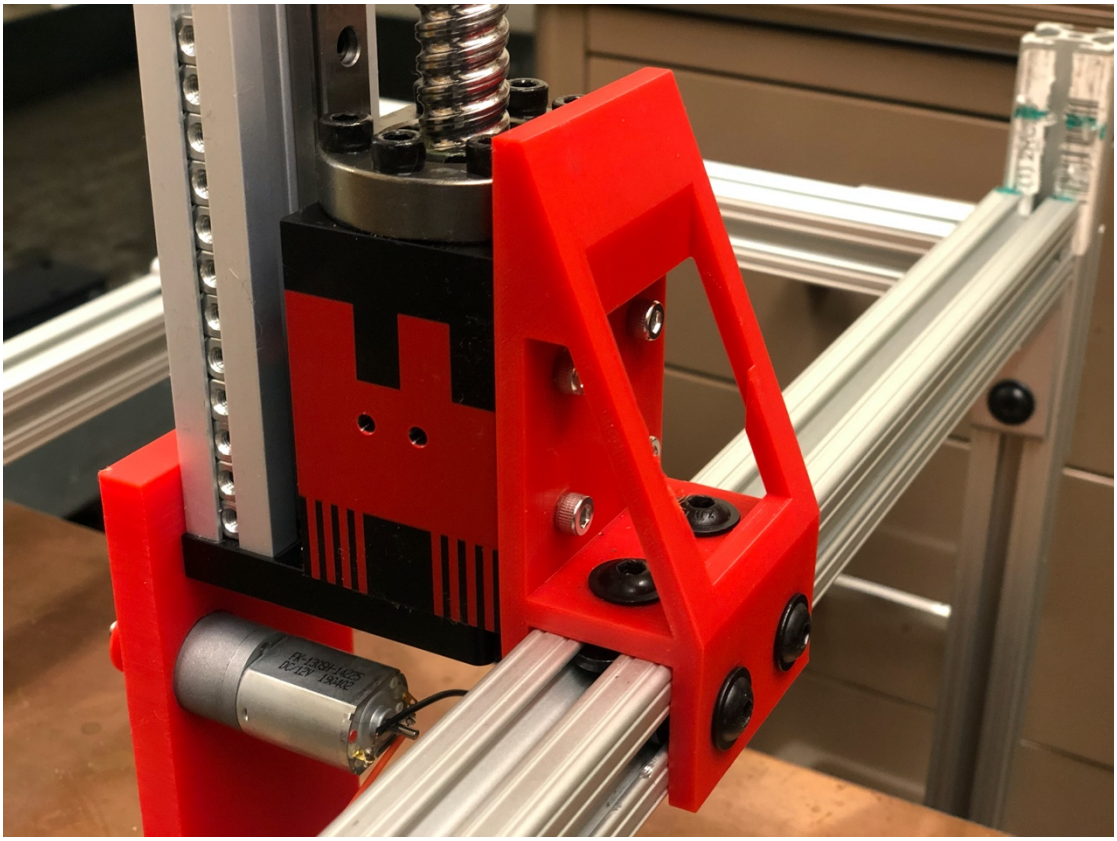

Figure 4-17. Triangular mounting bracket to enhance the supporting of the step motor

4.5 SUMMARY

In chapter 4, an optimal vitrification solution, DPVP, for the electromagnetic rewarming system was determined by measuring the dielectric properties. A further improvement to the composition and concentration of the selected solution was performed to ensure the vitrified state at the low temperature.

Rapid and uniform warming relied on the resonant state inside the cavity. A resonant frequency monitoring and the controlling system was established to achieve the real-time

adjustments to the input frequency of the signal generator. Compared to the warming process without any frequency adjustments, the program-controlled system significantly improved the rewarming rate. An automatic sample loading system was also developed to reduce the labor work and operating error during the loading process. Meanwhile, the system could protect the operator from potential cryogenic injuries.

Chapter 5. IMPROVED CRYOPRESERVATION OF LARGE VOLUME JURKAT CELL SUSPENSION WITH MAGNETIC NANOPARTICLES

5.1 INTRODUCTION

The previous chapters discussed the design and development of the electromagnetic resonant rewarming system. The power utilization was focused on the electric field. To make the most of the energy usage in the electromagnetic field and further enhance the warming rate and uniformity, the coupled magnetic field should also be employed. Due to most of the biological systems are nonmagnetic samples, a biocompatible material with high sensitivity to the magnetic field is needed.

In the past decades, magnetic nanoparticles (MNPs) have been widely used in various clinical diagnostics and therapeutic practices, including non-invasive magnetic resonance imaging (MRI), drug delivery, magnetic immunoassay, genetic engineering, and hyperthermia treatments [107-114]. A lot of heat could be released from the MNPs due to the heating effects under a strong oscillating magnetic field. In MNPs-based hyperthermia therapy, a regional temperature spike could wipe out the tumor at the designated area while maintaining the functionalities of the surrounding healthy cells and tissues. The application suggests that, with an effective control system, the heating advantage of MNPs would benefit electromagnetic warming in the cryopreservation of large biomaterials.

In 2014, a group in Minnesota reported the development of a radiofrequency electromagnetic coil rewarming system combined with the usage of MNPs [26]. Later in 2017, the same group succeed the cryopreservation of porcine carotid artery and porcine aortic heart valve

leaflet tissues with the 'nanowarming' technology [115]. However, the impressive warming results relied on the high concentration of the iron oxide MNPs at $10\ \mathrm{mg\,Fe\,mL^{-1}}$. There had been concerns about the cytotoxicity and other side effects of MNPs in specific types of cells [116-118]. Besides, the high cost also limited the sustainable development of the high dosage MNPs strategy.

In this chapter, MNPs at much lower concentration ($0.1\ \mathrm{mg\,Fe\,mL^{-1}}$) were added to the automatic electromagnetic resonant rewarming system. The enhanced system utilized the energy of both electric and magnetic fields to accomplish the rapid and uniform rewarming of bulky cryopreserved biosamples. 25 mL of Jurkat cell suspensions were cooled to -80 ℃ and stored at least 24 hours, then rewarmed with different thawing methods. The recovery rate and post-thaw biological functionalities of cells were evaluated.

5.2 MATERIALS AND METHODS

5.2.1 *Sample preparation*

Jurkat cell was chosen as the biological sample in this study. The cell culture process was the same as introduced in Chapter 2. The Jurkat cells were cultured to the live cell concentration around $1 \times 10^6\ \mathrm{mL^{-1}}$, then aliquoted to 12.5 mL in each cylindrical glass vials on ice. The viability and live-cell concentration were determined by the Trypan Blue solution.

5.2.2 *Magnetic nanoparticles*

10 nm iron oxide (Fe_3O_4) superparamagnetic nanoparticles with amine group dissolved in 10 mM PBS (Ocean NanoTech LLC, San Diego, CA) were used in this study due to their excellent utilization of the magnetic power and good biocompatibility. The MNPs were coated with monolayer amphiphilic polymer and monolayer of polyethylene glycol (PEG) to avoid cluster in

the solution. The MNPs embedded CPA solutions were stored at room temperature for 24 hours to observe the gathering of the nanoparticles. The distribution of MNPs in the CPA cocktail was also examined with transmission electron microscopy (TEM). 200 mesh carbon coated grids, or 300 mesh lacey carbon grids (Electron Microscopy Sciences, Hatfield, PA) were cast to the solutions, and then the imaging was captured by a Gatan Ultrascan CCD and Digital Micrograph software (Gatan, Pleasanton, CA) at The Molecular Analysis Facility, University of Washington.

5.2.3 *CPA solution*

10% (v/v) dimethyl sulfoxide (DMSO) and 0.25 M trehalose in PBS solution was used as the CPA cocktail. The electrical and thermal properties of the solution were determined in Chapter 3. The stock solution (20% (v/v) DMSO and 0.5 M trehalose) were added to the cell suspension slowly with a dropwise method on the ice until the final volume reached 25 mL.

For groups with nanoparticles, MNPs were premixed in the CPA cocktail to prepare the stock solution containing 20% (v/v) DMSO, 0.5 M trehalose, and MNPs at $0.2\ \mathrm{mg\ Fe\ mL^{-1}}$.

Stock solutions were prepared the same day as the CPA addition.

5.2.4 *Cooling device and process*

The CPA and MNPs loaded solution were transferred to a styrofoam box and placed in the $-80\ ℃$ freezer for 24 hours. The average cooling rate was measured as $1\ ℃\ \mathrm{min^{-1}}$ as the experimental results from Chapter 2 indicated the highest survival rate of Jurkat cells at this cooling rate.

5.2.5 *Rewarming methods*

Three warming methods were implemented, convective water bath, electromagnetic resonance warming, and MNPs enhanced electromagnetic warming.

For the convective option, the sample holder at -80 ℃ was fully immersed into the 37 ℃ water bath. The holder was shaking at 60 RPM in an orbital motion until the thermal couple reading reached 0 ℃, and no obvious ice crystal remained.

For volumetric warming methods, the cryopreserved sample was placed at the center point within the resonant cavity and heated with 400 W electromagnetic power. The signal generator and power amplifier were shut down by the control program once the fiber optic sensor reached 0 ℃.

5.2.6 *Temperature monitoring*

In the water bath warming, two thermal couples were inserted into the cell suspension (one at the center of the holder, the other one at the edge) to record the temperature profile and temperature gradient within the sample.

In the electromagnetic thawing, two fiber optic temperature sensors (center and edge) were used to avoid interference to the established electromagnetic field distribution.

For all three warming methods, the thermography picture of sample holders' exterior surface was captured by a thermal infrared camera (FLIR Systems, Wilsonville, OR) at the end of the heating.

5.2.7 *The recovery rate of the Jurkat cells*

Cell membrane integrity was determined by Trypan Blue assay to calculate the recovery rate of the Jurkat cell. 10 μL post-thawed cell suspension was mixed with 10 μL staining solution and then added to the counting slide. The cell counter was used to obtain the number of live cells and dead cells. The recovery rate of the Jurkat cells was determined with eq. (2.1).

5.2.8 *Assessment of the post-thaw biological functionalities*

The metabolic activity of the post-thawed Jurkat cell was determined by alamarBlue assay. As illustrated in Figure 5.1, 90 μL post-thawed cell suspension of each warming method was added to the 96-well plate. The same amount of fresh cells and growth media were also added as the positive and negative control group. Then, 10 μL alamarBlue assay was added to each well. The loaded plate was incubated at 37 ℃ for 2 hours. The absorbance of each well was determined by the microplate reader at 570 nm and 600 nm. The average absorbance readings of each group were normalized to the fresh control group and presented in the percentage.

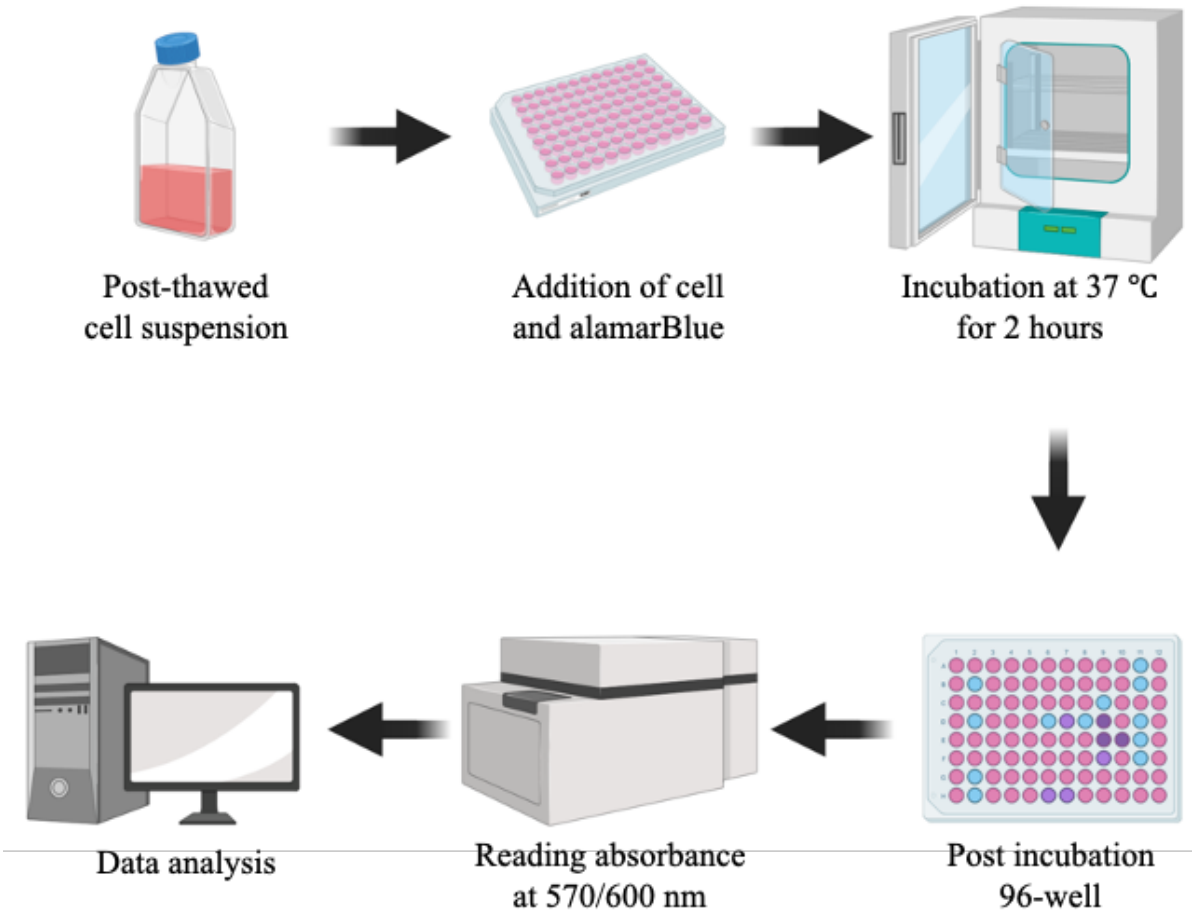

Figure 5-1. Determination of the metabolic activity of the post-thawed Jurkat cells

5.3 RESULTS AND DISCUSSION

5.3.1 *MNPs embedded CPA cocktail*

10 nm iron oxide nanoparticles were mixed with CPA cocktail to utilize the power of the magnetic field and enhance the warming results. Due to the interfacial chemical reactions and particle transport mechanisms, MNPs are naturally formed together and tend to the growth of clusters in aqueous dispersions [119, 120]. However, a cluster of MNPs would lead to the nonuniformed temperature distribution and localized overheating to the cells, which is against the intention of adding MNPs. A monolayer of PEG was coated on the surface of the MNPs to prevent

the aggregation of iron oxide. Figure 5-2 shows the stability of MNPs with and without PEG coating at room temperature over time.

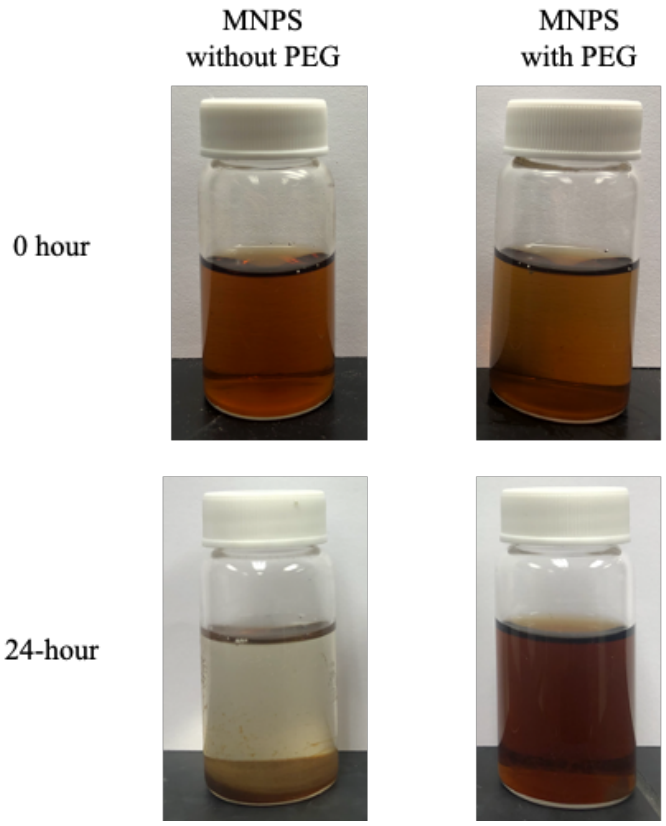

Figure 5-2. Stability of MNPs with and without PEG coating at room temperature over time

At time 0 hour, MNPs at 0.2 mg Fe mL^{-1} were mixed well with CPA solutions. No significant difference was observed between the two groups. At the time 24-hour, the MNPs with PEG coating remained in solution, whereas uncoated MNPs were fall out and separated at the bottom of the glass vial. Figure 5-3 shows the representative TEM image of MNPs in CPA solution and indicates the coated MNPs were uniformly distributed in the solution. Thus, the MNPs with PEG coating was used in this study.

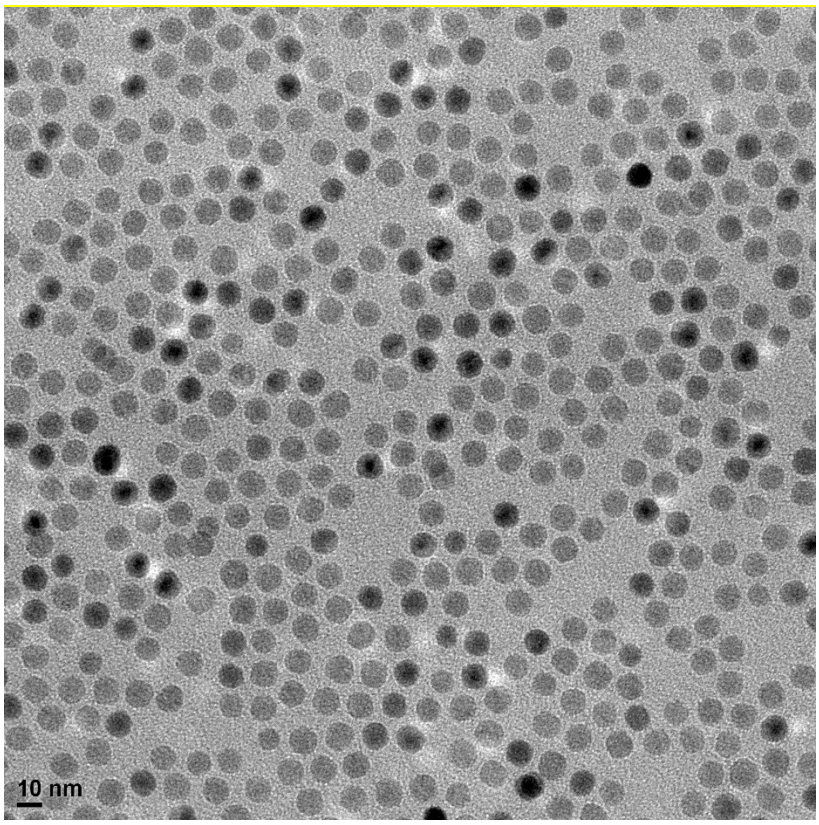

Figure 5-3. Representative TEM image of MNPs in the CPA solution

5.3.2 *Temperature profile and rewarming rates of different warming methods*

Jurkat cells were cryopreserved at -80 ℃ freezer for 24 hours and then transferred to a water bath or electromagnetic resonance warming system. A styrofoam box was used to carry the samples during transportation to reduce natural air convection effects. Figure 5-4 shows the temperature profile of different warming methods during the rewarming process. The average warming rate of the water bath, electromagnetic warming, and MNPs enhanced electromagnetic warming were achieved at 26.7, 91.3, and 152.4 ℃ min^{-1}. The addition of MNPs improved the average rewarming rate of electromagnetic resonance warming by 66.92% and was more than 5 times faster than the convective water bath. The mean values $\pm$ standard deviations at each time point of all cases were determined based on six replicates (n=6).

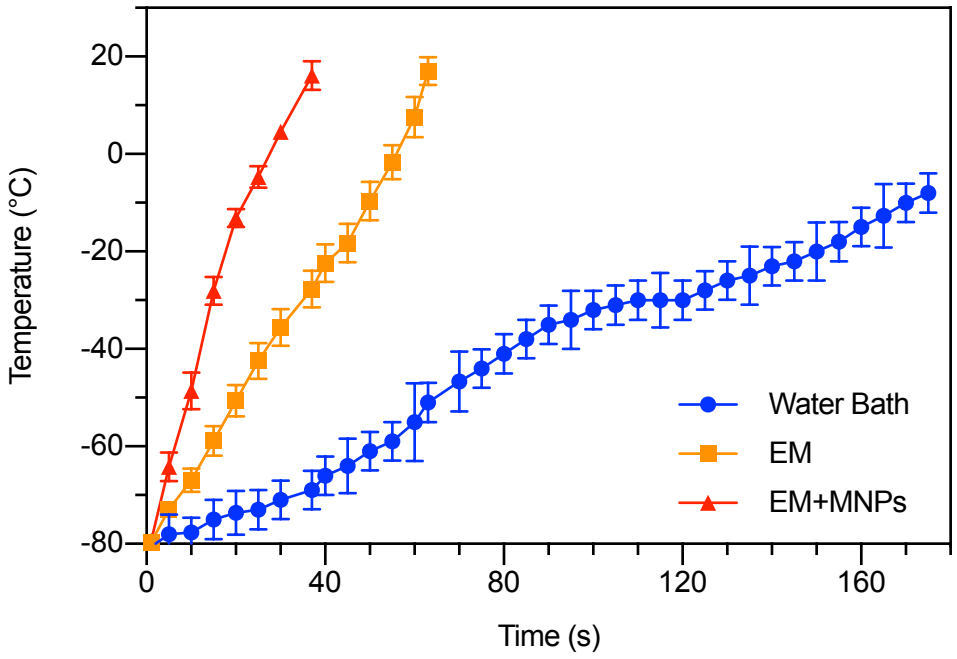

Figure 5-4. Temperature profile of different warming methods during the rewarming process

5.3.3 *The temperature gradient of different warming methods*

Temperature sensors were placed at the center and edge of the sample holder to monitor the temperature change at different positions. As shown in Figure 5-5, the uniformity of the temperature distribution of different warming methods was evaluated by the reading difference between the two sensors. The largest temperature difference of water bath, electromagnetic warming, and MNPs enhanced electromagnetic warming were $36.83 \pm 2.71, 6.53 \pm 0.59$, and 2.73 ± 0.50 ℃, respectively. The mean values $\pm$ standard deviations at each time point of all cases were determined based on six replicates (n=6).

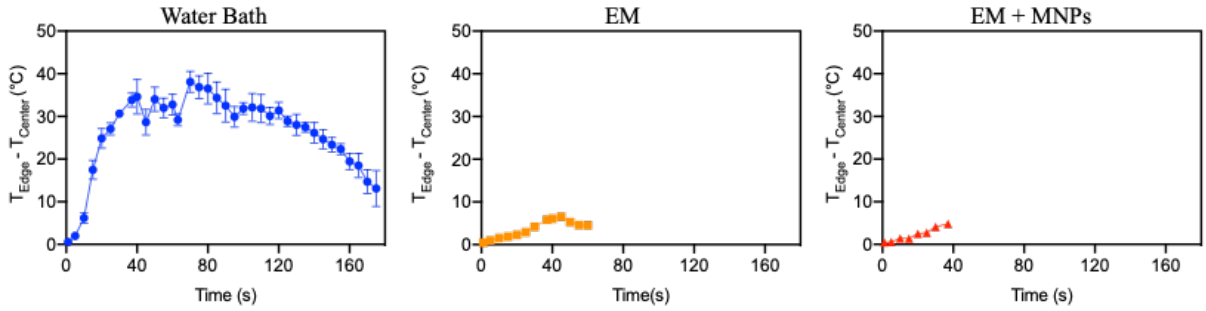

Figure 5-5. Temperature difference between the center and edge positions

Thermography photos of the sample holder bottom surface were also captured by the infrared camera for all three rewarming methods. As shown in Figure 5-6, the temperature gradient, defined as the difference between the maximum and minimum temperature divided by the distance, of the water bath, electromagnetic warming, and MNPs enhanced electromagnetic warming was 2.16, 1.28, and 0.47 °C mm^{-1}, respectively.

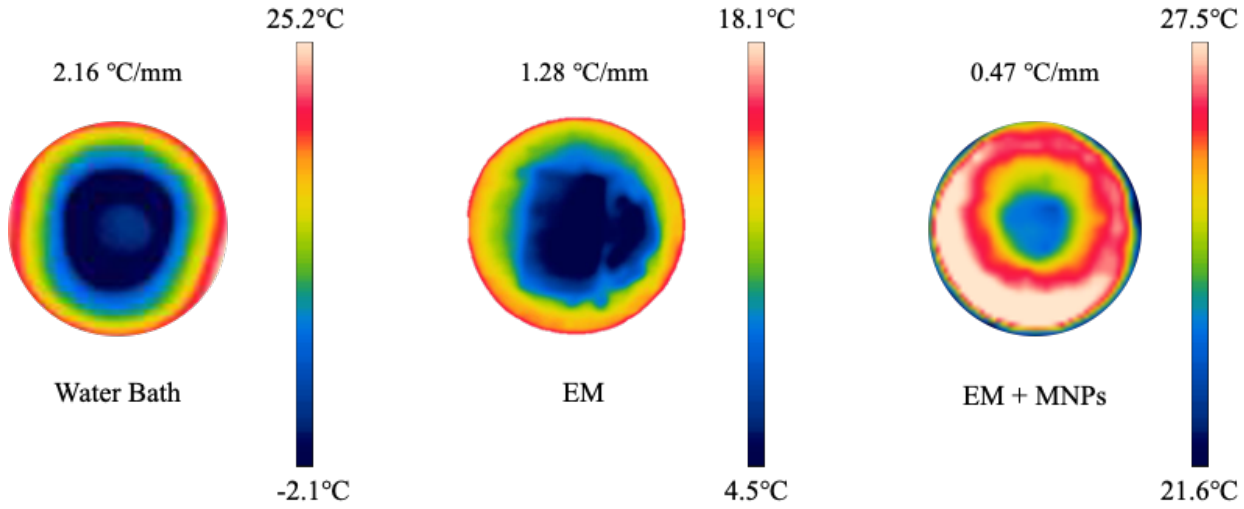

Figure 5-6. Surface temperature distribution of different rewarming methods

The addition of MNPs in the electromagnetic rewarming system significantly reduced the thermal gradient of the 25 mL large samples during the rewarming between −80 °C to 0 °C.

5.3.4 *Determination of the recovery rate of the Jurkat cells*

The membrane integrity of the Jurkat cells with different rewarming methods was determined by the Trypan Blue staining solution. As shown in Figure 5-7, the recovery rate of Jurkat cells of the water bath, electromagnetic warming, and MNPs enhanced electromagnetic warming were $48 \pm 9.3\%$, $78.3 \pm 6.2\%$, and $91.7 \pm 5.5\%$, respectively. The mean values $\pm$ standard deviations were determine based on twelve replicates (n=12).

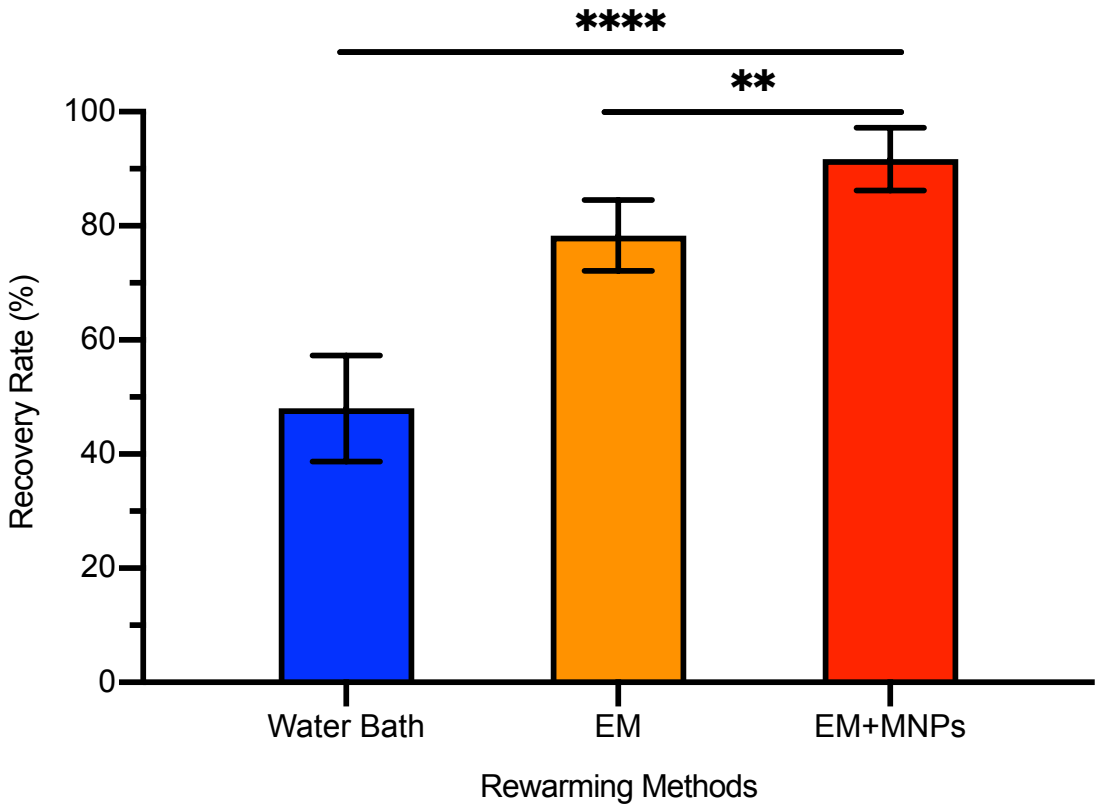

Figure 5-7. The recovery rate of the post-thawed Jurkat cells

The utilization of magnetic filed accomplished a faster and more uniformed heating outcome. As a result, the recovery rate of Jurkat cells was increased by 17.11% from electromagnetic warming ($P = 0.0027$), and almost doubled the recovery rate achieved by convective warming ($P < 0.0001$).

5.3.5 *Determination of the metabolic activity of the post-thawed cells*

As an immortalized cell line, a defining function of viable Jurkat cells is their proliferation rate or metabolic activity. The post-thawed Jurkat cells were incubated at 37 ℃ with 5% carbon dioxide, the metabolic activity was assessed by alamarBlue assay on a daily basis for the next three days. The metabolic activity of viable cells indicated by a change from resazurin (blue color) to resorufin (red color) through the reduction reaction of active living cells. Figure 5-8 represents the color change of Jurkat cells with different warming methods over time. In each 96-well, from left to right, the cells were from the fresh control group, MNPs enhanced electromagnetic warming, electromagnetic warming, water bath, and negative control group, respectively.

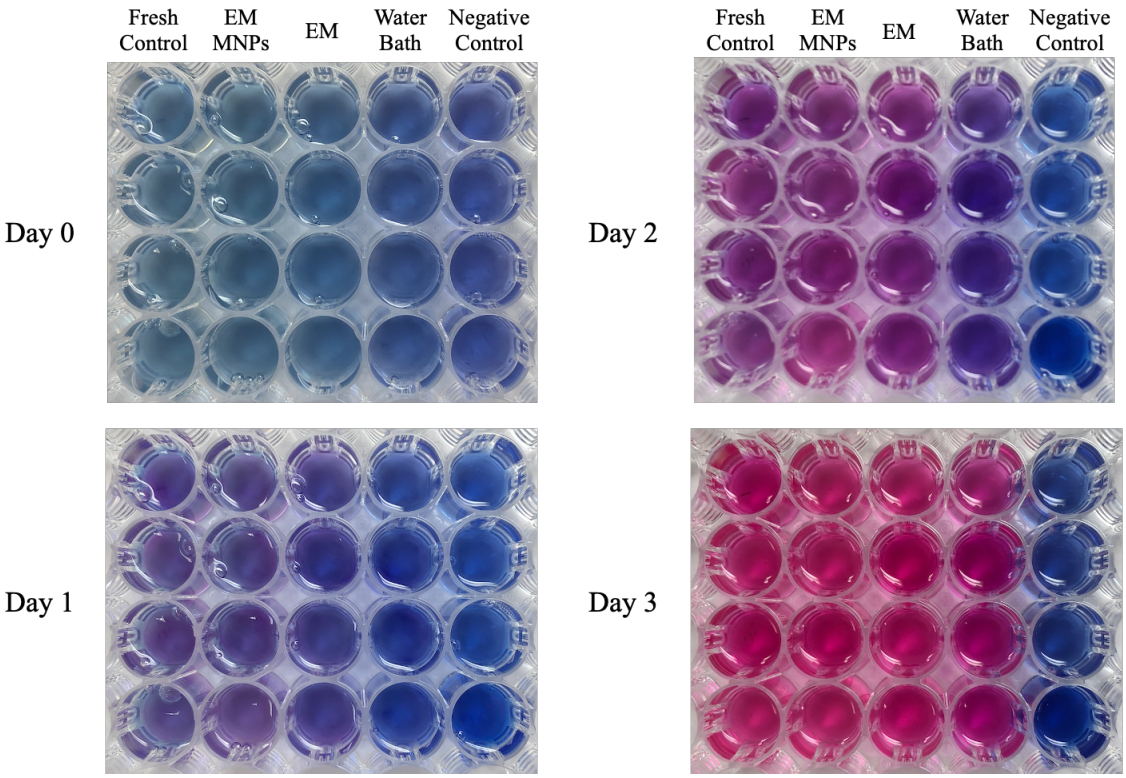

Figure 5-8. Determination of the post-thawed cells metabolic activity by alamarBlue

Start from day 1, both MNPs enhanced and electromagnetic warming groups demonstrated a similar color change to the fresh, positive control group, while the water bath remained the blue

and purple color. A confirmatory low metabolic activity was observed in the negative control group as the samples stayed blue color for all of the testing days. The quantified absorbance readings were obtained by the microplate reader, normalized to the fresh control group, and presented in the percentage in Figure 5-9. The mean values $\pm$ standard deviations were determined based on nine replicates (n=9).

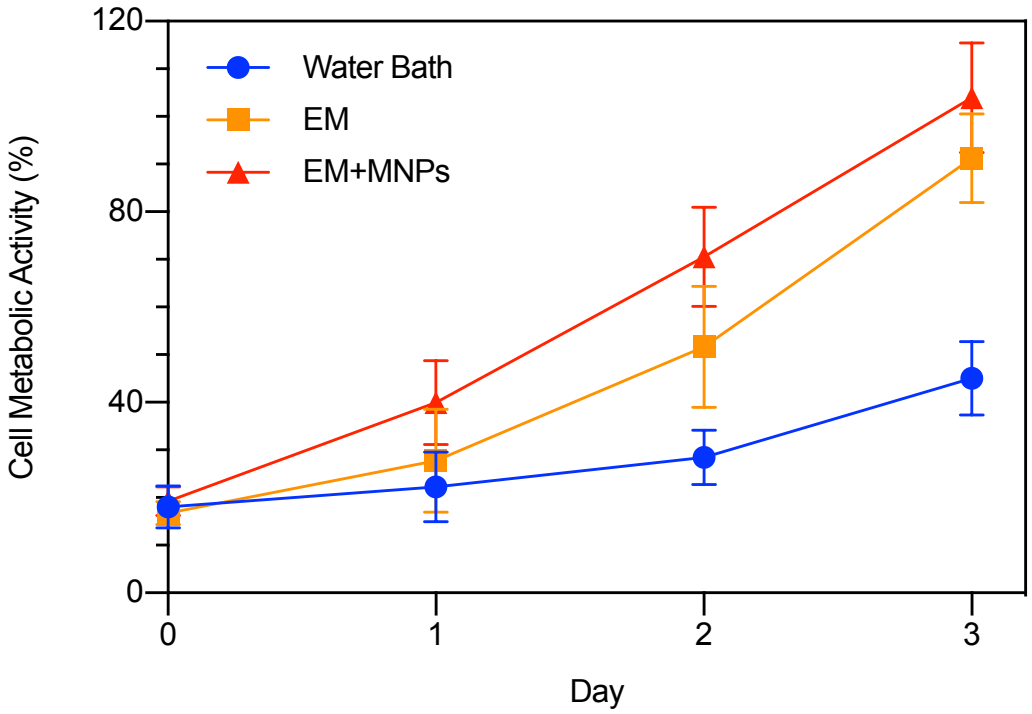

Figure 5-9. Post-thawed Jurkat cell metabolic activity of different rewarming methods

All of three rewarming methods demonstrated the increasing metabolic activity over time, while the MNPs enhanced and electromagnetic warming presented a much higher metabolic activity start from day 1. After three days of incubation, the average metabolic activity achieved by water bath, electromagnetic warming, and MNPs enhanced warming were $45 \pm 7.75\%$, $91.22 \pm 9.35\%$, and $103.92 \pm 11.54\%$, respectively. The addition of MNPs significantly improved the post-thawed Jurkat cell's biological functionalities from electromagnetic warming ($P = 0.0208$) and convective water bath ($P < 0.0001$). The metabolic activity value of MNPs

enhanced warming on day 3 indicated the cells' proliferation rate was similar to the fresh control group.

5.4 CONCLUSION

In this chapter, iron oxide superparamagnetic nanoparticles were added to the automatic electromagnetic resonance rewarming system to enhance the rapid and uniform rewarming of large cryopreserved biosamples. The heating test of 25 mL Jurkat cell showed a significant improvement in the warming rate (152.4 ℃) and final temperature uniformity (0.47 ℃ mm^{-1}) achieved by the MNPs enhanced electromagnetic warming.

The improved fast and homogenous heating also led to the better biological characteristics of the post-thawed Jurkat cells. The addition of MNPs almost doubled the recovery rate of Jurkat cell ($91.7 \pm 5.5\%$) from the convective water bath method and presented a similar metabolic activity to the fresh control group after three days of incubation.

The concentration of MNPs was limited to 0.1 mg Fe mL^{-1}, avoiding the side effects and high cost of the higher MNPs dosage. Moreover, the maximum amplified power was merely 400W due to the efficient electromagnetic energy utilization accomplished by the automatic resonant frequency adjusting system. The outstanding heating performance provided possibilities for the rewarming of tissue or organ preservation.

Chapter 6. VITREOUS CRYOPRESERVATION OF RABBIT JUGULAR VEIN USING MAGNETIC NANOPARTICLES ENHANCED ELECTROMAGNETIC RESONANCE REWARMING

6.1 INTRODUCTION

Transplantation remains the most effective treatment for those patients who suffered from chronic organ failures [121-125]. However, there is a long waiting list for transplantation due to the lack of an effective organ preservation method. The hypothermic storage could maintain the viability of hearts and lungs for up to 4 hours, intestine, pancreas, and liver for 8 to 12 hours, and kidney for up to 36 hours [126]. In such a short period, many tissues and organs are wasted due to insufficient time to match a recipient or exceeded the maximum storage time during transportation.

Cryopreservation, a technology to preserve the biomaterials at low temperatures to pause the biological and chemical reactions, is a potential solution to long-term tissue and organ preservation. The small biological systems, including red blood cells [10], oocytes [11, 12], liver cells [13], etc., have been proved successfully preserved by cryopreservation. Plus, the breakthroughs in vitrification, forming an amorphous glass state by fast freezing and adding a higher CPA concentration, reduced the cryoinjuries during the cooling process[1, 99, 100, 127]. But, two technological challenges remain in the thawing. First, a fast rewarming rate that is higher than the critical warming rate (CWR) is needed to avoid the devitrification that would form the ice crystals to rupture the cells. Second, this fast rate needs to be homogeneously distributed within

the entire sample to prevent the temperature difference induced thermal stress that could lead to the fracture of the material. Therefore, a rapid and uniform rewarming technique is needed.

By vibrating the electrical dipole molecules, a high-power electromagnetic (EM) cavity heating system can generate volumetric dielectric heating that overcomes the problems of low thermal conductivities and high specific heats of biological materials, which rules out the possibility of using a traditional water bath for thawing large cryopreserved samples [53, 85]. By adding the magnetic nanoparticles (MNPs), the coupled magnetic field's energy could also be harnessed to improve warming rates and uniformity further. The recent ‘nanowarming’ approach succeed in the cryopreservation of porcine carotid artery and porcine aortic heart valve leaflet tissues by utilizing a commercially available radio-frequency (RF) coil system [115]. Nevertheless, due to the low electric field intensity at the center position, the heating performance by RF coil relied on the high dosage of MNPs, which brought the concerns of cytotoxicity [112, 116].

In this chapter, the developed electromagnetic resonance rewarming system was adopted to the warming test of vitrified rabbit jugular veins. Because of the resonant frequency tracking system, the high energy conversion efficiency allowed the low concentration of MNPs and smaller energy input. The heating results were compared with the convective water bath and natural air convection method and evaluated by various biological functionality assessments.

The venous grafts warmed by MNPs enhanced electromagnetic system showed comparable post-thawed metabolic activity and biomechanical test results to the fresh tissues, which indicated the improved warming system is a promising alternative strategy for dealing with the rewarming problems concerning tissue and organ preservation.

6.1.1 *Tissue harvesting and preparation*

In this study, all of the procedures were performed in strict accordance with the National Institutes of Health (NIH) guidelines for the care and use of laboratory animals [128]. Rabbit jugular veins were procured from adult male New Zealand rabbits (2-3 kg, N = 26). The fresh veins were obtained within 30 min of death following the procedures approved by the Institutional Animal Care and Use Committee of the University of Washington, Seattle, Washington. All tissues used were considered bonafide excess; therefore, no animals were specifically euthanized for this study.

The fresh veins were harvested and immersed in Krebs-Henseleit buffer (Sigma-Aldrich) immediately, then transferred to the research lab within 1 hour. Jugular veins were immersed and rinsed with wash media (phosphate buffered saline (PBS) plus antibiotics (100 units/mL penicillin, 100 μg/mL streptomycin, and 0.25 μg/mL amphotericin B (Gibco)) for 5 minutes and then cleared of fatty tissue. After that, the veins were sectioned into vein segments with the following dimensions: inner diameter, 2 to 4 mm, wall thickness, 1 to 2 mm, and length, 20 to 40 mm. The sectioned veins were placed on a Petri dish and gently patted dry with Kimwipes. Then, the weight of each segment was obtained. All of the procedures performed at the research lab were in a biological safety cabinet.

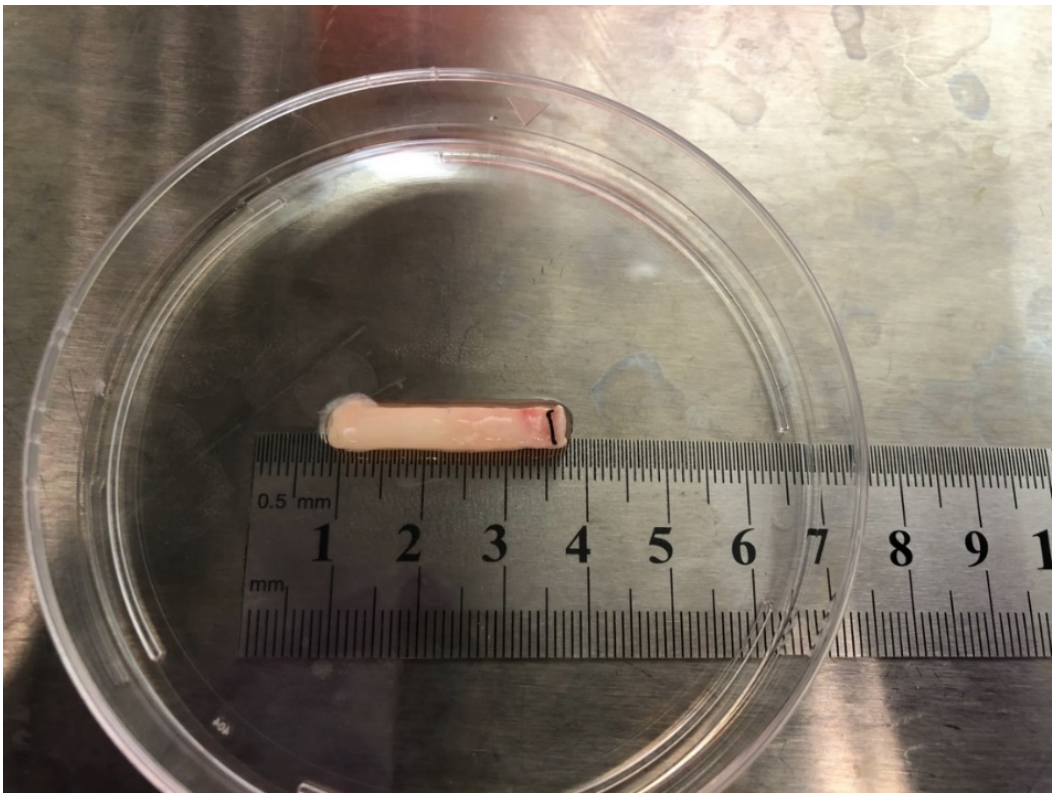

Figure 6-1. Sectioning the Jugular veins into 20-40 mm segments

6.1.2 *Determination of viability of tissues before and after warming*

Prior to the cooling and warming tests, the sectioned veins were incubated with growth media plus 10% alamarBlue solution at 37 ℃ and 5% carbon dioxide for 2 hours. The absorbance of each sample was determined by the microplate reader at 570 and 600 nm from an aliquot of the solution. The readings were averaged from two replicated to establish the baseline.

After the rewarming treatments, the same protocol was repeated to obtain the readings of the post-thawed tissues. The viability of each vein segment was determined by calculating the absorbance before and after the tests and normalized to the fresh control group.

6.1.3 *MNPs embedded vitrification solution*

DPVP solution containing 41% (w/v) dimethyl sulfoxide (DMSO) and 6% (w/v) polyvinylpyrrolidone (PVP) was chosen as the vitrification solution. The dielectric properties were measured in chapter 4, and the preliminary cooling and warming tests proved the solution could achieve vitrification at low temperature and prevent devitrification with electromagnetic warming system.

10 nm iron oxide superparamagnetic nanoparticles with monolayer PEG coating were added to the DPVP solution at a low concentration of $0.1\ \mathrm{mg\ Fe\ mL^{-1}}$. The PEG coating could effectively inhibit the aggregation of nanoparticles in the aqueous solution.

6.1.4 *Vitrification solution loading and removal processes*

The addition of DPVP solution was performed on ice between 0 to 4 ℃ with a multi-step method to reduce the toxicity and osmotic injury to the tissues. As shown in Figure 6-2, the gradually increased CPA concentration for each step was controlled as 10%, 25%, 50%, and 100%. The interval between each concentration was 5 minutes to allow the system to reach an equilibrium state. MNPs were only loaded at the last step.

By the end of CPA loading, the total volume of the sample reached 25 mL.

A similar stepwise method was applied in the CPA removal procedure and showed in Figure 6-2. The gradually increased CPA concentration for each step was controlled as 50%, 25%, 10%, and 0% with a 5-minute interval.

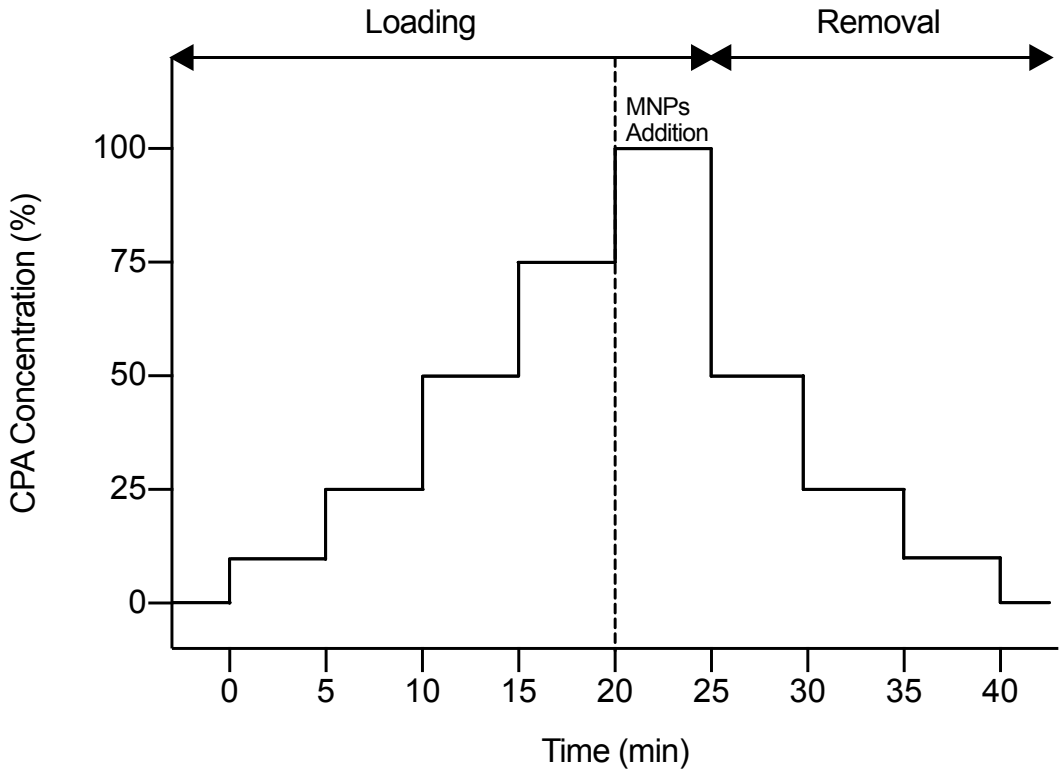

Figure 6-2. Loading and removal of DPVP solution and MNPs

6.1.5 *Cooling device and method*

The device and method for vitrification solution cooling introduced in chapter 4 were applied in this study. The CPA loaded cylindrical sample holder was placed in the rack and transferred to the liquid nitrogen dewar. The nylon string adjusted the height of the holder inside the dewar to control the cooling rate. Two temperature sensors were inserted in the center and edge of the sample to monitor the change of the temperature.

Once the temperature reached $-150℃$, the sample was picked up, and the vitrification status was verified by visual inspection. The vitrified samples were stored in the liquid nitrogen storage dewar for at least 24 hours.

6.1.6 *Rewarming methods*

Three rewarming methods were adopted, natural air convection as slow warming, convective water bath as intermediate warming, and MNPs enhanced electromagnetic warming.

In natural air convection warming, the vitrified sample was put on the top of the lab bench at room temperature ($21-23$ ℃). The warming was terminated when both temperature sensors at center and edge reached 0 ℃, and there were no visual observation of ice crystals.

In convective water bath warming, the vitrified sample was quickly transferred to the pre-warmed water bath at 37 ℃. The bath was shaking at 60 RPM in an orbital motion during the warming. The warming was terminated when both temperature sensors reached 0 ℃, and there were no visual observation of ice crystals.

In MNPs enhanced electromagnetic warming, the vitrified sample was quickly transferred to the resonant cavity. The maximum power was limited to 400 W, and input frequency was automatically adjusted by the resonant frequency monitoring and controlling system. The warming was terminated when both temperature sensors reached 0 ℃.

6.1.7 *Biomechanical assessments of the post-thawed tissue*

Right after the unloading of the vitrification solution, the post-thawed veins were cut into vein rings in the length of 3-5 mm, then incubated in the growth media at 37 ℃ for 2 hours. The biomechanical function of the fresh control tissue and preserved vein segments were assessed by an isometric high-resolution force transducer (PASCO Scientfic Inc., Evanston, IL). As shown in Figure 6-3, two hooks were placed in a 15-mL Falcon tube that served as the container of PBS at 37 ℃. The lower hook was fixed at the bottom of the tube; the other one was connected to the force transducer by a rigid string. Each vein ring was mounted between the two hooks, and the

contractile tensions were measured by adding different concentrations of Histamine (Alfa Aesar, Haverhill, MA).

When investigating the relaxation response, the previous solution was removed and replaced with Sodium Nitroprusside (Thermo Fisher Scientific) solution. Then, the cumulative dose-response curves were produced to assess the tissues' response to the precontraction with Histamine at 10^{-1} M.

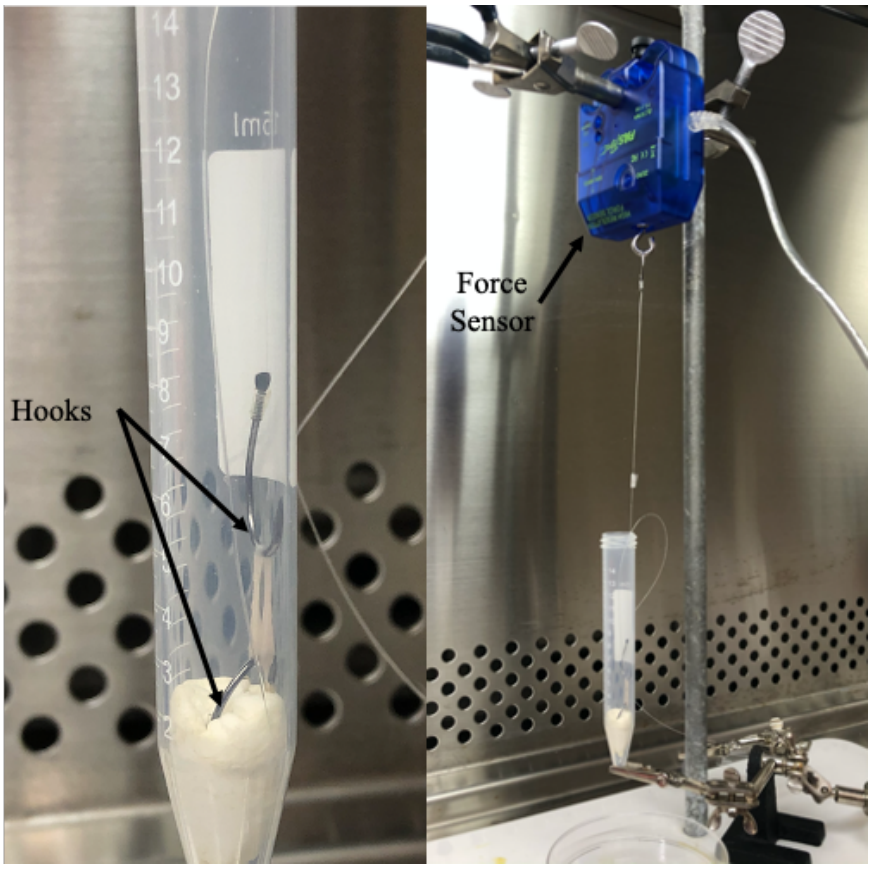

Figure 6-3. Measurements of contraction and relaxation of vein rings. Left, detailed setup of the hooks. Right, an overview of the measurement system.

6.1.8 *Determination of the mitochondrial membrane potential*

Tetramethylrhodamine, methyl ester [TMRM, (Thermo Fisher Scientific)] assay, a small and membrane-permeable dye, was used to determine the mitochondrial membrane potential of

the post-thawed tissues. The vein rings of the fresh control group and different rewarming methods were incubated in the 96-well at 37 ℃ and 5% carbon dioxide for 2 hours. Then, the growth media was removed and replaced with TMRM solution at 100 nM concentration. The vein rings were put back in the incubator for another 30 minutes. Fluorescence readings were determined by a plate reader (SpectraMax i3X, Molecular Devices, LLC., San Jose, CA) at 548 nm using the TRITC filter set. The relative fluorescence units (RFU) were normalized to the fresh control group and presented as a percentage.

6.1.9 *Tissue fixation and histology imaging*

The control groups and post-thawed vein rings were immersed in 4% Paraformaldehyde [PFA, (Boster Bio, Pleasanton, CA)] and transferred to 4 ℃ freezers and stored overnight. The samples were sent to the Histology and Imaging Core (HIC) at the University of Washington for the following tissue processing, embedding, Hematoxylin and eosin staining, and histology imaging.

6.1.10 *Fresh control and negative control groups*

A fresh control sample is defined as the jugular veins without any CPA loading, cooling, or warming treatments.

A negative control sample is defined as the jugular veins loaded with PBS and directly immersed in the liquid nitrogen without any CPA, then warmed with natural air convection method.

6.1.11 *Statistical analysis*

All of the viability, mitochondrial membrane potential, and histology image analysis were normalized to fresh controls. The numerical data of contractile tensions, relaxation responses are presented as means ± standard deviation (SD). The one-way analysis of variance (ANOVA) with post hoc test (Tukey's multiple comparisons) was performed on the controlled and treated samples' viability and mitochondrial membrane potential. A two-tailed *t*-test was performed on the histology image analysis.

6.2 RESULTS AND DISCUSSION

6.2.1 *Temperature profile during the cooling*

The recorded temperature profiles of the center and edge locations for all cases are shown in Figure 6-4. The average cooling rate was $5.69\ ℃\ \mathrm{min}^{-1}$. The mean values ± standard deviations at each time point were determined based on six replicates (n=6).

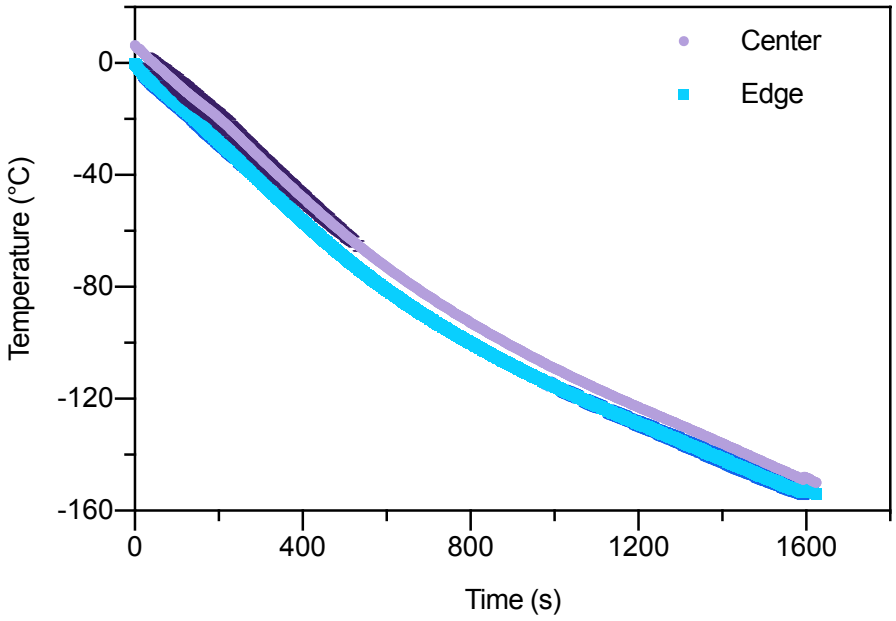

Figure 6-4. Temperature profiles of the center and edge positions during the cooling

The thermal gradient was calculated by the difference between the center and edge values. The results are shown in Figure 6-5. The largest temperature difference during the cooling was 9.27 ± 1.49 ℃.

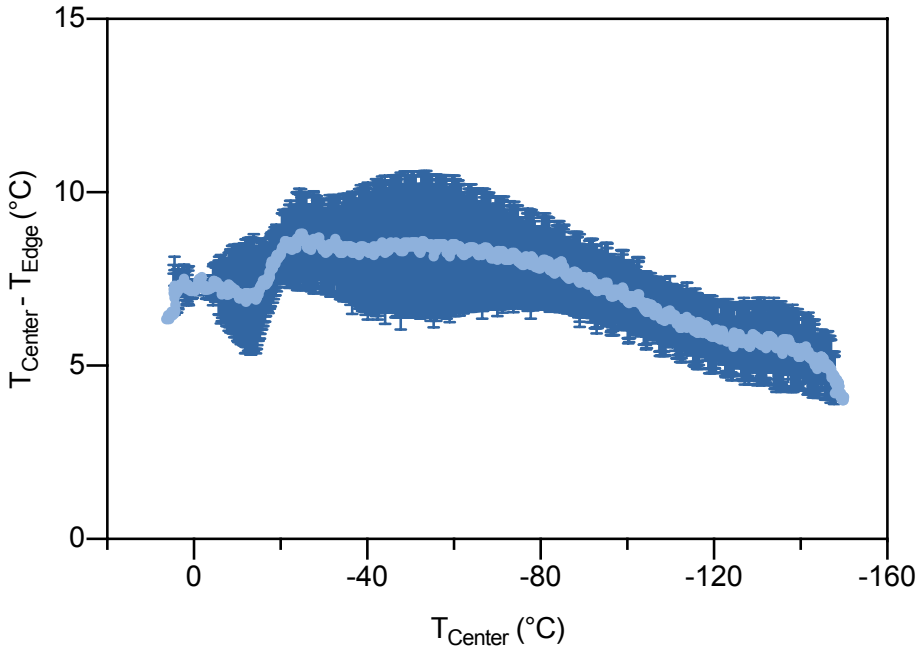

Figure 6-5. Temperature difference from center to edge during the cooling

6.2.2 *Vitrification verification at* -150 ℃

Rapid cooling is needed to achieve the vitrification below the solution's glass transition temperature (T_g). The vitrification of the sample solution was verified by visual observation at -150 ℃. The representative pictures of vitrified, cracked, and frozen samples are shown in Figure 6-6. The cooling rate was controlled by the distance between the sample solution and the surface of liquid nitrogen, which could be adjusted through the nylon string. The cacked and frozen sample might be due to the slow cooling that slower than the critical cooling rate or the fast cooling that led to the non-uniform temperature distribution and caused the thermal stress. The height of the sample holder within the liquid nitrogen dewar was adjusted based on the observation of the solution status at -150 ℃.

Only the vitrified samples were stored in the dewar and conducted the rewarming test.

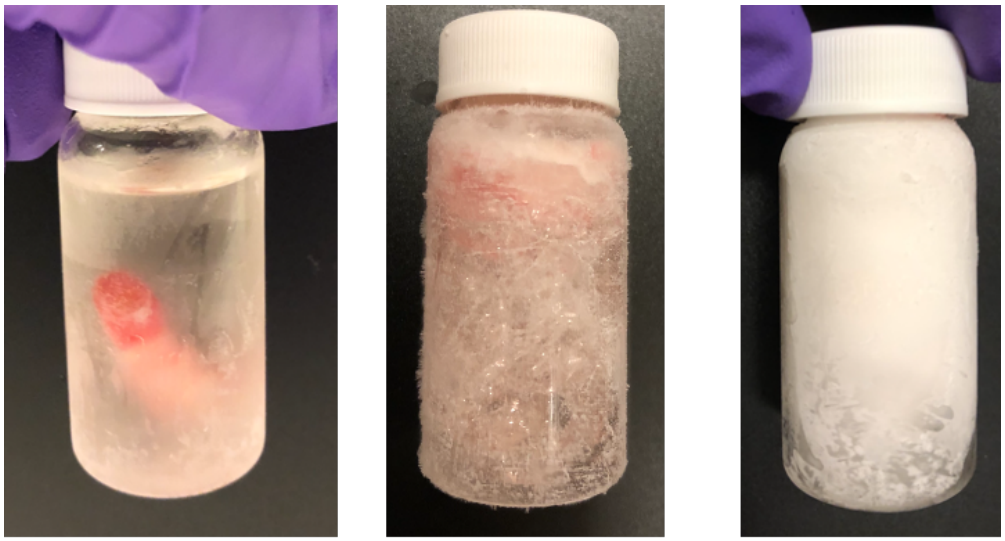

A. Vitrified B. Cracked C. Frozen

Figure 6-6. Vitrification verification of tissues at -150 ℃

6.2.3 *Temperature profiles of different rewarming methods*

The recorded temperature profiles at the center and edge positions of MNPs enhanced electromagnetic rewarming, convective water bath, and natural air convection are shown in Figure 6-7, Figure 6-9, and Figure 6-11. The mean values ± standard deviations at each time point of all cases were determined based on six replicates (n=6).

The thermal gradient of MNPs enhanced electromagnetic rewarming, convective water bath, and natural air convection are shown in Figure 6-8, Figure 6-10, and Figure 6-12.

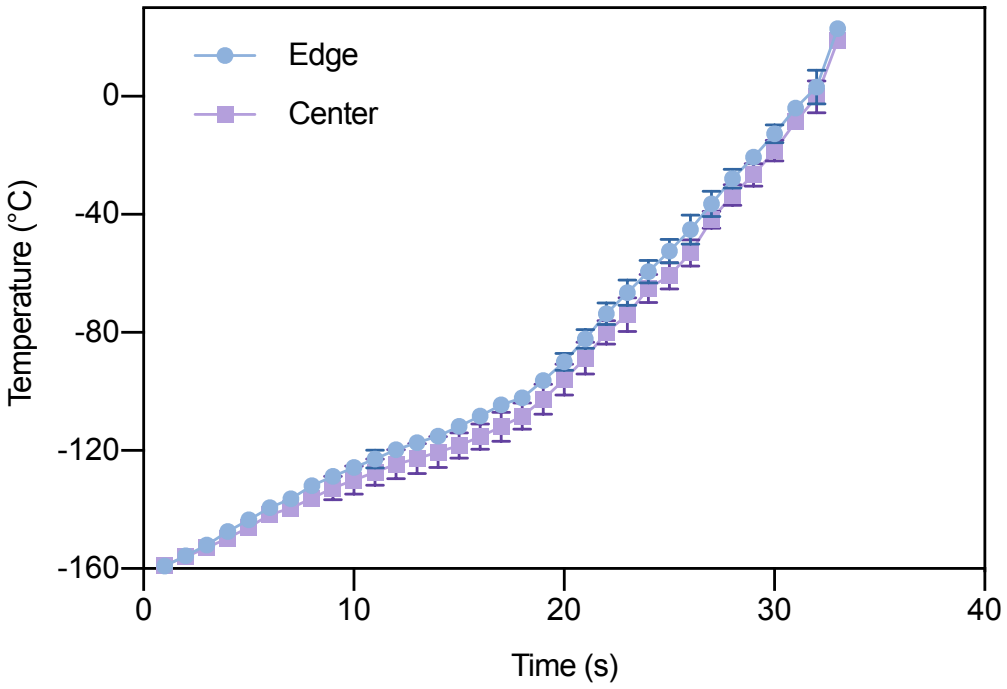

Figure 6-7. Temperature profiles of the MNPs enhanced electromagnetic rewarming

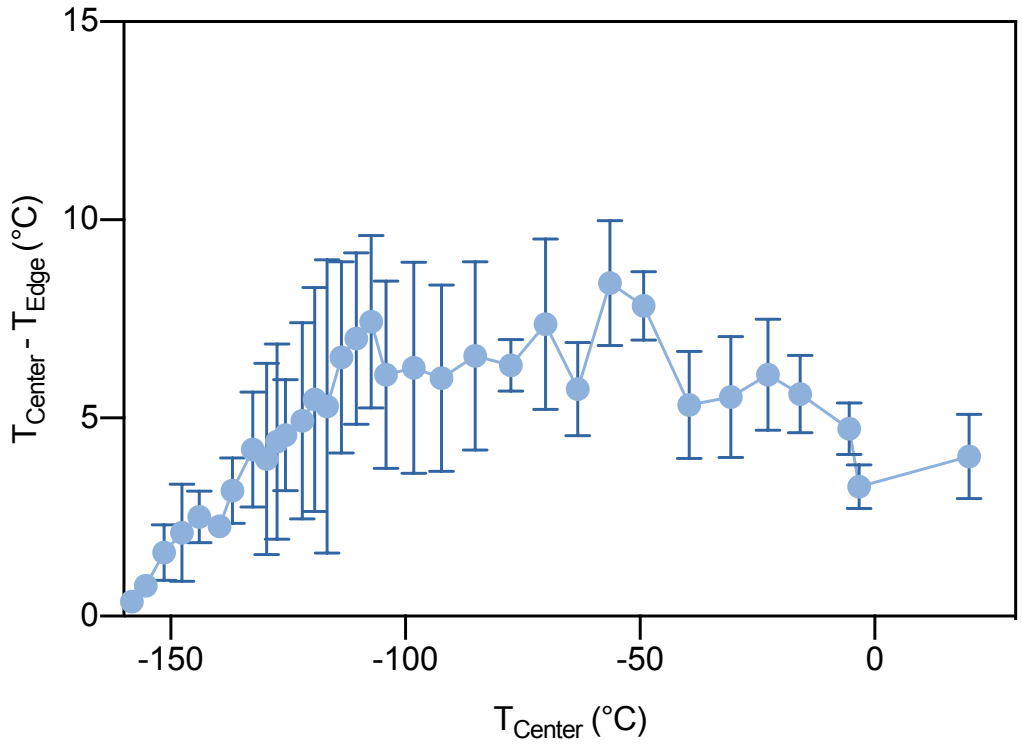

Figure 6-8. Thermal gradient of the MNPs enhanced electromagnetic rewarming

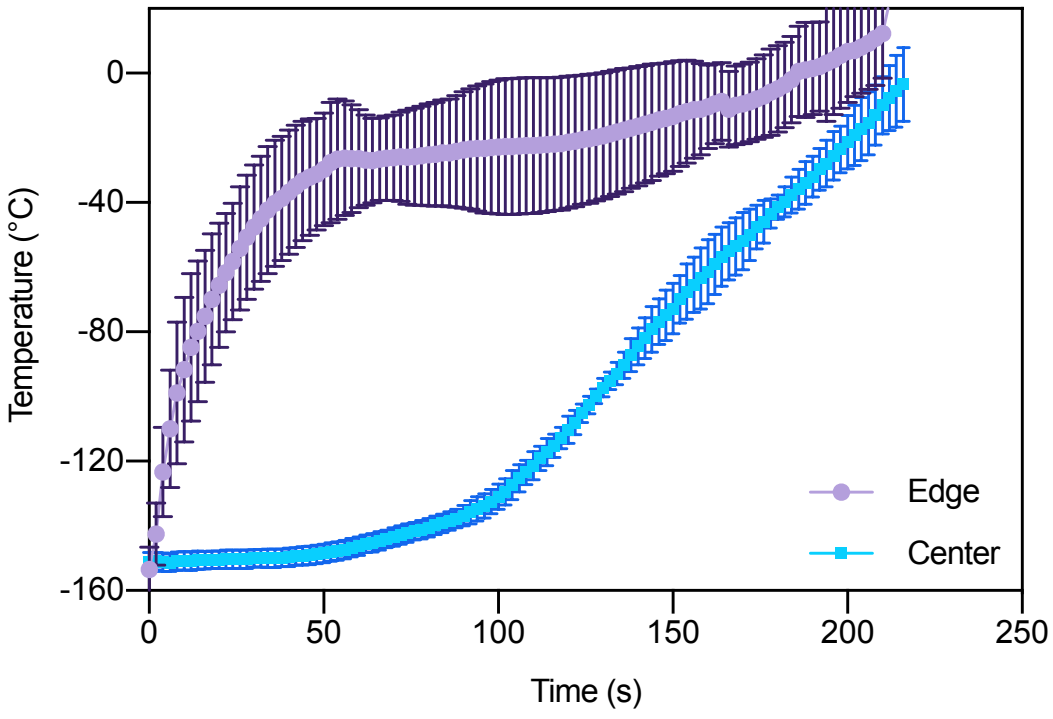

Figure 6-9. Temperature profiles of the convective water bath rewarming

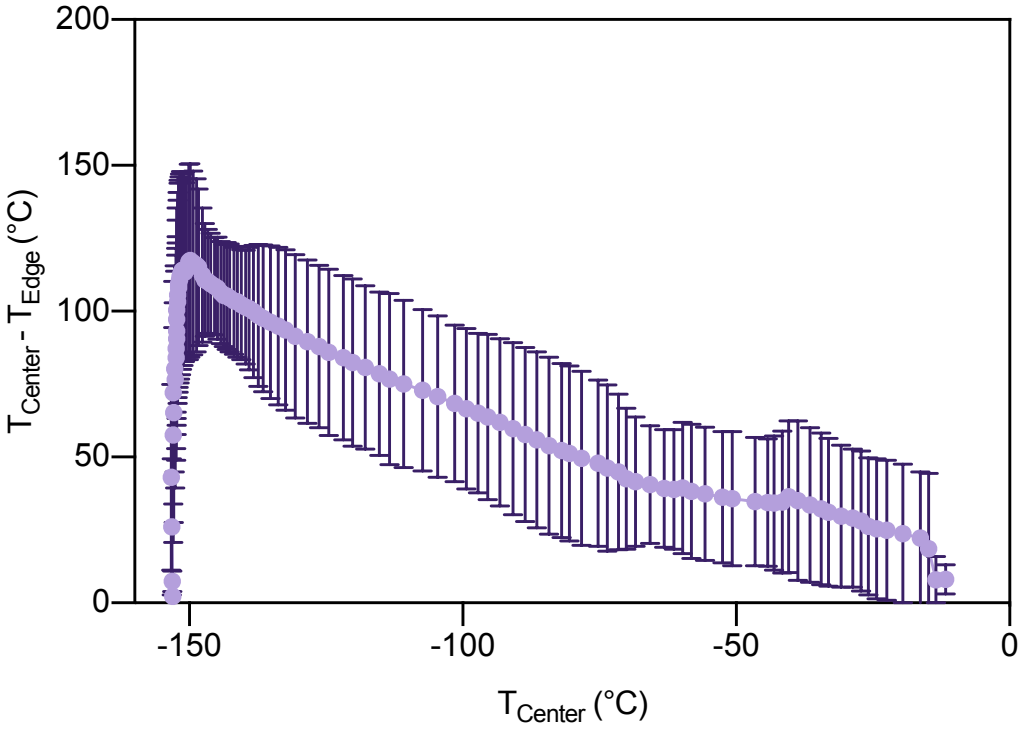

Figure 6-10. Thermal gradient of the convective water bath rewarming

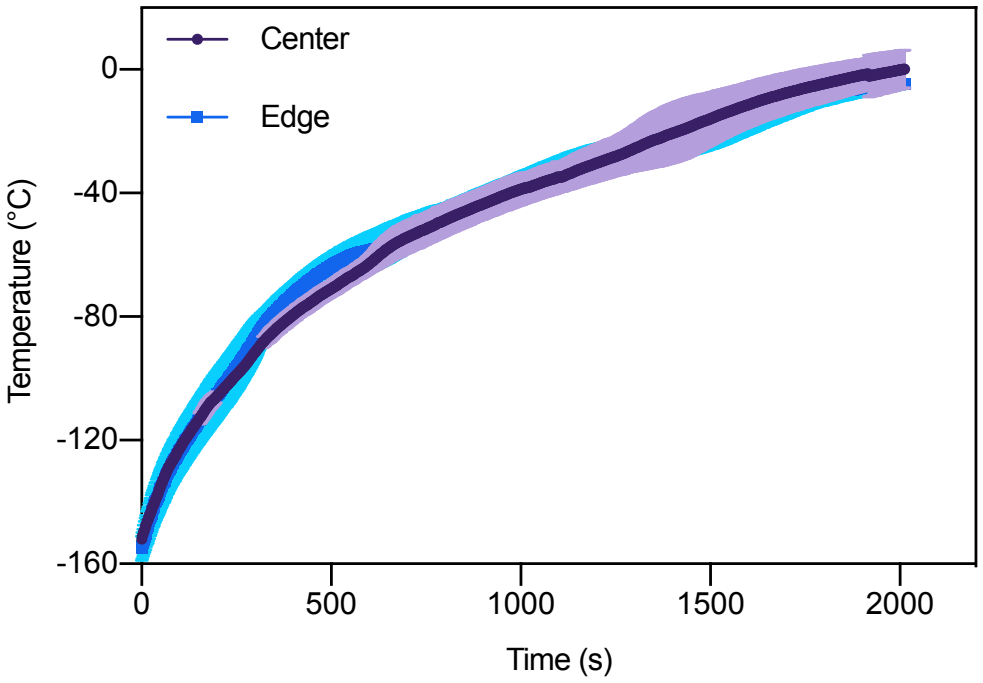

Figure 6-11. Temperature profiles of the natural air convection rewarming

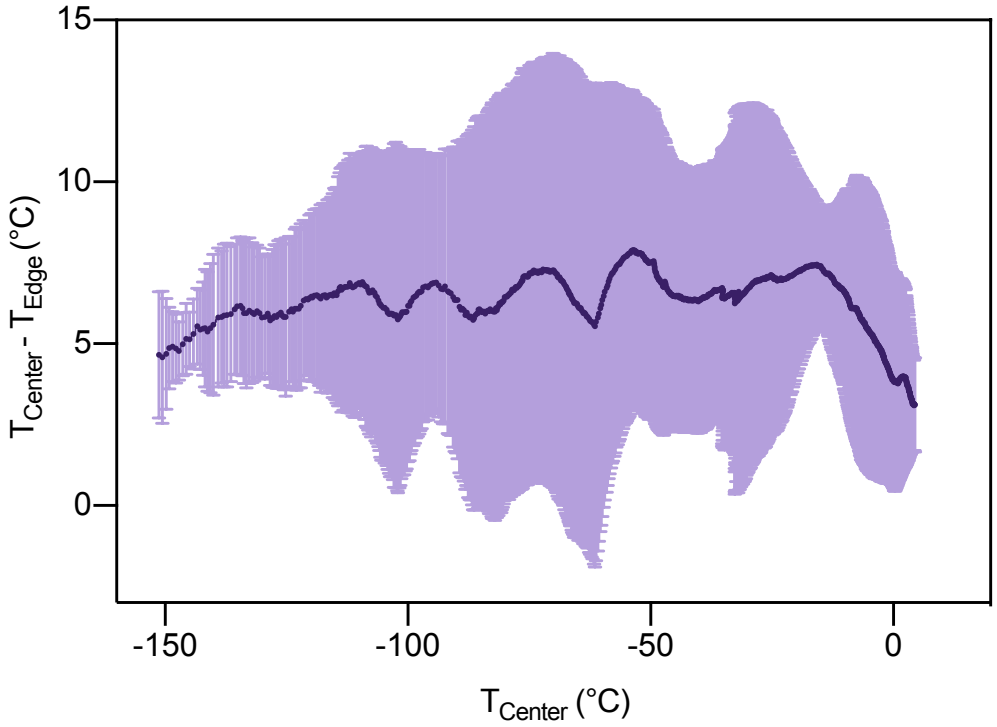

Figure 6-12. Thermal gradient of the natural air convection rewarming

The average rewarming rate of the natural air convection, convective water bath, and MNPs electromagnetic warming was achieved at 4.53 ± 0.14, 46.52 ± 4.85, and 326.91 ± 7.55 ℃ min^{-1}, respectively.

The MNPs enhanced electromagnetic warming succeeds the rapid and uniform warming. The largest thermal gradient was limited to less than 10 ℃, while the convective water bath method reached more than 100 ℃. Especially at the beginning of the thawing, the sudden temperature change at the exterior surface of the sample holder in convective heating caused the vast temperature difference. At such a large thermal gradient, the induced thermal stress could tear up the tissues. The natural air convection warming also accomplished uniform thawing. The largest thermal gradient was within 15 ℃ because the slow warming rate allowed sufficient time for the heat transfer within the sample. However, the slower heating also favors the devitrification that would rupture the cells.

6.2.4 *Viability of different rewarming methods*

The viability of the post-thawed tissues was measured by comparing the resazurin (alamarBlue) readings before and after the warming tests. The results are shown in Figure 6-13. The viability of MNPs enhanced electromagnetic warming, water bath, and natural air convection was $32.13 \pm 11.04\%, 26.73 \pm 7.75\%$, and $86.54 \pm 5.63\%$. The mean values $\pm$ standard deviations were determined based on nine replicates (n=9).

The viability of MNPs enhanced electromagnetic warming was comparable to the fresh control group ($P = 0.3675$) and significantly better than the water bath ($P < 0.0001$) and natural air convection ($P < 0.0001$). The large decline of viability in the water bath and air warm might be due to devitrification caused by the slow warming rate.

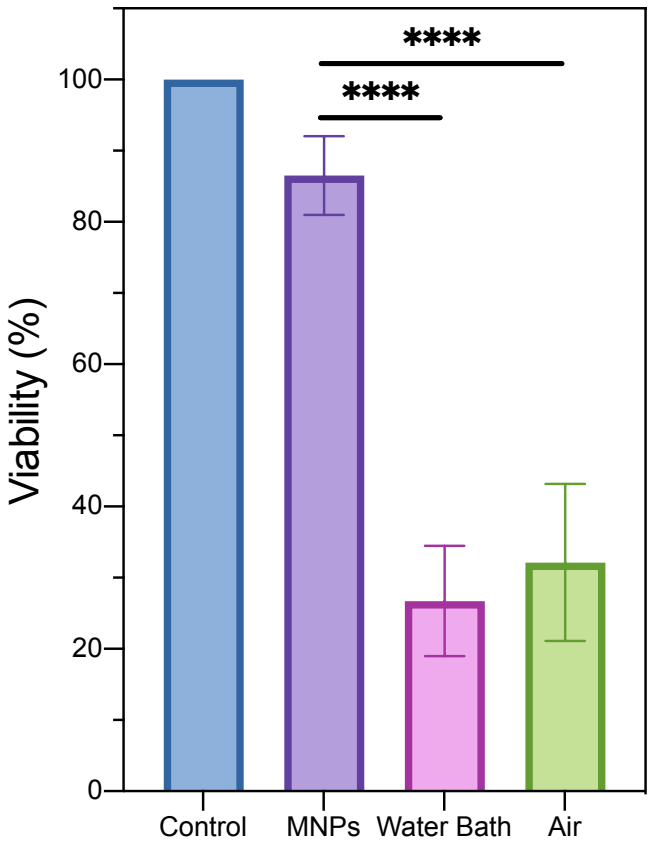

Figure 6-13. Viability of rabbit jugular vein measured by alarmBlue

6.2.5 *Histology image analysis*

Hematoxylin and eosin (H&E) stained histological images were obtained by HIC at the University of Washington. The results are shown in Figure 6-14 and further supported the previous viability data.

The MNPs enhanced electromagnetic rewarming (A) demonstrated well-defined intact nuclear morphology and structure of the venous smooth muscle cells. In contrast, the samples warmed by water bath (B) and air convection (C) showed disruptive structure and dispersed nuclei with apparent hollow space between cells, possibly due to the devitrification and osmotic injury.

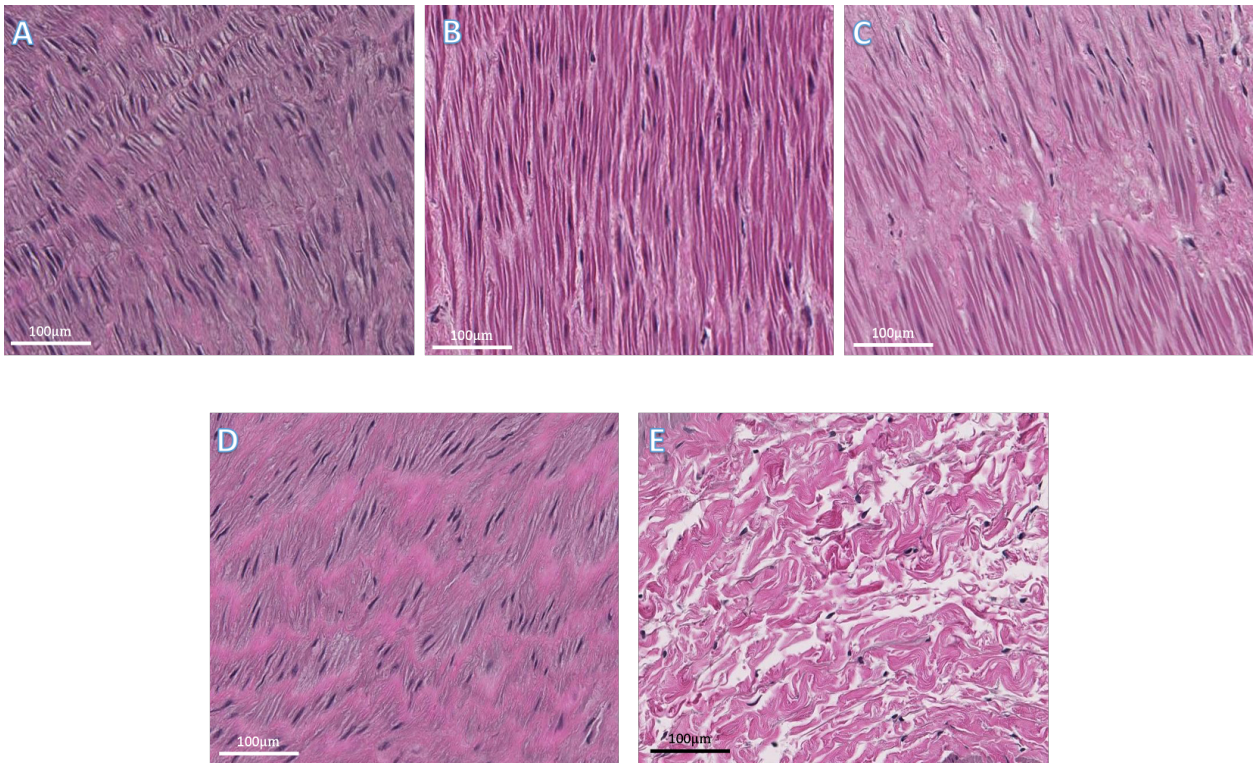

Figure 6-14. Histological images of H&E stained samples. A, MNPs enhanced electromagnetic warming; B, Convective water bath; C, Natural air convection; D, Fresh control; E, Negative control. Scale bars, 100 μm.

Comparing the fresh control (D) and negative control (E), the formation of ice could lead to the rupture of the cells and disruptive layered tissues, which could be observed as more hollow

space (white area) in the histological images. Quantitative analysis of the images was performed by comparing the tissue area (total area – hollow space) of different warming methods. The area was determined by ImageJ software, and the results were normalized to the fresh control group and presented in the percentage.

As shown in Figure 6-15, no statistical difference found between the MNPs electromagnetic warming and fresh control group ($93.04 \pm 7.70\%$ and 100%, $P = 0.1222$), while significantly higher than water bath ($78.17 \pm 6.72\%$, $P = 0.2002$), air warmed ($71.08 \pm 8.67\%$, $P = 0.0002$), and negative control ($49.98 \pm 7.86\%$, $P < 0.0001$). The mean values $\pm$ standard deviations were determined based on three replicates (n=3 slides per case).

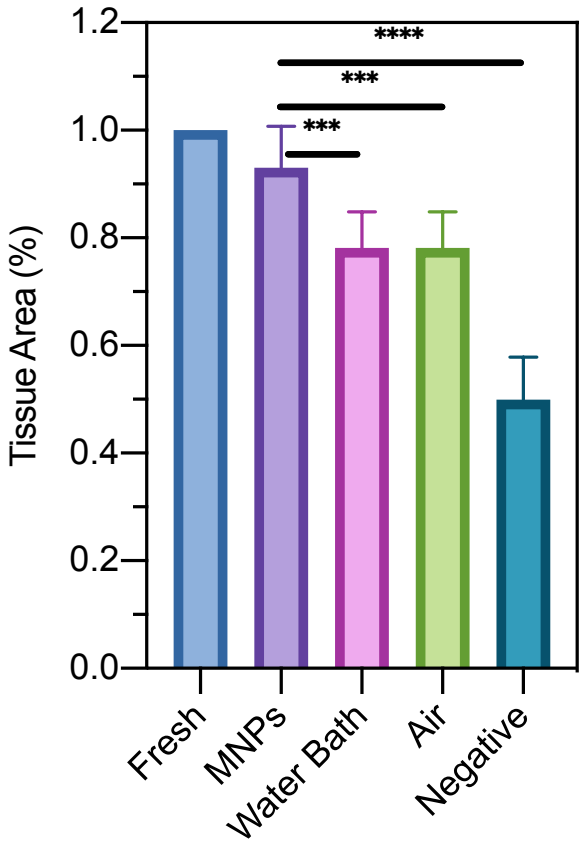

Figure 6-15. Tissue area of the post-thawed veins

6.2.6 *Contractile tensions of post-thawed vein rings*

Like all other smooth muscle tissues, contraction and relaxation are the two major biological functions of the jugular veins to maintain blood pressure and transport deoxygenated blood. A dysfunctional jugular vein could cause a life-threaten problem, including thrombosis, heart failure, trauma, etc. [129-132]. After loading the agonist (Histamine), the contractile tension of post-thawed vein rings was measured by the force transducer. The maximal contractile responses at each chemical's concentration are presented in Figure 6-16.

The fresh control and MNPs enhanced electromagnetic warming samples showed initial responses at a lower concentration and enlarged tension as the concentration increased. The water

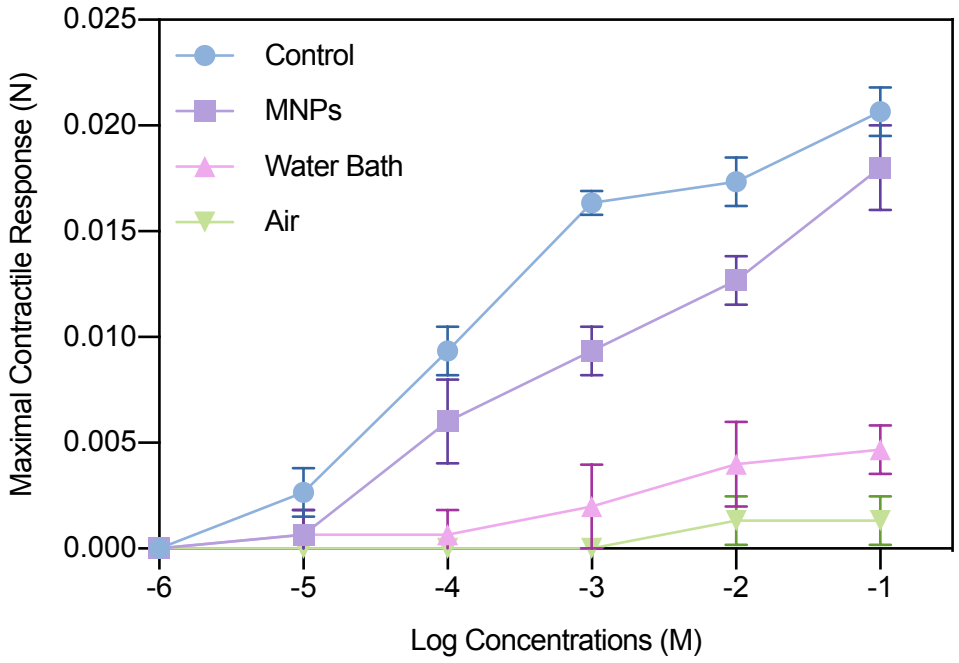

Figure 6-16. Maximal contractile tension of post-thawed vein rings under different concentrations of Histamine

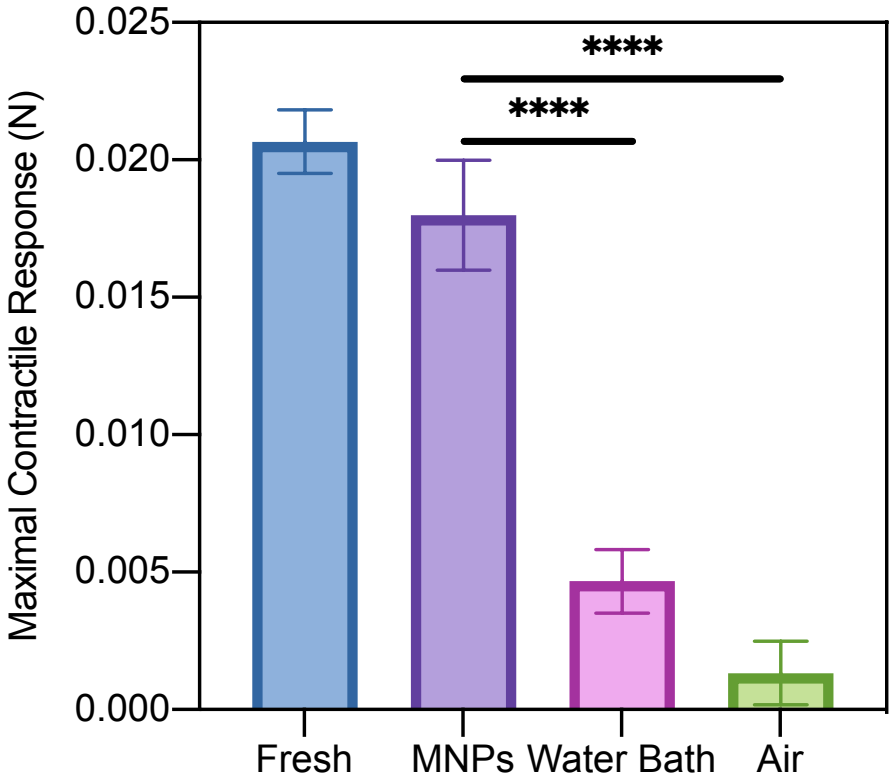

Figure 6-17. Maximal contractile tension with Histamine at 10^{-1}M

bath and air warm indicated vein reaction to the stimulate at high concentration, but smaller tension was recorded. The maximal contractile responses of all methods at the highest Histamine concentration are shown in Figure 6-17.

The maximal contractile tension of fresh control, MNPs, water bath, and air warmed was captured at 0.021 ± 0.001, 0.018 ± 0.002, 0.005 ± 0.001, and 0.002 ± 0.001 N. The MNPs warmed results were comparable to the fresh control ($P = 0.1165$) and significantly higher than water bath ($P < 0.0001$) and ($P < 0.0001$). The mean values $\pm$ standard deviations were determined based on nine replicates (n=9 rings per case).

6.2.7 *Relaxation response of post-thawed vein rings*

Endothelium-independent relaxation was determined by Sodium Nitroprusside (SNP). As shown in Figure 6-18, fresh control and MNPs warmed vein rings presented increasing smooth muscle relaxation response to the dosage increment. Water bath and air warmed started to show slight response to antagonist at higher concentration (10^{-3} and 10^{-1}M).

The maximum relaxation response of fresh control, MNPs, water bath, and air warmed was captured at 0.019 ± 0.001, 0.016 ± 0.002, 0.003 ± 0.001, and 0.001 ± 0.001 N. The MNPs wared results were comparable to the fresh control ($P = 0.2173$) and significantly higher than water bath ($P < 0.0001$) and ($P < 0.0001$). The mean values $\pm$ standard deviations were determined based on nine replicates (n=9 rings per case).

Comparing to the previous maximal contractile tension, fresh control and MNPs warmed relaxation response succeed more than 90% precontraction, and superior to the water bath (66.7%) and air warmed (~50%). The significantly better smooth muscle function in the MNPs warmed method indicated the rapid and uniformed electromagnetic warming system preserved tissue integrity and biological functionalities.

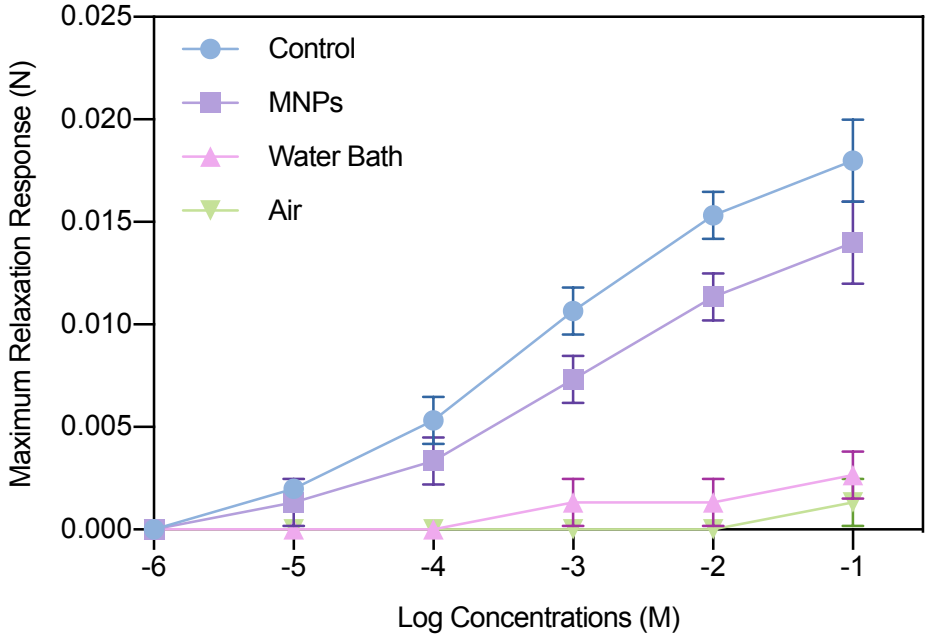

Figure 6-18. Maximum relaxation of post-thawed vein rings under different concentrations of Sodium Nitroprusside

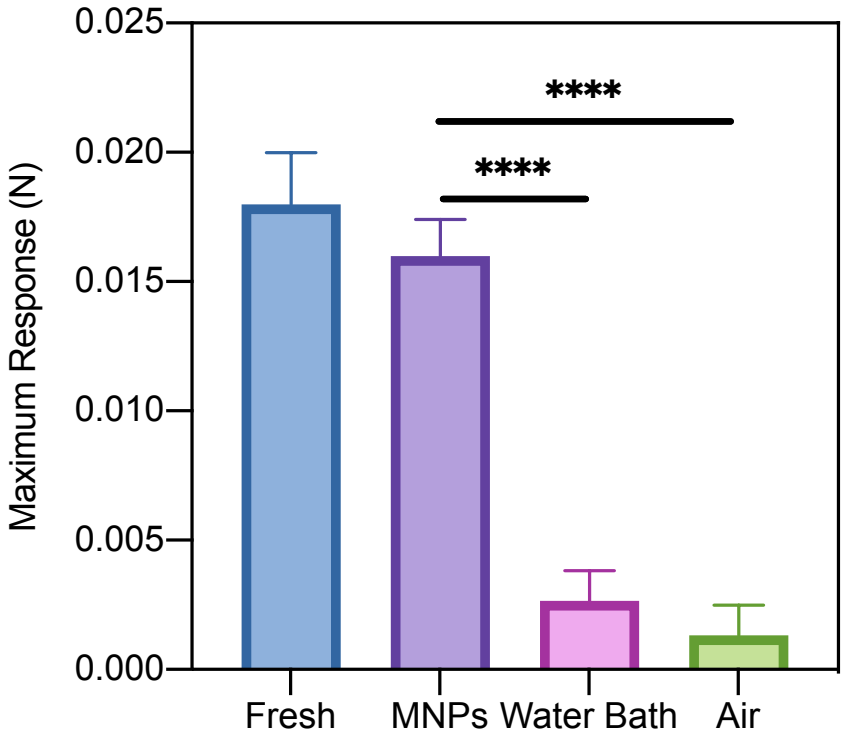

Figure 6-19. Maximum relaxation response with Sodium Nitroprusside at 10^{-1} M

6.2.8 *Metabolic activity of the post-thawed jugular vein*

A sign of the programmed cell death is the disruption of the mitochondria function, including changes in the membrane potential and modification to the oxidation potential. The electrical potential between the interior and exterior is maintained at a difference by the healthy mitochondrial membrane. Therefore, the biological functionality of the post-thawed tissues could also be determined through the measurements of mitochondrial membrane potential.

The fluorescence readings of TMRM solution are normalized to the control group presented in Figure 6-20. MNPs electromagnetic warming was comparable to the fresh control group ($83.74 \pm 11.62\%$ and 100%, $P = 0.2543$), while significantly higher than water bath ($24.78 \pm 6.34\%$, $P < 0.0001$), air warmed ($26.64 \pm 7.29\%$, $P < 0.0001$). The mean values $\pm$ standard deviations were determined based on nine replicates (n=9).

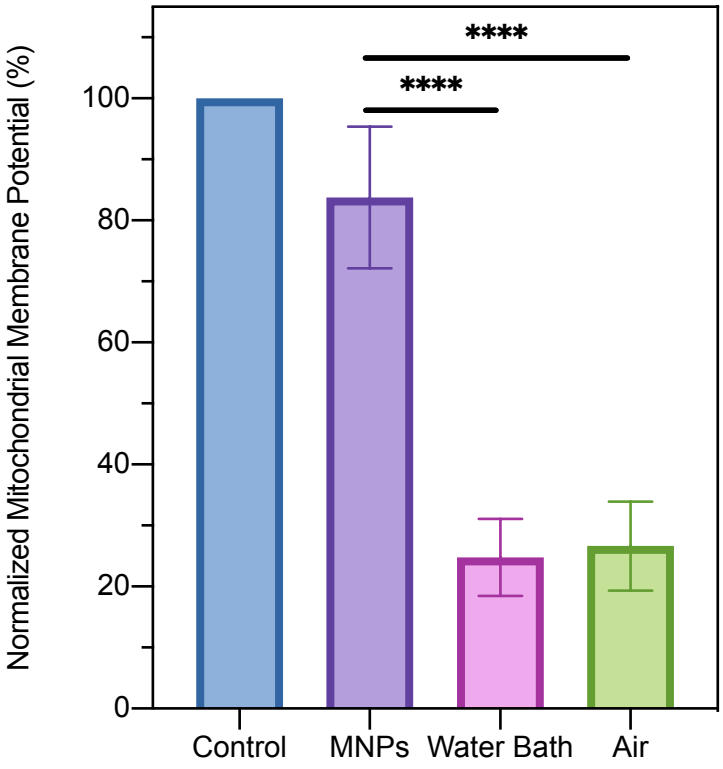

Figure 6-20. Normalized mitochondrial membrane potential

Higher fluorescence readings of the MNPs warming method indicated the post-thawed tissues were healthy and contained well-functioned mitochondria. The lower signal in the water bath and air convection confirmed the rupture of the cells, presumable to the devitrification caused by slow and less uniformed warming.

6.3 CONCLUSION

In this chapter, the rabbit jugular vein was successfully cryopreserved by vitrification and MNPs enhanced electromagnetic rewarming system. Besides vitrification, the viability and metabolic activity of large biological systems (tissues or organs) rely on rapid and uniform rewarming to avoid the damage caused by recrystallization.

This study compared the warming outcomes of MNPs enhanced electromagnetic warming, convective water bath, and natural air convection on thermal and biological aspects. The fast (326.91 ± 7.55 ℃ min^{-1}) and uniform (temperature difference less than 10 ℃ during the entire thawing) heating was captured by the thermal sensors. The viability, histology image analysis, biomechanical assessments, and mitochondrial membrane potential of post-thawed tissues were also determined; no statistical difference was found between the MNPs warmed veins and the fresh control group. Both tissue integrity and biological functionalities were well preserved and protected by the electromagnetic rewarming system.

Moreover, the low concentration of iron oxide nanoparticles and relatively small power input indicated the effective energy utilization with the automatic resonant frequency tracking system and the potential to even faster and uniformed heating with a higher dosage of MNPs and larger power input.

With continued improvements in the electromagnetic warming system, it is possible to preserve more complex biomaterials in the near future.

Chapter 7. SUMMARY AND FUTURE WORK

7.1 SUMMARY

In the past decades, several major breakthroughs in cryopreservation, a technology to preserve biomaterials at low temperatures to reduce or even pause the metabolism and chemical reactions, had been focused on the composition of the CPA solution and different freezing techniques. Unfortunately, advances in the cooling process have not been matched by similar progress in the rewarming.

In order to assess the heating rate effects on the cryopreservation, Jurkat cells were cooled and rewarmed at different rate combinations. The results show that at the same cooling rate, fast rewarming always achieved a higher recovery rate and metabolic activity of the post-thawed Jurkat cell, which consistent with the previous hypothesis proposed by Mazur.

The traditional cryopreservation is confined to simple and small biological systems due to the lack of an effective rewarming method. At the large size of targeted material, such as tissues or organs, convective water bath or natural air convection heating would not work. The slow warming that favors recrystallization could lead to the cells' rupture, and the large temperature gradient might cause the fracture within the sample. Thus, for the long-term preservation of complex and large-scale biomaterials, a rapid and uniform rewarming technology is needed.

Electromagnetic waves are considered a promising approach with the ability to generate volumetric heating within the sample solution. To further understand the relationship between the electromagnetic field and coupled heat transfer, the critical electric and thermal properties, including dielectric constant, dielectric loss, thermal conductivity, and heat capacity were determined for several CPA solutions. The cavity perturbation method was adopted to determine

the dielectric properties and select the appropriate composition and concentration of CPA solution in electromagnetic rewarming. The 10%DMSO and 0.25 M trehalose solution was picked due to its higher ability to convert electromagnetic energy into heat and used in the later cell rewarming test. The essential physical properties were also measured on several vitrification solutions. The results indicated that the imaginary part of complex permittivity should be high to absorb electric field energy, but a decreasing imaginary part as temperature increases could reduce the thermal runaway phenomenon. Therefore, DPVP (41% DMSO and 6% PVP) solution was selected as the sample vitrification solution in the later tissue test.

The dimension of the resonant cavity was calculated from Maxwell equations. A numerical simulation model based on the finite element method was established to assist the design and development of the electromagnetic resonance rewarming system. Electromagnetic field intensity and distribution at different input frequencies and power were calculated and modified. The effects of different sample shapes on the rewarming outcome were evaluated by the heating rate and final temperature distribution. The simulated results showed that the cylindrical holder has the better performance in electromagnetic warming.

The temperature-dependent resonant frequency of the cryopreserved sample is constantly changing in the thawing process. In order to maintain the resonant state within the cavity, a real-time resonant frequency monitoring and the controlling system was developed. Two approaches to ensure the resonant frequency were studied in this dissertation. First, a network analyzer was implemented to obtain the relationship between frequency and Qloss, then the empirical equation of the relationship from resonant frequency to temperature is acquired. Secondly, a spectrum analyzer was adopted to measure the real-time reflected power from the cavity. By adjusting the input frequency, the power reflection changed accordingly. Thus, the optimal input frequency

could be determined. Both approaches were coded to the Python program and tested with the vitrification solution. Experimental results suggested spectrum analyzer method has a faster adjustment to the temperature change, which accomplished a faster rewarming.

In this study, the interested temperature region is between $-196\,℃$ to physiological temperature. An automatic sample loading system was designed and manufactured to protect the operator from frostbite and also ensure the sample was precisely placed at the designated position in the cavity.

Moreover, in order to further improve the developed warming system, iron oxide superparamagnetic nanoparticles were added to the sample solution to harness the magnetic field energy. Since the high power utilization efficiency achieved by the resonant frequency tracking system, it is possible to succeed ultra-fast and uniform rewarming with a lower dosage of MNPs and small power input.

The MNPs enhanced electromagnetic system was tested with the rewarming of a large volume of Jurkat cell suspension and rabbit jugular vein. The post-thawed biomaterials were evaluated by the viability, metabolic activity, biomechanical assessment, and histology image analysis. All of the test results demonstrated that MNPs enhanced rewarming was significantly better than the convective water bath and natural air convection. The materials warmed by MNPs enhanced electromagnetic warming system were comparable to the fresh control samples.

7.2 FUTURE WORK

The exciting results from the large volume cell test and tissue test demonstrated the capability of the electromagnetic resonance rewarming system to deliver rapid and uniform heating. Thus, we are looking forward to solving the thawing challenges in organ preservation.

Despite the scale up of the warming system to fit the heating requirements for organ, the loading protocol of MNPs embedded vitrification solution also needs additional investigation. Several perfusion techniques are used to pump the solution into the heart, kidney, and liver. However, the penetration and distribution of vitrification solutions rely on the flow rates and circulation time. Moreover, the requirements and conditions are changing among different organs and solutions. All of these factors need quantitative analysis to ensure perfusion results.

In addition, many challenges still remain about vitrification and electromagnetic rewarming. It is known that the vitrification could be affected by the composition and concentration of solutions. However, there is a lack of a method/system to systematically and quantitatively verify the vitrification status. Currently, we check the amorphous glass state by visual observation. Apparently, this is not objective and sustainable due to the standards varies across different operators. The real-time resonant frequency monitoring and the controlling system could be modified to meet the requirements. Due to the naturally small dielectric properties of the ice, significantly low absorption of the electromagnetic energy or a large reflected power would be captured by the control system as the formation of ice crystals. In that case, we are not only measuring the resonant frequency but also actively checking the vitrification state and apply any necessary adjustment based on the dynamic feedback. This improved system would gain us a deeper understanding of the mechanisms of vitrification and reduce the injury to the biomaterials caused by recrystallization during the warming.

Though the developed electromagnetic resonance system succeeds in impressive heating performance, further improvements could be implemented to the resonant frequency tracking system. Due to the limitation of the current cavity design, we could not connect both the network

analyzer and spectrum analyzer to the heating system at the same time. Otherwise, the reflected power might destroy the equipment. Multiple options may solve the problem.

First, a mechanical switch is considered to be added between the directional coupler and power amplifier. The rest ports of the switch would be connected to the network analyzer and spectrum analyzer and automatically adjusted by the control system. In this setup, it is possible to switch between two devices continuously to mimic the 'real-time' measurement of the resonant frequency. The interval depends on the switch response time and the signal lag in the coaxial cable.

Second, the directional coupler in the current setup would be replaced with a hybrid coupler. Then a power combiner is introduced to the system and placed between the hybrid coupler and resonant cavity. The third port of the combiner is linked to the network analyzer through the protection of another directional coupler. The updated setup allows the system to achieve the actual real-time monitoring of the resonant frequency at the cost of losing half of the amplified power.

Third and perhaps the best, a new cavity is needed to place both probe antenna on the exterior wall. One probe would be served as the current one that responsible for the power input and monitoring the reflected power through the spectrum analyzer, while the other probe is connected to the network analyzer and in charge of the real-time monitoring of the resonant frequency. Another advantage of designing a new cavity, the automated sample loading system could be integrated into the heating system and load the samples from different orientations depending on the sample shape and size. For example, a smaller sample may install from the bottom surface while the larger one enters from the sidewall.

BIBLIOGRAPHY

1. Fahy, G.M., et al., Vitrification as an approach to cryopreservation. Cryobiology, 1984. 21(4): p. 407-426.
2. Polge, C., A.U. Smith, and A.S. Parkes, Revival of spermatozoa after vitrification and dehydration at low temperatures. Nature, 1949. 164(4172): p. 666.
3. Cordoba, R., et al., The occurrence of adverse events during the infusion of autologous peripheral blood stem cells is related to the number of granulocytes in the leukapheresis product. Bone Marrow Transplant, 2007. 40(11): p. 1063-7.
4. Bakken, A.M., O. Bruserud, and J.F. Abrahamsen, No differences in colony formation of peripheral blood stem cells frozen with 5% or 10% dimethyl sulfoxide. J Hematother Stem Cell Res, 2003. 12(3): p. 351-8.
5. Hidalgo, J.D., et al., Supraventricular tachyarrhythmias after hematopoietic stem cell transplantation: incidence, risk factors and outcomes. Bone Marrow Transplant, 2004. 34(7): p. 615-9.
6. Donmez, A., et al., Clinical side effects during peripheral blood progenitor cell infusion. Transfus Apher Sci, 2007. 36(1): p. 95-101.
7. Martin-Henao, G.A., et al., Adverse reactions during transfusion of thawed haematopoietic progenitor cells from apheresis are closely related to the number of granulocyte cells in the leukapheresis product. Vox Sang, 2010. 99(3): p. 267-73.
8. Mueller, F.O., T.A. Casey, and P.D. Trevor-Roper, Use of Deep-Frozen Human Cornea in Full-Thickness Grafts. Br Med J, 1964. 2(5407): p. 473-5.
9. Calmels, B., et al., Preclinical evaluation of an automated closed fluid management device: Cytomate, for washing out DMSO from hematopoietic stem cell grafts after thawing. Bone Marrow Transplant, 2003. 31(9): p. 823-8.
10. Sputtek, A., Cryopreservation of red blood cells and platelets. Methods in molecular biology (Clifton, N.J.), 2007. 368: p. 283-301.
11. Chen, C., Pregnancy after Human Oocyte Cryopreservation. The Lancet, 1986. 327(8486): p. 884-886.
12. al-Hasani, S., et al., Successful embryo transfer of cryopreserved and in-vitro fertilized rabbit oocytes. Human reproduction (Oxford), 1989. 4(1): p. 77-79.
13. Diener, B., et al., A method for the cryopreservation of liver parenchymal cells for studies of xenobiotics. Cryobiology, 1993. 30(2): p. 116-27.
14. Baxter, C., S. Aggarwal, and K.R. Diller, Cryopreservation of skin: a review. Transplantation proceedings, 1985. 17(6 Suppl 4): p. 112-120.
15. Lovelock, J.E., The haemolysis of human red blood-cells by freezing and thawing. Biochimica et Biophysica Acta, 1953. 10: p. 414-426.
16. Meryman, H.T., Freezing Injury and its Prevention in Living Cells. Annual review of biophysics and bioengineering, 1974. 3(1): p. 341-363.
17. Mazur, P., S.P. Leibo, and E.H.Y. Chu, A two-factor hypothesis of freezing injury. Experimental Cell Research, 1972. 71(2): p. 345-355.

18. Mazur, P., Cryobiology: the freezing of biological systems. Science, 1970. 168(3934): p. 939-49.
19. Gao, D. and J.K. Critser, Mechanisms of Cryoinjury in Living Cells. ILAR journal, 2000. 41(4): p. 187-196.
20. Brockbank, K.G., et al., Interstitial ice formation in cryopreserved homografts: a possible cause of tissue deterioration and calcification in vivo. The Journal of heart valve disease, 2000. 9(2): p. 200-206.
21. Scholander, P.F., et al., Supercooling and osmoregulation in arctic fish. Journal of cellular and comparative physiology, 1957. 49(1): p. 5-24.
22. DeVries, A.L. and D.E. Wohlschlag, Freezing Resistance in Some Antarctic Fishes. Science (American Association for the Advancement of Science), 1969. 163(3871): p. 1073-1075.
23. Wowk, B., Thermodynamic aspects of vitrification. Cryobiology, 2010. 60(1): p. 11-22.
24. Fahy, G.M., B. Wowk, and J. Wu, Cryopreservation of complex systems: the missing link in the regenerative medicine supply chain. Rejuvenation Res, 2006. 9(2): p. 279-91.
25. Ren, H.S., et al., Theoretical Prediction of Vitrification and Devitrification Tendencies for Cryoprotective Solutions. Cryobiology, 1994. 31(1): p. 47-56.
26. Etheridge, M.L., et al., RF heating of magnetic nanoparticles improves the thawing of cryopreserved biomaterials. Technology, 2014. 02(03): p. 229-242.
27. Amorim, C.A., et al., Vitrification as an alternative means of cryopreserving ovarian tissue. Reprod Biomed Online, 2011. 23(2): p. 160-86.
28. Carvalho, A.A., et al., Novel wide-capacity method for vitrification of caprine ovaries: Ovarian Tissue Cryosystem (OTC). Anim Reprod Sci, 2013. 138(3-4): p. 220-7.
29. Chong, Y.K., et al., Cryopreservation of neurospheres derived from human glioblastoma multiforme. Stem Cells, 2009. 27(1): p. 29-39.
30. Kasper, H.U., et al., Cryopreservation of precision cut tissue slices (PCTS): investigation of morphology and reactivity. Exp Toxicol Pathol, 2011. 63(6): p. 575-80.
31. Kuwayama, M., et al., Highly efficient vitrification method for cryopreservation of human oocytes. Reproductive BioMedicine Online, 2005. 11(3): p. 300-308.
32. Merino, O., et al., Fish (Oncorhynchus mykiss) spermatozoa cryoprotectant-free vitrification: stability of mitochondrion as criterion of effectiveness. Anim Reprod Sci, 2011. 124(1-2): p. 125-31.
33. Silvestre, M.A., et al., Vitrification and rapid freezing of rabbit fetal tissues and skin samples from rabbits and pigs. Theriogenology, 2002. 58(1): p. 69-76.
34. Silvestre, M.A., J.P. Sanchez, and E.A. Gomez, Vitrification of goat, sheep, and cattle skin samples from whole ear extirpated after death and maintained at different storage times and temperatures. Cryobiology, 2004. 49(3): p. 221-9.
35. Song, Y.C., et al., Vitrification of tissue engineered pancreatic substitute. Transplant Proc, 2005. 37(1): p. 253-5.
36. Song, Y.C., et al., Vitreous cryopreservation maintains the function of vascular grafts. Nat Biotechnol, 2000. 18(3): p. 296-9.
37. Ting, A.Y., et al., In vitro development of secondary follicles from cryopreserved rhesus macaque ovarian tissue after slow-rate freeze or vitrification. Hum Reprod, 2011. 26(9): p. 2461-72.

38. Milenkovic, M., et al., Viability and function of the cryopreserved whole rat ovary: comparison between slow-freezing and vitrification. Fertil Steril, 2012. 97(5): p. 1176-82.
39. Mazur, P., et al., Cryobiological preservation of Drosophila embryos. Science, 1992. 258(5090): p. 1932-5.
40. Seki, S., B. Jin, and P. Mazur, Extreme rapid warming yields high functional survivals of vitrified 8-cell mouse embryos even when suspended in a half-strength vitrification solution and cooled at moderate rates to -196 degrees C. Cryobiology, 2014. 68(1): p. 71-8.
41. Kuwayama, M., Highly efficient vitrification for cryopreservation of human oocytes and embryos: the Cryotop method. Theriogenology, 2007. 67(1): p. 73-80.
42. Spencer, P.L., Electronic cooking US 2582174, U.S.P.O. (Ed.), Editor. 1949.
43. Spencer, P.L., Prepared food article and method of preparing US 2480679, U.S.P.O. (Ed.(Editor. 1947.
44. Spencer, P.L., Food cooking US2540036, U.S.P.O. (Ed.), Editor. 1948.
45. Spencer, P.L., Method of treating foodstuffs US2495429, U.S.P.O. (Ed.), Editor. 1945.
46. 4. Analytical investigation of thermal runaway during electrical thawing of frozen tissue. Cryobiology, 1968. 4(5): p. 248.
47. Ketterer, F.D., H.I. Holst, and H.B. Lehr, Improved viability of kidneys with microwave thawing. Cryobiology, 1971. 8(4).
48. Guttman, F.M., et al., Survival of canine kidneys after treatment with dimethyl-sulfoxide, freezing at −80 °C, and thawing by microwave illumination. Cryobiology, 1977. 14(5): p. 559-567.
49. Pegg, D.E., C.J. Green, and C.A. Walter, Attempted canine renal cryopreservation using dimethyl sulphoxide helium perfusion and microwave thawing. Cryobiology, 1978. 15(6): p. 618-626.
50. Burdette, E.C., A.M. Karow, and A.H. Jeske, Design, development, and performance of an electromagnetic illumination system for thawing cryopreserved kidneys of rabbits and dogs. Cryobiology, 1978. 15(2): p. 152-167.
51. Ruggera, P.S. and G.M. Fahy, Rapid and uniform electromagnetic heating of aqueous cryoprotectant solutions from cryogenic temperatures. Cryobiology, 1990. 27(5): p. 465-478.
52. Rachman, M.J., S. Evans, and D.E. Pegg, Experimental results on the rewarming of a cryopreserved organ phantom in a UHF field. Journal of Biomedical Engineering, 1992. 14(5): p. 397-403.
53. Robinson, M.P. and D.E. Pegg, Rapid electromagnetic warming of cells and tissues. IEEE Trans Biomed Eng, 1999. 46(12): p. 1413-25.
54. Mazur, P., Physical-chemical basis of injury from intracellular freezing in yeast. Cryobiology, 1967. 3(4): p. 348.
55. Mazur, P., THE ROLE OF CELL MEMBRANES IN THE FREEZING OF YEAST AND OTHER SINGLE CELLS. Annals of the New York Academy of Sciences, 1965. 125(2): p. 658-676.
56. Survival of plant tissue at super-low temperatures. V. An electron microscope study of ice in cortical cells cooled rapidly. Cryobiology, 1968. 4(4): p. 214.
57. Shimada, K. and E. Asahina, Visualization of intracellular ice crystals formed in very rapidly frozen cells at −27 °C. Cryobiology, 1975. 12(3): p. 209-218.

58. Farrant, J., et al., Use of two-step cooling procedures to examine factors influencing cell survival following freezing and thawing. Cryobiology, 1977. 14(3): p. 273-286.
59. Death of Frozen Yeast in the Course of Slow warming, in Ciba Foundation Symposium - The Frozen Cell. 1970. p. 89-96.
60. Bank, H., Visualization of freezing damage. II. Structural alterations during warming. Cryobiology, 1973. 10(2): p. 157-170.
61. Moor, H., Die Gefrier-Fixation lebender Zellen und ihre Anwendung in der Elektronenmikroskopie. Cell and tissue research, 1964. 62(4): p. 546-580.
62. Mazur, P., Freezing of living cells: mechanisms and implications. American Journal of Physiology: Cell Physiology, 1984. 247(3): p. C125-C142.
63. Shum, D., et al., A high density assay format for the detection of novel cytotoxic agents in large chemical libraries. Journal of enzyme inhibition and medicinal chemistry, 2008. 23(6): p. 931-945.
64. Hill, N.E., Dielectric behaviour of biological molecules in solution by E. H. Grant, R. J. Sheppard and S. P. South. Pp. 237. Clarendon Press: Oxford University Press, Oxford and London. 1978. In the series Monographs on Physical Biochemistry. £11.00. Biochemical Education, 1979. 7(1): p. 16-16.
65. Robinson, M.P., et al., Electromagnetic re-warming of cryopreserved tissues: effect of choice of cryoprotectant and sample shape on uniformity of heating. Phys Med Biol, 2002. 47(13): p. 2311-25.
66. Wusteman, M.C., et al., Vitrification media: toxicity, permeability, and dielectric properties. Cryobiology, 2002. 44(1): p. 24-37.
67. Hasar, U.C. and M.T. Yurtcan, A microwave method based on amplitude-only reflection measurements for permittivity determination of low-loss materials. Measurement, 2010. 43(9): p. 1255-1265.
68. Ansorge, S., G. Esteban, and G. Schmid, Multifrequency permittivity measurements enable on-line monitoring of changes in intracellular conductivity due to nutrient limitations during batch cultivations of CHO cells. Biotechnol Prog, 2010. 26(1): p. 272-83.
69. Juan-García, P. and J.M. Torrents, Measurement of mortar permittivity during setting using a coplanar waveguide. Measurement Science and Technology, 2010. 21(4).
70. Lee, K.Y., et al., In situ measurements of complex permittivity and moisture content in oil palm fruits. The European Physical Journal Applied Physics, 2010. 49(3).
71. Bradford, J.H., J.T. Harper, and J. Brown, Complex dielectric permittivity measurements from ground-penetrating radar data to estimate snow liquid water content in the pendular regime. Water Resources Research, 2009. 45(8).
72. Zohdi, T.I., F.A. Kuypers, and W.C. Lee, Estimation of red blood cell volume fraction from overall permittivity measurements. International Journal of Engineering Science, 2010. 48(11): p. 1681-1691.
73. Ba, D. and P. Sabouroux, EpsiMu, A toolkit for permittivity and permeability measurement in microwave domain at real time of all materials: Applications to solid and semisolid materials. Microwave and Optical Technology Letters, 2010. 52(12): p. 2643-2648.
74. Shibata, K., Measurement of Complex Permittivity for Liquid Materials Using the Open-Ended Cut-Off Waveguide Reflection Method. IEICE transactions on electronics, 2010. E93-C(11): p. 1621-1629.

75. Komarov, V., S. Wang, and J. Tang, Permittivity and Measurements, in Encyclopedia of RF and Microwave Engineering. 2005.
76. Marsland, T.P., S. Evans, and D.E. Pegg, Dielectric measurements for the design of an electromagnetic rewarming system. Cryobiology, 1987. 24(4): p. 311-323.
77. Michelson, S.C. and S. Evans, Dielectric properties of supercooled cryoprotectant agents. Physics in medicine & biology, 1996. 41(10): p. 2053-2066.
78. Evans, S., Electromagnetic Rewarming: The Effect of CPA Concentration and Radio Source Frequency on Uniformity and Efficiency of Heating. Cryobiology, 2000. 40(2): p. 126-138.
79. Lin, M., M.H. Duane, and M.N. Afsar, Cavity-Perturbation Measurement of Complex Permittivity and Permeability of Common Ferrimagnetics in Microwave-Frequency Range. IEEE Transactions on Magnetics, 2006. 42(10): p. 2885-2887.
80. Waldron, R.A., Perturbation theory of resonant cavities. Proceedings of the IEE Part C: Monographs, 1960. 107(12).
81. Kraszewski, A.W. and S.O. Nelson, Observations on resonant cavity perturbation by dielectric objects. IEEE Transactions on Microwave Theory and Techniques, 1992. 40(1): p. 151-155.
82. Hasan, A. and A.F. Peterson, Improved measurement of complex permittivity using artificial neural networks with scaled inputs. Microwave and Optical Technology Letters, 2011. 53(9): p. 2139-2142.
83. Von Hippel, A.R., Dielectrics and waves. 1954, New York; London: Wiley; Chapman & Hall.
84. Liang, X.M., et al., High accuracy thermal conductivity measurement of aqueous cryoprotective agents and semi-rigid biological tissues using a microfabricated thermal sensor. Scientific reports, 2015. 5(1): p. 10377-10377.
85. Evans, S., M.J. Rachman, and D.E. Pegg, Design of a UHF applicator for rewarming of cryopreserved biomaterials. IEEE Trans Biomed Eng, 1992. 39(3): p. 217-25.
86. Luo, D., et al., Development of a single mode electromagnetic resonant cavity for rewarming of cryopreserved biomaterials. Cryobiology, 2006. 53(2): p. 288-93.
87. Bai, X., et al., Analysis of electromagnetic heating patterns inside a cryopreserved organ. Journal of Biomedical Engineering, 1992. 14(6): p. 459-466.
88. Dayong, G., L. Huai-Zhi, and L. Cai-Cheng, Combined electromagnetic and heat-conduction analysis of rapid rewarming of cryopreserved tissues. IEEE Transactions on Microwave Theory and Techniques, 2000. 48(11): p. 2185-2190.
89. Penfold, J.D. and S. Evans, Control of thermal runaway and uniformity of heating in the electromagnetic rewarming of a cryopreserved kidney phantom. Cryobiology, 1993. 30(5): p. 493-508.
90. Han, X., et al., Numerical simulation of the microwave rewarming process of cryopreserved organs. Microwave and Optical Technology Letters, 2005. 46(3): p. 201-205.
91. Wang, T., et al., Numerical simulation of the effect of superparamagnetic nanoparticles on microwave rewarming of cryopreserved tissues. Cryobiology, 2014. 68(2): p. 234-43.
92. Vaz, R.H., et al., Simulation and uncertainty quantification in high temperature microwave heating. Applied Thermal Engineering, 2014. 70(1): p. 1025-1039.

93. Lizhuang, M., et al., Experimental validation of a combined electromagnetic and thermal FDTD model of a microwave heating process. IEEE transactions on microwave theory and techniques, 1995. 43(11): p. 2565-2572.
94. Torres, F. and B. Jecko, Complete FDTD analysis of microwave heating processes in frequency-dependent and temperature-dependent media. IEEE transactions on microwave theory and techniques, 1997. 45(1): p. 108-117.
95. Pathak, V., Z. Yun, and M.F. Iskander, Development of an integrated multi-grid 3D FDTD and finite-difference heat transfer code to simulate microwave drying in multimode cavities. 2001, IEEE. p. 138-141 vol.4.
96. Zhang, Q., T.H. Jackson, and A. Ungan, Numerical modeling of microwave induced natural convection. International journal of heat and mass transfer, 2000. 43(12): p. 2141-2154.
97. Mirabito, C., et al., FEMLAB Model of a Coupled Electromagnetic-Thermal Boundary Value Problem. Research Experience: Worcester Polytechnic Institute, 2005.
98. Zhang, H., et al., Electromagnetics, heat transfer, and thermokinetics in microwave sterilization. AIChE Journal, 2001. 47(9): p. 1957-1968.
99. Rall, W.F. and G.M. Fahy, Ice-free cryopreservation of mouse embryos at -196 degrees C by vitrification. Nature (London), 1985. 313(6003): p. 573-575.
100. He, X., et al., Vitrification by ultra-fast cooling at a low concentration of cryoprotectants in a quartz micro-capillary: A study using murine embryonic stem cells. Cryobiology, 2008. 56(3): p. 223-232.
101. Pegg, D.E., Principles of cryopreservation. (1064-3745 (Print)).
102. Mehl, P.M., Nucleation and Crystal Growth in a Vitrification Solution Tested for Organ Cryopreservation by Vitrification. Cryobiology, 1993. 30(5): p. 509-518.
103. Fahy, G.M., et al., Physical and biological aspects of renal vitrification. Organogenesis, 2009. 5(3): p. 167-175.
104. Brockbank, K.G.M., et al., Vitrification of Heart Valve Tissues, in Cryopreservation and Freeze-Drying Protocols, W.F. Wolkers and H. Oldenhof, Editors. 2021, Springer US: New York, NY. p. 593-605.
105. Fahy, G.M., et al., Improved vitrification solutions based on the predictability of vitrification solution toxicity. Cryobiology, 2004. 48(1): p. 22-35.
106. Huang, H., et al., Alginate Hydrogel Microencapsulation Inhibits Devitrification and Enables Large-Volume Low-CPA Cell Vitrification. Advanced functional materials, 2015. 25(44): p. 6839-6850.
107. Hayashi, K., et al., High-frequency, magnetic-field-responsive drug release from magnetic nanoparticle/organic hybrid based on hyperthermic effect. ACS Appl Mater Interfaces, 2010. 2(7): p. 1903-11.
108. Kumar, C.S. and F. Mohammad, Magnetic nanomaterials for hyperthermia-based therapy and controlled drug delivery. Adv Drug Deliv Rev, 2011. 63(9): p. 789-808.
109. Liong, M., et al., Multifunctional inorganic nanoparticles for imaging, targeting, and drug delivery. ACS Nano, 2008. 2(5): p. 889-96.
110. Sun, C., J.S. Lee, and M. Zhang, Magnetic nanoparticles in MR imaging and drug delivery. Adv Drug Deliv Rev, 2008. 60(11): p. 1252-65.
111. Park, J.H., et al., Cooperative nanomaterial system to sensitize, target, and treat tumors. Proc Natl Acad Sci U S A, 2010. 107(3): p. 981-6.

112. Johannsen, M., et al., Thermotherapy of prostate cancer using magnetic nanoparticles: feasibility, imaging, and three-dimensional temperature distribution. Eur Urol, 2007. 52(6): p. 1653-61.
113. Ernst, C., et al., Improved DNA extraction and purification with magnetic nanoparticles for the detection of methicillin-resistant Staphylococcus aureus. Veterinary Microbiology, 2019. 230: p. 45-48.
114. Schätz, A., et al., Cu(II)−Azabis(oxazoline) Complexes Immobilized on Magnetic Co/C Nanoparticles: Kinetic Resolution of 1,2-Diphenylethane-1,2-diol under Batch and Continuous-Flow Conditions. Chemistry of Materials, 2010. 22(2): p. 305-310.
115. Manuchehrabadi, N., et al., Improved tissue cryopreservation using inductive heating of magnetic nanoparticles. Science translational medicine, 2017. 9(379): p. eaah4586.
116. Rodríguez-Luccioni, H.L., et al., Enhanced reduction in cell viability by hyperthermia induced by magnetic nanoparticles. International journal of nanomedicine, 2011. 6: p. 373-380.
117. Jordan, A., et al., Cellular uptake of magnetic fluid particles and their effects on human adenocarcinoma cells exposed to AC magnetic fields in vitro. International journal of hyperthermia, 1996. 12(6): p. 705-722.
118. Brigger, I., C. Dubernet, and P. Couvreur, Nanoparticles in cancer therapy and diagnosis. Advanced drug delivery reviews, 2012. 64: p. 24-36.
119. Zhang, W., Nanoparticle Aggregation: Principles and Modeling, in Nanomaterial: Impacts on Cell Biology and Medicine, D.G. Capco and Y. Chen, Editors. 2014, Springer Netherlands: Dordrecht. p. 19-43.
120. Colombo, M., et al., Biological applications of magnetic nanoparticles. Chemical Society reviews, 2012. 41(11): p. 4306-4334.
121. Bezinover, D. and F. Saner, Organ transplantation in the modern era. BMC Anesthesiology, 2019. 19(1): p. 32.
122. Black, C.K., et al., Solid organ transplantation in the 21(st) century. Annals of translational medicine, 2018. 6(20): p. 409-409.
123. Grinyó, J.M., Why is organ transplantation clinically important? Cold Spring Harbor perspectives in medicine, 2013. 3(6): p. a014985.
124. Kerridge, I.H., et al., Death, dying and donation: organ transplantation and the diagnosis of death. Journal of Medical Ethics, 2002. 28(2): p. 89-94.
125. Watson, C.J.E. and J.H. Dark, Organ transplantation: historical perspective and current practice. BJA: British Journal of Anaesthesia, 2012. 108(suppl_1): p. i29-i42.
126. Lewis, J.K., et al., The Grand Challenges of Organ Banking: Proceedings from the first global summit on complex tissue cryopreservation. Cryobiology, 2016. 72(2): p. 169-182.
127. Jin, B., F.W. Kleinhans, and P. Mazur, Survivals of mouse oocytes approach 100% after vitrification in 3-fold diluted media and ultra-rapid warming by an IR laser pulse. Cryobiology, 2014. 68(3): p. 419-430.
128. Council, N.R., Guide for the Care and Use of Laboratory Animals: Eighth Edition. 2011, Washington, DC: The National Academies Press. 246.
129. Gbaguidi, X., et al., Internal jugular vein thrombosis: outcome and risk factors. QJM: An International Journal of Medicine, 2010. 104(3): p. 209-219.

130. Marshall-Goebel, K., et al., Assessment of Jugular Venous Blood Flow Stasis and Thrombosis During Spaceflight. JAMA Network Open, 2019. 2(11): p. e1915011-e1915011.
131. Perloff, J.K., Importance of elevated jugular venous pressure and a third heart sound in asymptomatic left ventricular dysfunction. The American Journal of Medicine, 2003. 114(6): p. 499-500.
132. Zhou, D., et al., Understanding jugular venous outflow disturbance. CNS neuroscience & therapeutics, 2018. 24(6): p. 473-482.